UNIVERSITÀ
DEGLI STUDI
DI PADOVA

UNIVERSITA' DEGLI STUDI DI PADOVA

INSTITUTO SUPERIOR TECNICO - UNIVERSIDADE TECNICA DE LISBOA

Centro Interdipartimentale "*Centro Ricerche Fusione"* Università di Padova

JOINT RESEARCH DOCTORATE IN FUSION SCIENCE AND ENGINEERING

PhD Thesis

PHYSICS OF NEGATIVE ION EXTRACTION AND ACCELERATION IN NEUTRAL BEAM INJECTORS

Coordinator **:** Chiar.mo Prof. Piero Martin

Supervisor :Chiar.mo Prof. Francesco Gnesotto

Supervisor : Dott. Vanni Antoni

Doctoral Student: Pierluigi Veltri

Padova, 31 Gennaio 2010

Contents

Abstract

Most of the work reported in this PhD thesis was carried out at Consorzio RFX, where the most important neutral beam facility worldwide is under construction. This test bed will host 2 experiments, an ion source and a full injector, representing the state of art technology in the NBI context.
In this initial phase of design and optimization the modeling plays a key role in defining the characteristics of the devices and in anticipating their performance. In this perspective the work reported here has the scope to analyze some issues that are critical for the operation of such experiments, with particular attention to the phase of extraction and acceleration of ions from the source, before they are neutralized and injected into the plasma core. Many issues strictly connected to this basic topic will be discussed as well, as the production of secondary particles by interaction of the beam with the gas flowing in the injector. The development, implementation and use of dedicated models are described and their results discussed and, in some cases benchmarked with existing experiments.

Riassunto

Gran parte del lavoro descritto in questa tesi è stato svolto presso il Consorzio RFX, dove è in corso di costruzione quella che diverrà il più grande laboratorio di prova del mondo dedicato agli iniettori di neutri. Questo impianto ospiterà due esperimenti, una sorgente di ioni ed un acceleratore completo, che rappresentano la tecnologia più all'avanguardia nel contesto degli NBIs. Nella fase iniziale di progettazione e ottimizzazione di tali dispositivi la modellizzazione gioca un ruolo chiave, aiutando a definire le caratteristiche dell'iniettore e dando la possibilità di prevedere le sue prestazioni. In questa prospettiva il lavoro riportato in questa tesi ha lo scopo di analizzare alcuni aspetti cruciali per il funzionamento degli iniettori, prestando particolare attenzione alla fase di estrazione ed accelerazione degli ioni dalla sorgente, prima che vengano neutralizzati ed iniettati nel plasma. Allo stesso tempo saranno analizzati diversi aspetti strettamente correlati a questi argomenti di base, come, ad esempio, la produzione di particelle secondarie durante l'interazione tra il fascio ed il gas presente nell'iniettore. Verranno dunque presentati lo sviluppo, l'implementazione e l'uso di specifici modelli, i cui risultati verranno discussi ed, in alcuni casi, confrontati con le evidenze sperimentali di dispositivi esistenti.

Summary

The problem of limited energy resources and the environmental concerns about the existing energy production techniques urgently ask for the development of renewable and clean energy production methods. In this frame the realization of a nuclear fusion reactor represents one of the main objectives, and for sure the most ambitious.
In particular the nuclear fusion obtained by magnetic confinement of plasma emerged in the latest years as the most promising concept to menage the power produced by this energy source. In the devices exploiting this concept, the fusion reactions between two nuclei occur inside a plasma, a state of matter consisting in a quasi-neutral ensemble of ions and electrons. Since plasmas are subjects to magnetic fields they can be confined by means of particular geometric configurations in which particles are forced to follow prescribed orbits.
The studies developed in that direction, since the fifties, yielded more and more encouraging results and important breakthroughs both in physics and technology and inspired the ITER project. This experimental reactor could give, in the next few decades the definitive answers to many questions on the scientific and technological feasibility of a fusion reactor. In order to have a sufficient number of reaction to occur, the plasma temperature in ITER must be raised up to more than 10 KeV. The ohmic heating which is intrinsically produced by self induced current flowing in the plasma is not sufficient to reach this temperature and the use of auxiliary heating methods is necessary. Among the systems used to reach this high temperature range, a fundamental role is played by the injection of intense beams of particles into the plasma, which is consequently heated by collisions. This process is realized by means of Neutral Beam Injectors (NBIs).
The basic concept of the functioning of this device consist in the extraction of ions from an ion source and into their acceleration toward the reactor. In order to penetrate the high magnetic field confining the plasma, the beam of particles must be previously neutralized, and this is accomplished by charge exchange processes inside a neutralizer.

The beam performance is in large part determined by the characteristics of the source and of the accelerator, since it strongly depends on the fraction of ion current produced and extracted. This thesis discusses some aspects of the physics involved in the phases of beam formation and acceleration, describing the most important phenomena occurring and the models developed to deal with them.
Since the topic covers several branches, ranging from atomic and plasma physics to optics, heat conduction, and acceleration of charged particles problems, it was found convenient to organize the matter in chapters divided into macro arguments, also reflecting the intrinsic differences present in the distinct components of the injector.
Chapter 1 contains an overview on the problem of the world increasing energy demand and the search for new sources and technologies. After a short review on the existing energy sources the context of nuclear fusion it is introduced. The physical and engineering basis are described, together with the progresses obtained in the latest years, leading to the ITER project. A second part will be devoted to present the essentials of an NBI, anticipating the topics which will be treated more in details in further chapters. The final part contains the description of the two experiments SPIDER and MITICA under development at Consorzio RFX in Padova, with the purpose to study the physical and engineering problems of neutral beam injection.
Chapter 2 will focus on the description of the ion plasma source. Some general notions on its functioning are given, and particular attention is dedicated in describing the more important processes responsible for the formation of negative ions inside the confined plasma. To deal with them the knowledge of the cross section of all the possible reaction occurring between ions and molecules is necessary, and intensive work was done on the collection and implementation of a structured database of relevant data for source and beam interaction. The description of such work is addressed in the final section of this chapter.
In **chapter 3** the problems of ion extraction and acceleration is treated. In the first section an overview on the physics governing the extraction of particles from the source is given. In particular the phenomenon of the formation of a transition layer between the source plasma and its boundary is reviewed, and an analytical solution is given for a simple case. Then a section is dedicated to introduce the way in which the modeling is used to help the understanding of this phenomenon. In this context a particular theoretical model developed during the doctorate and its implementation in a robust numerical code will be presented. This code, called Bypo, represent a considerable step beyond the modeling of negative ion extraction and acceleration. The description of its characteristics and potentiality and the

discussion of some results cover great part of this section.
Chapter 4 is devoted to study the interaction of the beam with the gas flowing in the accelerator and with the material surfaces. The phenomenon of production of secondary particles in atomic interactions between beam and gas will be addressed. This kind of studies lead to the creation of a dedicated code, developed as an add-on for the Bypo code described in section 3.4, devoted to study the trajectories of this secondary, and their effects on the space charge distribution and on the formation of intense thermal fluxes on the injector components. Another topic connected with the formation of secondary is the space charge compensation occurring in the drift region of the injector. A section is dedicated to describe the peculiarities of this phenomena and the numerical tools developed to deal with it. Finally, the interaction of the beam with surfaces is presented with the description of some models devoted to estimate the thermal power deposition on structures and dimension the cooling system.
Chapter 5 focus on the description of the contribution to the activities of design and optimization of the future devices. This work needed the knowledge on the suite of codes currently used at RFX in the framework of NBI modeling which actually account for dozen of models and numerical tools. The characteristics of the different codes exploited are described by presenting the results carried out for the specific case of the exploration of the scenarios that the SPIDER experiment can experience during its operation.
Chapter 6 present the preliminary benchmark between some of the codes previously described and existing experiment. In the perspective of enhancing the level of reliability of the codes, in fact, the experimental validation is a fundamental subject. The work described in this chapter was carried out in the frame of the ongoing collaboration with the Japanese institute of NIFS. In this laboratory the most advanced existing negative ion based neutral beam injectors are installed on the LHD fusion device. The comparison involved the use of all the most important members of the complete RFX set of codes. In a first section the benchmark exploited calorimetric measures giving the temperature rise of the accelerator grids due to power fluxes of primary and secondary particles. A second section focus on the studies of the beam optics under the effect of the variation in the acceleration voltage, following the perveance match test performed on one of the injector.The main results are discussed and the pathway of future collaboration is described.
Chapter 7 will conclude this thesis with the discussion of the most important results carried out, highlighting the importance of the work done, and analyzing the possible implications for the developing of the experiment in the PRIMA test bed. Some considerations on open points and future perspective are also included.

Finally 3 appendices contain details about further work performed during the PhD course. Appendix A describes a particular model developed in the context of high voltage holding modeling. Using the hypothesis of the consecutive emissions of particles from the surfaces of an electrostatic accelerator, this model appear able to predict the position of a micro-discharge between the electrodes initiating the breakdown process. Appendix B describes the contribution given in the design of the instrumented calorimeter for the SPIDER source, by means of numerical tools, and appendix C include the database of reactions mentioned in chapter 2.

Chapter 1

Introduction

This chapter will introduce the concept of nuclear fusion, as one possible alternative to challenge the increasing energy demand of the world. After a short overview on the energetic problem, the basic issues of nuclear fusion will be described, with particular attention to the ITER project, representing the most important fusion experiment ever designed. Then, in the context of the auxiliary systems required to heat the plasma up the the temperature required to begin the fusion reaction, a section will be dedicated to the introduction to the neutral beam injection, constituting the main argument of this PhD thesis.

1.1 The World Energy Problem

In Europe, as in the rest of the industrialized world, we use an enormous amount of energy, as we go about our everyday lives. Energy use has increased significantly since the start of the industrial revolution, due to increase human population, increased production of consumer goods and increased intensive appliances. The last reports shown that thought the past year has been difficult and full of upheaval in the energy markets: for the first time form the oil crisis of 1981, the world energy demand felt with the 2009 economic contraction [1]. Anyway it is expected to resume its long term upward trend with the economic recovery, so that the search for the new source of energy remains an urgent issue. Our current modes of energy production are based on the use of fossils fuels, according tho the graph in figure 1.1, leading to a huge production of carbon dioxide (CO_2) emissions, while the contribution of CO_2 free source of energy is still modest; In this perspective of high environment pollution the concerns about global warming, acid rain and related problems are well justified if we consider that if the world will

continue to use the actual main energy sources, in the next 20 years we shall input the atmosphere the same amount of CO_2 we have produced since the beginning of the industrial revolution [2].[3]. In addition to the problem of

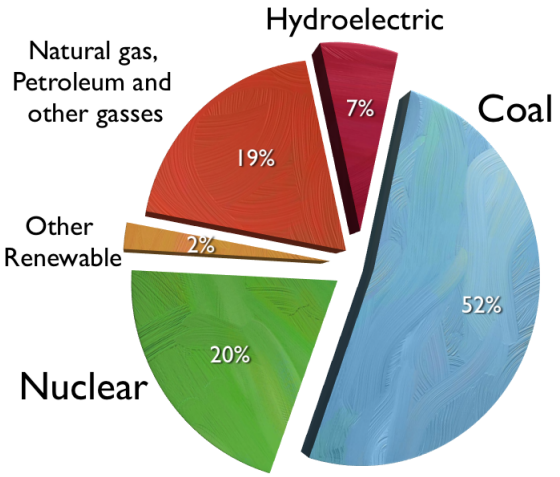

Figure 1.1: World energy use by type in 2000.

CO_2 concentration in the atmosphere, we should consider that except for coal, the supply of these fuels at present rate of consumption will last in few decades.
By focusing on the oil, which is the most commonly used fuel, it appears to be in the shortest supply worldwide, but continues to be that commodity on which we rely most heavily: the Association for the Study of Peak Oil and Gas (ASPO), based on current information about known oil reserves, estimates of future discovery, growing oil demand, and available technology, estimates that peak of the world oil production have already occurred. Even if other estimations are more optimistic, and new technology discoveries would allow in the future for easier extraction, the problem of finite resources remains open.
In this context, the renewables energies represent the most long term alternative, including wind power, tidal power, geothermal power, combustion of wood and biomass, hydroelectric power and solar energy. Unfortunately even if they will contribute much more in the future, they are not expected be able to satisfy the total demand, certainly not for the energy requirements implied by projections of our level of consumption. Moreover many of these energy sources are restricted to particular geological or geographic sites (tidal, geothermal, hydroelectric) and/or tend to be least available when most needed (solar energy at night or in the winter), and/or cannot be turned

on and off at will to meet the power demand curve of an electric utility.
The other important source of energy used so far to fulfill world energy needs is the nuclear power. As we will see, this definition lacks of precision, since it usually refers only to one of the two nuclear reactions that can be used to generate energy, the nuclear fission. In this process the nucleus of an atom, usually Uranium, splits into two or more smaller nuclei and usually some by-product particles, emitting energy in the form of gamma and other radiation. Converting heat produced by reactions into kinetic energy by means of a steam turbine, and then into electricity using a generator, is the standard simplified use of this energy. Even if nowadays nuclear power provides about 20% of the world's electricity, the use of Uranium fission to generate electricity is still controversial because of the problem of storing radioactive waste for indefinite periods, the potential for possibly severe radioactive contamination by accident or sabotage, and the possibility that its use could lead in some countries to the proliferation of nuclear weapons. Moreover Uranium is again a non-renewable resource and, at the present rate of use, there are 50 years left of low-cost known Uranium reserves.

1.2 Thermonuclear Fusion

As already mentioned, nuclear fission is not the only way to extract the nuclear energy from atoms. The inverse process, nuclear fusion, has interesting and positive features both relative to the environment preservation and to the availability of energy. The energy production, as in the case of fission, exploits the unbalance between the mass of one complex element with respect to the elements composing it. This mass defect reverses in a production of energy, as the atoms are forced together or split. If the combined nuclear mass is less than that of iron (Fe) at the peak of the binding energy curve, reported in 1.2, then the nuclear particles will be more tightly bound than they were in the lighter nuclei, and that decrease in mass comes off in the form of energy , according to the Einstein relationship

$$E = \Delta m c^2 \tag{1.1}$$

E being the energy produced and Δm the mass defect between the reactant and product. This process in known as nuclear fusion, while the nuclear fission yield energy by the mass defect of elements heavier than Fe. Nuclear Fusion is a basilar phenomenon in nature, responsible, for instance, to the processes producing energy into the stars and other astrophysical settings. Two light nuclei can fuse together if they are brought sufficiently close for the short-range attractive nuclear force to overcome by quantum tunneling

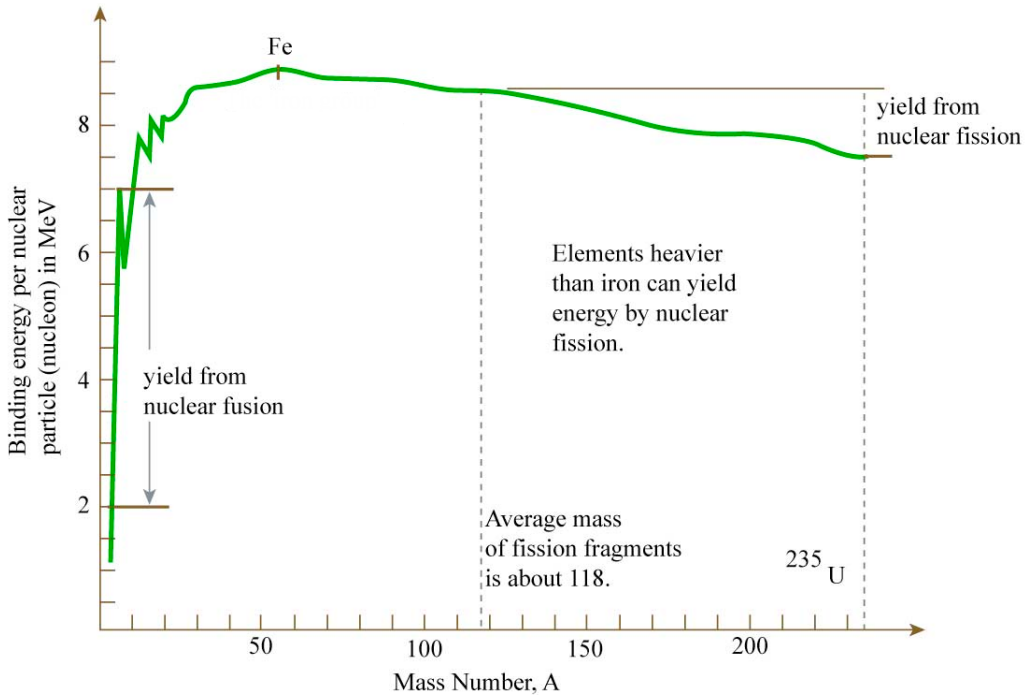

Figure 1.2: Binding energy Vs Mass number curve. Note the higher energy gain of fusion process with respect to fission.

the Coulomb repulsion among them. This is possible if the two reactants collide with high enough kinetic energy. For a significant fraction of fusion reactions to occur, matter has thus to be brought to high densities and temperatures for a sufficiently long time. In such conditions, matter is in the plasma state, a quasi-neutral ensemble of ions and electrons [4]. Between the various advantages of the fusion with respect to fission, we should list the intrinsic safety of the operation, since the reactions requires high density and temperature plasma to occur, avoiding the possibility of chain reactions, the relative abundance of fusion fuels, whose availability can provide the production of large amount of energy for thousand of years and the neglectable amount of nuclear waste to be contained, since the materials will lose their radioactivity in time scales of decades. Moreover in case of nuclear fusion the overlapping with nuclear weapon technology is small avoiding a contribution to nuclear proliferation.
While the fusion processes in the stars exploits the huge force of gravity of the astrophysical body to confine the plasma, to realize the fusion in laboratories, where that large amount of mass is clearly not available, other

technique where developed. In particular two methods emerged to be rather promising:
Magnetic confinement fusion[5] exploiting the use of strong magnetic fields to confine matter in the plasma state.
Inertial confinement fusion[6], where small volumes of solid matter are brought to sufficiently high temperatures and densities by firing high power lasers from many different directions. This compresses and heats the matter, and brings it to critical conditions.
Since the work of this thesis is devoted to investigate some aspects of physics related to magnetically confined fusion, from here on only this kind of method will be treated.
Within the several fusion reaction possible, the most favorable reaction in conditions attainable in laboratory exploiting the reactants deuterium and tritium is:

$$ {}^{2}_{1}D + {}^{3}_{1}T \rightarrow {}^{3}_{2}He + {}^{1}_{0}n \tag{1.2} $$

having a cross section peck in a relatively low energy range around 100 KeV, as reported in figure 1.3. In the same figure also a schematic of the process, including the energy carried by the single particles is reported.

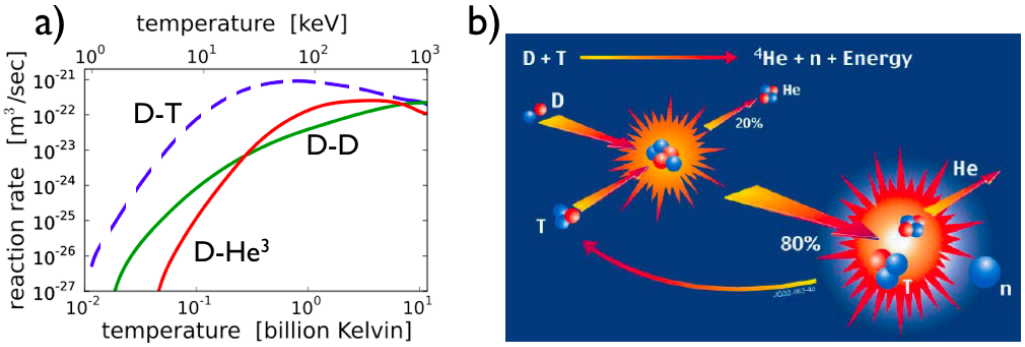

Figure 1.3: In a) the cross section of some fusion reaction. The reaction involving deuterium and tritium (dashed) is the most convenient. In b) a schematic of the reaction 1.2.

About the availability of the fuels, the Deuterium resources on Earth are practically endless, 0.0015% of hydrogen atoms in water being Deuterium, even though extraction methods are not yet affordable. Tritium is an hydrogen isotope which, even if is not present in nature due to its radioactive half-life of 12.3 years can be obtained from a transmutation from Lithium, whose resources are abundant in the Earth crust.

The Burning Criteria

For the balance of a fusion reactor to be positive, the energy produced by fusion reactions has to exceed that required to create and sustain the plasma itself, also accounting for the energy losses for emission of radiation (bremsstrahlung), or confinement degradation. Let Define the bremsstrahlung losses as $P_b = bn^2T^{1/2}$, where b is a function of the effective charge $Z_{eff} = n^{-1}\sum_i n_i Z_i^2$ in a multi-species plasma, T and n the plasma temperature and density respectively. Analogously for the heating power P_t that should be introduced in to the plasma to reach the fusion temperature the relation $P_t = 3nT/\tau_E$, hold, with τ_E the energy confinement time. The energy produced by the fusion reactor can be defined as $P_n = W_{DT}n^2 < \sigma v >_T /4$ where $W_{DT} = 17.59$MeV is the energy released after a single $D-T$ fusion reaction, and $<?v>_T$ is the product of the reaction cross-section and the relative velocity of the reactants averaged over a Maxwellian velocity distribution. Hence, assuming that the reaction power P_n balances the energy losses with an efficiency η. The self-sustainment condition will be:

$$P_b + P_t \leq \eta(P_b + P_t + P_n), \tag{1.3}$$

or

$$n\tau_E \geq \Big(\frac{\eta}{1-\eta}\frac{W_{DT}}{4} < \sigma v >_T - bT^{1/2}\Big)^{-1}. \tag{1.4}$$

This last expression is also known as Lawson's criterion [7] containing the 3 figures of merit most important for fusion reaction to occur: confinement time, plasma density and temperature. The most probable reactor scenario is one in which the α particles (^4_2He nuclei) produced by fusion reactions are confined by the magnetic field and replace all the energy losses by transferring their energy to the plasma, whereas neutrons escape the plasma volume and their energy is converted to electric energy. In this case, the Lawson's criterion must be modified; it is called *ignition criterion* and is written as $P_b + P_t \leq P_\alpha$ which can also be expressed as:

$$n\tau_E \geq 3T\Big(\frac{W_\alpha}{4} < \sigma v >_T - bT^{1/2}\Big)^{-1} \tag{1.5}$$

where $W_\alpha = W_{DT}/5$ is the energy of a single α particle after a fusion reaction. This ignition curve has a minimum at $T_i \simeq 20keV$. Isolating the temperature dependence in the right term of equation 1.5 we obtain the classical form of the so called *triple product*:

$$n\tau_E T_i \geq 3 \cdot 10^{21}[m^{-3}keVs]. \tag{1.6}$$

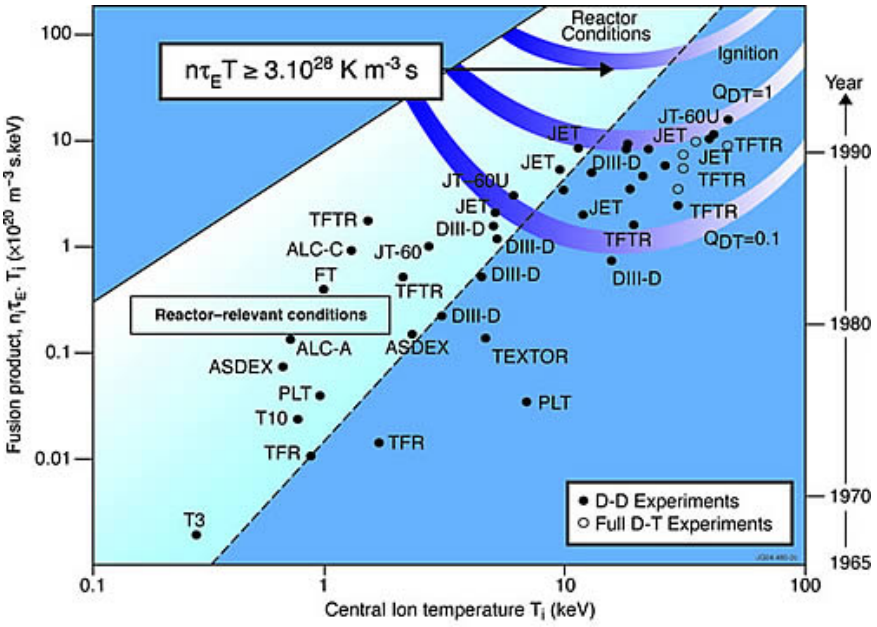

Figure 1.4: Values of the fusion triple product as a function of ion temperature for existing experiments in D-T reactions.

Figure 1.4 shows the values of the triple product reached in fusion devices since the beginning of experiments in plasma physics. From the right side axis it can be seen how the efforts profuse in the fusion research produced result more and more encouraging in the last decades, also if a major step, demonstrating the feasibility of a nuclear fusion reactor is still missing.

1.2.1 ITER

Conditions approaching ignition have been achieved in only in recent years in plasma confined in the so called *tokamak* configuration. The word tokamak, comes form the russian acronym meaning *toroidal chamber with magnetic coils*, which already gives an idea of its functioning. In this device, in fact, the plasma is confined by means of strong magnetic fields created by some coils surrounding a toroidal vessel. The magnetic field is arranged in order to obtain helical field lines which the goal to contain the losses of particles. The experiments performed in the russian laboratories in '60 and '70 on this kind of configuration made the tokamak magnetic-containment concept became the dominant approach in the fusion programs of all major industrialized countries. The large experimental database obtained in

ITER Parameters		
Fusion Power	500	[MW]
Power Amplication (Q)	≥ 10	
Major Radius	6.2	[m]
Minor Radius	2	[m]
Machine Height	26	[m]
Machine Diameter	29	[m]
Plasma Volume	837	$[m^3]$
Maximum toroidal field	5.3	[T]
Plasma Current	15	[MA]
Pulse length	≥ 400	[s]

Table 1.1: Main Parameters of the ITER Tokamak.

the last decade in tokamaks and other toroidal configurations, and the improving capability of numerical simulations have provided the international community the physics basis for the design of a burning plasma experiment based on the tokamak concept: ITER. The name is the acronym for International Thermonuclear Experimental Reactor, but it means also *the way* in latin, because it is also considered the experimental way towards controlled fusion as a peaceful power energy source. On November 21, 2006, the seven participants (European Union, Japan, Russian Federation, People's Republic of China, South Korea, India and United States of America) formally agreed to fund the project, whose program is anticipated to last for 30 years - 10 years for construction and 20 years of operation. The site preparation is in progress and the first plasma operation is expected in 2018. The table 1.1 reports the ITER characteristics. ITER would offer the possibility of studying several reactor relevant scientific and technological issues, which are beyond the present experimental capabilities. The principal aims of ITER are:

- The fusion of 0.5 g of deuterium/tritium mixture in its approximately 840 m^3 reactor chamber;

- To achieve extended burn in inductively-driven plasmas with $Q = Q_{fus}/Q_{aux} \geq 10$. where Q_{fus} is the the energy gain by fusion and Q_{aux} the energy needed by auxiliary systems to heat the plasma. This point must be demonstrated at nominal fusion power output of about 500 MW for a range of operating scenarios and with a duration sufficient ($\simeq 400$ s) to achieve stationary conditions;

- to aim at demonstrating steady state operation using non-inductive

current drive with a ratio of fusion power to input power for current drive of at least 5;

- the possibility of high Q operation exploitation, if favorable confinement conditions can be achieved.

A schematic of ITER is reported in figure 1.5. In many case the same compo-

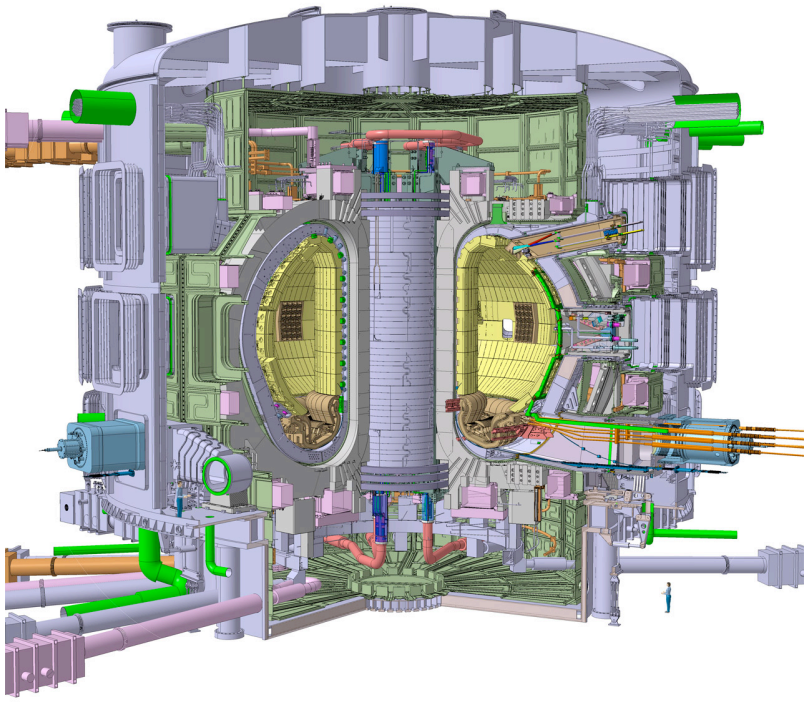

Figure 1.5: Schematic of ITER

nent is developed by several countries together. This will help the cooperation and the synergies, and allow more country to acquire knowledge on different part of the device. This point will be fundamental in future perspective. ITER is predicted to produce inductively driven D-T plasmas. These plasmas will be with density $n_e \simeq 10^{20}$ and core electron and ion temperatures of $T_e \simeq 8.8$ keV and $T_i \simeq 8$ keV. New physical regimes and a variety of technological issues will be explored with ITER. For example, conditions in which the α particles contribute significantly to the plasma pressure, with a class of plasma instabilities which can be studied in depth only with this new device. Again, a variety of technological issues could also be studied in ITER, like the test of advanced materials facing very large heat and particle fluxes, the

test of concepts for a tritium breeding module, the superconducting technology under high neutron flux and many others. The auxiliary systems needed to achieve the conditions expected in ITER are an external heating and current drive capability of 73 MW and several advanced diagnostics for both analysis and plasma control. All of these requirements are expected to solve many of the scientific and engineering issues concerning a burning plasma and could allow to make a straightforward step towards the demonstration of a tokamak power plant.

1.2.2 Auxiliary Heating and Current Drive

In order to have sufficient fusion processes occurring, the confined plasma must be bring to extremely high temperature, $T \simeq 10$ keV.
The fist direct way causing a temperature increase is intrinsic in the tokamak operation. The helical shapes of the magnetic field lines, in fact, are obtained by the superposition of 2 fields contribution, one in the poloidal, the other in the toroidal direction; The poloidal field is obtained by using the plasma as a conductor and forcing large amount of current to pass trough it, generating a consequent magnetic field. This *plasma current* will additionally heat the plasma by ohmic heating, according to $P_{Ohm} \propto I^2 \cdot R_p$, P_{Ohm} being the power produced, I_p the plasma current and R_p the plasma resistance. Hence the heat generated depends on the resistance of the plasma and the intensity of the current. Unfortunately as the temperature of heated plasma rises, R_p decreases and ohmic heating becomes less effective. It appears that the maximum plasma temperature attainable by ohmic heating in a tokamak is about 2 keV. To obtain still higher temperatures, additional heating methods must be used.
One way is radiating electromagnetic waves into the plasma. Carefully choosing the frequency of the generator to coincide with a characteristic frequency of the plasma, the power electromagnetically radiated into the plasma is transferred to the charged particles, which in turn collide with other plasma particles, thus increasing the overall temperature. This process is called *radiofrequency heating*. The second option is to fire very energetic particles into the machine, where they will transfer their momentum to the plasma particle by collisions. This second method is known as neutral beam injection. Notice that, both of this method are also able to produce large current drive, very effective in order to initiate, sustain and control the largely-self-heated fusion burn and to optimize the plasma current profile and sustain the plasma current during long-pulse/steady state advanced performance operation. A schematic of the Heating and current drive system is reported in figure 1.6.
The neutral beam injection heating is the most important topic of this thesis

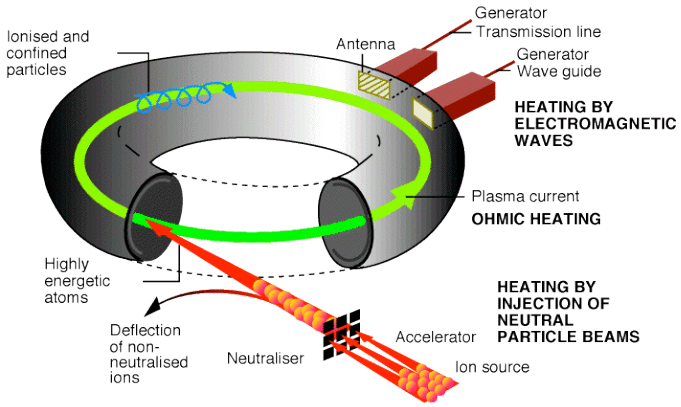

Figure 1.6: Schematic of an heating and current drive system featuring radio-frequency antennas and neutral beam injection.

work, and will be treated more in detail in the next section.

1.3 Neutral Beam Injection

A neutral beam injector (NBI) is able to heat plasma by firing it with dense beam on neutral particles. Since the injected particles have no charge they can penetrate the strong magnetic field devoted to confine the plasma, and transfer their energy to the plasma particles, increasing the overall temperature. The injection of such beams, moreover, increase the efficiency of the current drive, and the transition from a low level of confinement of the plasma (L mode) to an enhanced confinement scenario (H mode).
A beam of neutral particles can only be created in indirect way: since neutrals are not subject to electromagnetic fields, in order to give them the energy required to effectively heat the plasma, in principle they are generated as positive or negative ions inside an ion source. Then they are accelerated as an ion beam by means of strong electric field between different grids of an electrostatic accelerator, and only at this point they are neutralized in charge exchange processes with a neutral gas stripper. The neutral beam is then filtered of the ions which did not get the neutralization by means of strong magnetic field inside a so-called Residual Ion dump (RID) and finally directed toward the tokamak chamber. As the neutrals enter the plasma, they are quickly ionized and remains trapped by the magnetic field of the device. The choice of the beam particle species is constraint by the fact that

injected particle must not pollute the confined plasma, mainly composed by electrons and ions D^+ (or H^+ in the first experimental phase of the device), for this reason the beams are formed with D^0 (or H^0) particle. The ions created in the source can be either positive or negative. Even if the majority of existing neutral beam injector exploits the acceleration of positive ions, in the perspective of an highly energetic beam, as it is the case for ITER the use of negative ions appear compulsory, due to their high neutralization efficiency at high energy, as reported in figure 1.7 ITER will be equipped with

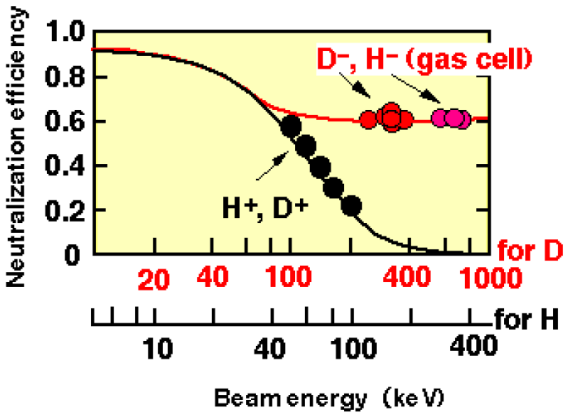

Figure 1.7: Neutralization efficiency for positive and negative deuterium and hydrogen ions against beam energy per nucleon

two neutral beam heating and current drive injectors, each one delivering a deuterium beam of 16.5 MW with particle energies of 1 MeV, and able to operate for long pulses of up to 3600 seconds. A third neutral beam line will inject a 100 keV, 1.5 MW hydrogen beam for diagnostic purposes.

1.3.1 The Padova Neutral Beam Test Facility

In the framework of the activity planned by the ITER Organization for the research and development of the NBIs (construction, operation, solutions for its problems) The *Consorzio RFX* in Padova was chosen to host a test facility, called PRIMA (acronym for *Padova Research on ITER Megavolt Accelerator*); it will includes two experiments: a full size plasma source with low voltage extraction and a full size NBI at full beam power (voltage up to 1 MV). The first experiment is called SPIDER (acronym for *Source for Productions of Ions of Deuterium Extracted from a Radio-frequency plasma*) while the second is called MITICA (*Megavolt ITER Injector and Concept*

SPIDER Parameters			
Ion Species	$\mathbf{D^-}$	$\mathbf{H^-}$	
Power	≤ 1	≤ 1	[MW]
Beam Energy	100	100	[keV]
Beam Current	40	60	[A]
Extracted current density	285	355	$[A/m^2]$
Pulse length	3600	3600	[s]
Source filling pressure	0.3	0.3	[Pa]
Extracted electron to ion ratio	≤ 1	≤ 0.5	

Table 1.2: Main parameters of the SPIDER source.

Advancement).

SPIDER

SPIDER is the first experimental device to be built and operated, aiming at testing the extraction of a negative ion beam (made of H^- and in a later stage D^- ions) from an ITER size ion source. A sketch of its design is reported in figure 1.8, while the main requirements are resumed in table 1.2

The extraction and accelerator system for the SPIDER ion source, is composed of three grids: the Plasma Grid (PG), the Extraction Grid (EG) and the Grounded Grid. The gap between the grids and the hole aperture are important parameters to allow a proper focus to the extracted beam. The PG, directly facing the plasma is required to operate at a temperature of about 150 ^oC in order to enhance the cesium effect for negative ion surface generation (see section 2.2). Moreover, it is Molybdenum coated on the plasma side to reduce the sputtering yield. The apertures are designed with conical chamfers on the upstream and downstream sides of the grid. To reduce the unavoidable co-extracted electron current a polarization of the plasma grid respect to the plasma potential is applied. Moreover some suppression magnets are embedded in the extraction grid to deviate the trajectories of the co-extracted electrons, forcing them to collide with the EG surface. The EG has an electric potential higher than the PG (depending on the extracted current density), so that the negative charged ions can be properly extracted from the RF expansion chamber. The GG has the function to accelerate the ion beamlets up to a potential of about 100 kV, and is also loaded by co-extracted and stripped electrons. Each grid of the ITER NBI is divided in 4 segments, each with 320 apertures for a surface of 2000 cm^2. Each segment contains 4 groups of apertures arranged in a regular 5 x 16 rectangular

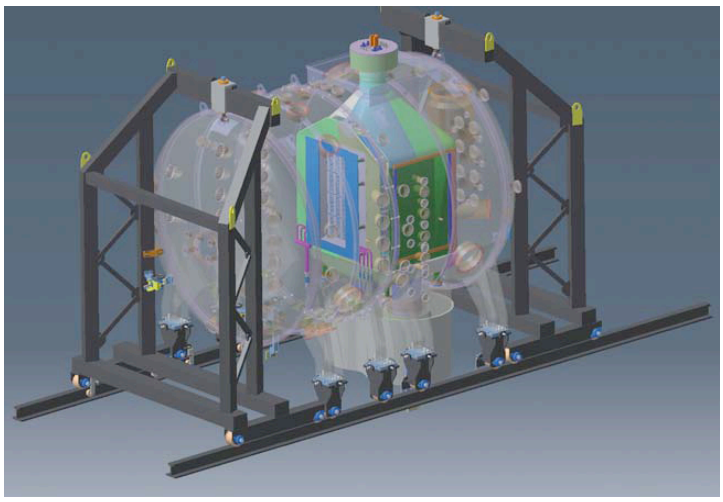

Figure 1.8: Sketch of the SPIDER sorce

array. All the grids are made by electrodeposition of pure copper onto a copper base plate. This technique permits to obtain a very complex geometric shape (with very small cooling channels that run inside the grid and grooves for embedded magnets) and to have good mechanical properties, due to the high purity and to the very small grain size of copper. The power loads on the EG and GG are expected to be quite high and concentrated, hence they are critical from the structural point of view, and require high performance cooling systems. In the last design update SPIDER was also equipped of a electron dump system, consisting of consecutive arrays of cooling pipes, just at the end of the accelerator stage, devoted to dump the high divergence particle contained in the beam before they damage more delicate structures. The main objectives of SPIDER will be to demonstrate the feasibility of extraction form large ion radio-frequency sources, presently only tested on small size source (BATMAN source at IPP Garching [8]), focusing on current density values and uniformity together with the containment of electrons leakages. In particular the electron to ion ratio should be limited to less than 1 and the admissible ion inhomogeneity, extracted from the grids, should be better than 10 % on the whole plasma cross-section, having a surface exposed to the extraction grid in the order of 1.5 m^2. Most of this studies can be performed thanks to instrumented calorimeter, a particular diagnostic system intercepting the beam after the acceleration stage, and giving information on beam uniformity and divergence and current values. Another SPIDER requirement is the production and extraction of a negative ion plasma for

MITICA Parameters			
Ion Species	$\mathbf{D^-}$	$\mathbf{H^-}$	
Beam energy	≤ 1	≤ 1	[MW]
Acceleration Current	40	60	[A]
Extracted current density	285	355	$[A/m^2]$
Beamlet divergence	≤ 7	≤ 7	[mrad]
Beam on Time	3600	3600	[s]
Source filling pressure	0.3	0.3	[Pa]
Extracted electron to ion ratio	≤ 1	≤ 0.5	[-]

Table 1.3: main parameters of MITICA injector.

one hour, assuring the beam modulation required by ITER full power and diagnostic beam operation. Finally, the capability of optimization of the cesium consumption and the tolerance to the presence of impurities have to be studied. The plasma source is based on the RF concept, including eight RF drivers, operating at 1 MHz. More information on plasma sources will be given in chapter 2.

MITICA

MITICA is a full size heating neutral beam injector, designed to answer all the requirement of the real ITER injector. The main parameters of the experiment are reported table 1.3. Differently form the case of SPIDER where more flexibility was allowed, in MITICA most of the technic specifications are strongly connected to the problem of optimizing the interaction with the ITER plasma. For instance the energy parameters for the beam must satisfy the need to penetrate plasma up to its internal region, where the heat is efficiently deposited. It is known, in fact, that the ionizing cross section of the beam decreases with the beam energy, hence, in order to allow the beam to reach the plasma core without be completely ionized before an high beam energy is required. Nonetheless the beam energy value is limited by the need of minimizing the fraction of surviving neutral beam reaching the internal wall of the device vessel. Moreover high voltages need very high insulating distances, while the dimension of the injector are fixed to do not exceed the ITER duct dimension. For this reason a value of the beam energy around 1MeV was selected as the best choice. With this acceleration voltage and considering the various lost factors, it was estimated that the power delivered from each injector should be around 17 MW. Considering the extraction surface the requirement on ion current density is obtained, as reported in the

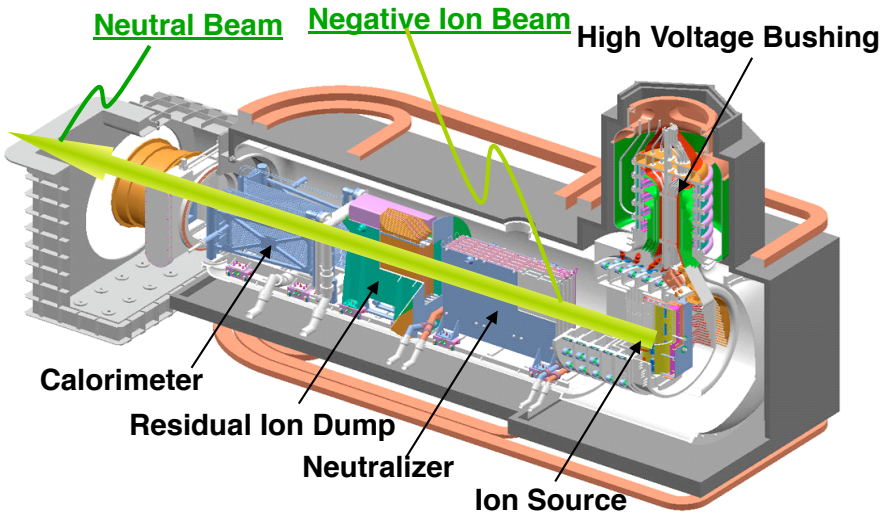

Figure 1.9: Sketch of the MITICA injector

previous table.
Differently for SPIDER, MITICA also include other typical NBI components, as the Neutralizer where reaction of charge exchange between the beam ions and the neutral gas occurs, and the Residual ion dump devoted to remove the fraction of charged particles still present in the beam.

A schematic of MITICA, including all the mentioned components is given in figure 1.9.

Chapter 2

Ion Source

The charged particles fueling the beam are created inside an ion source. Most ion sources for magnetic fusion are based on the formation and confinement of a plasma at the heart of the source [9]. The properties and features of this plasma determine to a large extent the kind of ion beam that is produced. The ions are extracted from the source by means of an *extractor* where the ions in the plasma are extracted by means of an electric potential, forming the beam. Usually the extractor is constituted by a grid, causing the extraction of particles in the form of several beamlets, rather than a single large sized beam. Then, the full beam is obtained by superposition of such beamlets far away from the source. Due to the high current density required in fusion applications the extraction area, and thus the whole accelerator size, are very large. This aspect, together with the large power they produce makes the great difference with respect to typical ion sources used for other purposes. As already mentioned, in the perspective of a high energy neutral beam, due to the low neutralization efficiency of positive ions, the use of negative ion based plasma sources appears compulsory. The creation of negative ions add a high degree of complexity to the physics of the source; this chapter will give an overview of the atomic and molecular processes involved in their formation, also describing some numerical tools developed to help the modeling of the source and the interpretation of experimental data.

2.1 Plasma Formation and Confinement

The way in which the plasma is formed is a characteristic of the type of source. in particular, for applications in neutral beam injectors two concepts have been developed:

- *Arc driven* ion source, where the plasma is produced via ionization of the background gas by electrons created in an arc discharge between some filaments (hot cathodes) and the source body (anode).

- *Radio frequency driven* (RF) ion source [10] in which the discharge ionizing the gas is generated by an induction coil, the *antenna*. The electrons contained in the gas, subject to oscillations imposed by the RF electric field of the coil, gain enough kinetic energy to ionize the background gas and to form the plasma.

  The use of RF sources in the context of neutral beam injection, firstly proposed by IPP Garching, presents some important advantages with respect to the filament sources. In particular the main disadvantages of the arc driven sources is that their filaments need to be changed often, due to tungsten consumption, which can also pollute the plasma , while the RF operations are intrinsically maintenance-free and " cleaner", Moreover, due to its nature, RF sources seem to exhibit a better plasma homogeneity. For these reasons, notwithstanding the large experience on arc driven sources, whose efficiency was proved in many test beds, also for large extraction experiments (especially in Japan, the only country were negative ion based injectors operate so far), the RF source was preferred for the final design of the ITER NBI [11].

The confinement of the plasma inside the source is usually magnetic, exploiting the use of permanent magnet arrays mounted on the external part of the chamber and arranged to form a multipole configuration. The resulting magnetic field has high intensity close to the walls and rapidly decays with distance from the wall, to contain the plasma losses and increase the overall source efficiency. A schematic of a permanent magnets arrangement confining the plasma is shown in figure 2.1.

2.2 Negative Ion Production

The physical mechanism of negative ion production involves the capture of electrons into an electron affinity level of an atom or molecule. In the case of a confined plasma, two different electron sources can be distinguished: the most obvious is the plasma itself which contains large amounts of free electrons which can attach to neutral particles (volume production); the second source can be identified with the shift of electrons from the conduction band of the metals surfaces surrounding the plasma toward the electron affinity level of the particle approaching the walls (surface production) [12],[13].

2.2.1 Volume Production

The negative ion production inside the plasma volume was investigated since 1970 by several authors [13],[14],[15],[16] who described the formation of a negative ion in terms of a two-steps process. According to them, the negative ions are supposed to be generated by a process of dissociative attachment (DA) between a molecule of gas and a low energy electron, according to the reaction:

$$e + X_2 \rightarrow X^- + X \tag{2.1}$$

The cross section of this reaction is low if the molecule is in the ground state, and it is increased by a factor of five when X_2 has a sufficient degree of vibrational excitation [15],[16]; for this reason I will refer to reaction

$$e + X_2(\nu \geq 5) \rightarrow X^- + X \tag{2.2}$$

rather than 2.1 in which X_2 is in ground state. It is thus evident that a preliminary step is required to vibrationally excite the molecule. The most effective way to change the vibrational state of X_2 is by means of an electron collision in the so called e-V reaction:

$$e + X_2(\nu) \rightarrow e + X_2(\nu') \tag{2.3}$$

tough very common, in most cases this reaction only realizes small transitions between the vibrational levels of X_2, and could in case cases even decrease the excitation level: $\Delta\nu = v - v' = \pm 1$. To be more effective this reaction should exploit the intermediate channel,

$$e + X_2 \rightarrow X_2^* \tag{2.4}$$

in which the X_2 is electronically excited to a metastable singlet state (B,C,..)[1] from which it decays in an electronically ground level, acquiring a vibrational excitation, and with a photon emission:

$$X_2^*(B, C) \rightarrow X_2(X, \nu' \geq 5) + \gamma \tag{2.5}$$

The whole process of 2.4 and 2.5 goes under the name of E-V reaction [17],[18] and was experimentally confirmed to be the greatest source of highly vibrationally excited molecules.

The DA reaction 2.2 needs the capture of an electron with low energy ($E \approx 1eV$), whit respect to the energy needed in reaction 2.4 to excite the molecule($E \geq 10eV$); moreover the newly created H^- lifetime is greatly

[1] A good description of the basic spectroscopy involved can be found, for example in [8]

shortened by the presence of energetic electrons, which easily can destroy the ion. For that reason the volume production negative ion sources are equipped with some kind of filter to separate 2 electron population, depending on their energy. The first realization of this point exploited a two chamber structure of the source (*tandem concept*), but in the last years a simplest solution was preferred, constituting in using a transverse magnetic filter close to the plasma grid, was preferred (*filter field*). Fast electron produced in the plasma region by the RF coil are reflected back by the magnetic filter field, with a mechanism similar to the the wall reflection caused by the multipole array. On the contrary, cold electrons throughout the filter field lines, since they are much more collisional. The direct consequence of this effect is that the average electron temperature falls rapidly with distance perpendicular to the filter field. The schematic of the process is reported in figure 2.1.

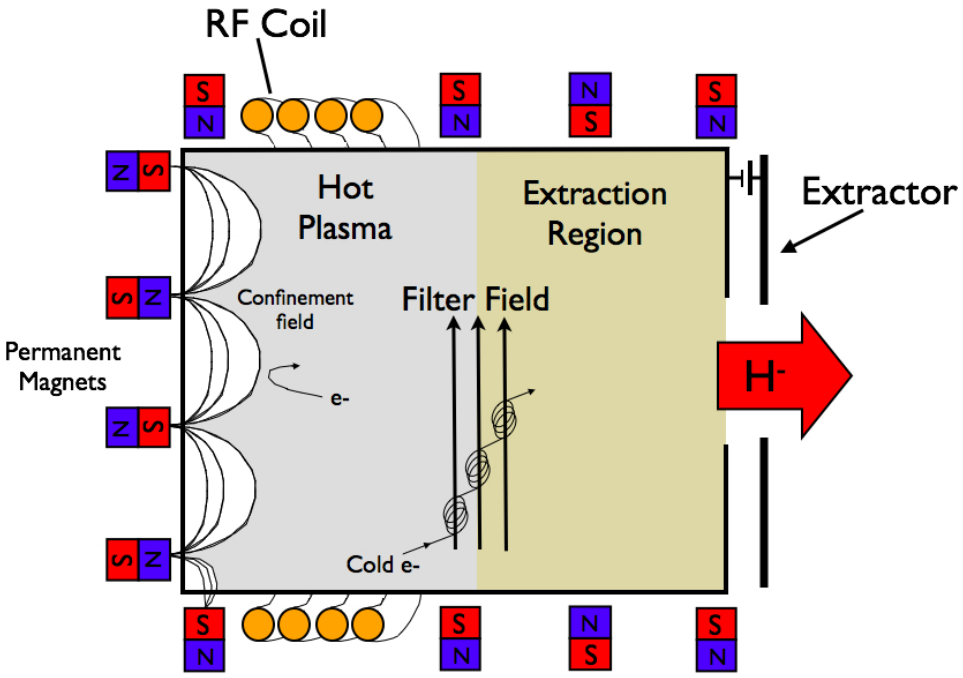

Figure 2.1: Schematic of a RF negative ion source. Note the presence of the confinement fild produced by permanents magnets array devoted to confine the plasma, and the filter field, preventing hot electrons to reach the extraction region.

An atom impinging on a wall of the source has a certain probability to be re-emitted as a negative ion. This probability becomes relatively high if

the metal constituting the wall has a low work function, since the energy of the Fermi level of the metal is comparable to the electron affinity level of the atom approaching the wall, and electrons tend to be captured by tunneling. A standard technique to lower the work function of the metals surrounding the source is covering the walls with some layers of cesium, which has the lowest work function of all metals (1.8 eV). Modern negative ion sources are equipped with cesium ovens, to obtain the depositions on walls by evaporation. Note that the dynamic of the cesium in the source is quite complex, and in some situations can change the potential distribution in the source or affect the currents of electron extracted from the source [19],[20] However these subjects are outside the scope of the present thesis.

2.3 Atomic and Molecular Processes and Databases

In the previous section, for the sake of simplicity, only the most basic reactions responsible for the formation of negative ions were mentioned. The real situation involves thousand of interactions between material surfaces, atoms and molecules which can also be found in their exited states. In particular the existence of rotational, vibrational, and electronic states for the molecules increase considerably the degree of complexity of the system. Nonetheless, considering that the volume production is strictly connected with the internal excitation level of molecules, this aspect cannot be omitted. The knowledge on these processes are useful to both help the interpretation of experimental results, and to help the modeling of the source, as well as of the whole injector. In the case of deuterium reactions a lot of information on this kind of reactions are missing, and even if the databases of known collision reactions of hydrogen molecules and ions are large the data are sometimes incomplete or controversial, and dispersed in several articles, books or online databases [21],[22],[23]. With the scope of constituting as detailed as possible reactions occurring in an injector database of practical information on the possible reaction occurring in a injector the assembling of a database was started within the present thesis work, and its implementation in structured numerical variables is well in progress. Note that the degree of complexity of such a database is governed by the interaction occurring in the source, while in the acceleration, drift and neutralization stage of the device the processes can be simply grouped in collision of high energy beam ions (or neutral) with the almost static background gas, as we will see in chapter 4.
The fundamental quantity collected in the database is the cross section, ex-

pressing the likelihood of interaction between particles. In some databases, on the contrary, the interaction is described by means of a rate coefficient, defined as:

$$R_X = \int_0^\infty v(E)\sigma_X(E)f(E)dE \tag{2.6}$$

where R_X is the rate coefficient of the X interaction, σ_X the corresponding cross section, v the relative speed between particles and f is the normalized energy distribution. The choice of using the cross section leaves to the user the possibility of obtaining the rate coefficient for every kind of energy distribution function different from the canonical Boltzmann expression.
The energy range of interest is extremely small for the majority of reactions occurring in source, where the electron energy stays below $\simeq 20$ eV, and the ion range is even smaller, going from 0 to about 5 eV, but for the beam reaction the range becomes huge, since in the perspective of future development of NBIs for fusion power plant the ion energy is expected to reach 2 MeV.
As a first step a list of all the expected reactions in the injector was prepared, without considering the relative importance of a reaction with respect to another. This list, featuring more than one thousand reactions is reported in the appendix C for the case of hydrogen. In that case the family of considered reactant involves, listed for ascending mass order: electron, H^+,H^0,H^-,H_2^+,H_2,H_2^- and H_3^+.
In a second step an exhaustive search of reliable data was performed to fill up that list, scanning all known databases, and asking for the collaboration of other laboratories. In some cases data coming from different sources were compared and eventually joined. An example of this kind of situation is given by the reaction of electron detachment:

$$H^- + H \rightarrow H + H + e. \tag{2.7}$$

Two different sources were found for the same reaction, the first from the ORNL report compiled by Barnett [23], the second in a work by Janev [21]. Even if the two energetic ranges were different, an overlapping of data was present in the middle range energy. In this case the data were recorded in the database in a way to match the data from both authors, and to join them smoothly, as reported in figure 2.2. In other cases, the fulfillment of data required more efforts. A particular case is the reaction of double charge exchange:

$$H^+ + H^- \rightarrow H^- + H^+. \tag{2.8}$$

Data for this reaction are available from many sources [24],[25],[26], but none of them gives the data for low energy range $E < 60$ eV. Since the reaction is particularly important exactly in that missing energy range some adjustment

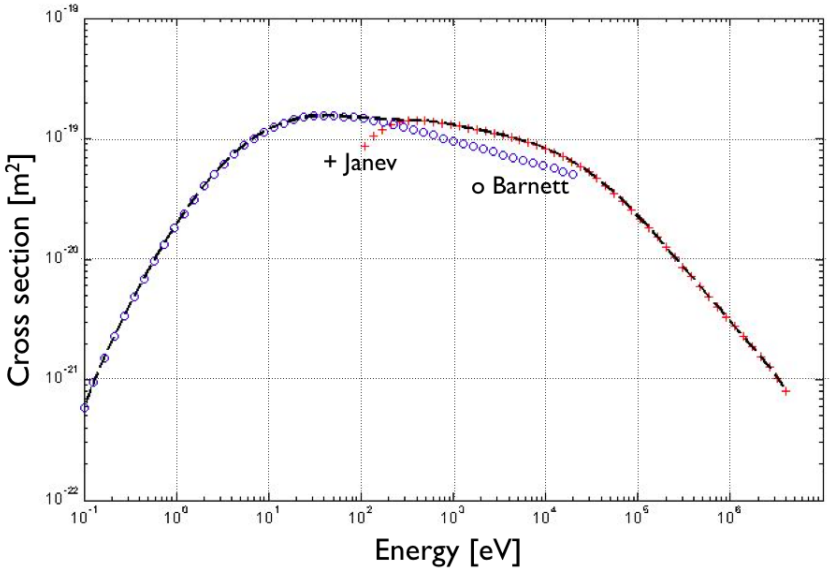

Figure 2.2: Cross section data for the reaction 2.7. The dotted line correspond to the data recorded in to the database.

appears necessary before implementing the cross section into the database. A solution consist in the fact that due to the indistinguishability of particles before and after the impact, reaction 2.8 can be seen, at least at low energy, as a simple elastic collision between particles. Hence the proposal was to join together the data of charge exchange with the one of elastic collisions. The results are plotted in figure 2.3.

The collected data were recorded in special tables in simple text format, so they are available to be read from many different programming languages. In the present state the implementing routine, translating this data table in the form of structured variables was written in MATLAB [27] environment. These structured variables act as boxes in which the data can be organized in categories. One example is the subdivision according to reaction type, defining the particular process involved, like *ionization, electron detachment, atomic or molecular excitation* and *dissociation*. Moreover the reactant and products of the reaction can de identified optionally by the fraction of energy they carry with respect to the other particles involved as slow or fast particles. In the standard 2 bodies reactions, in fact, the process is interpreted as a collision between a projectile particle and a target. All the energy is assumed to be carried by the projectile particle, considering the target at rest. This is particularly suitable for the beam reaction, where the dynamics

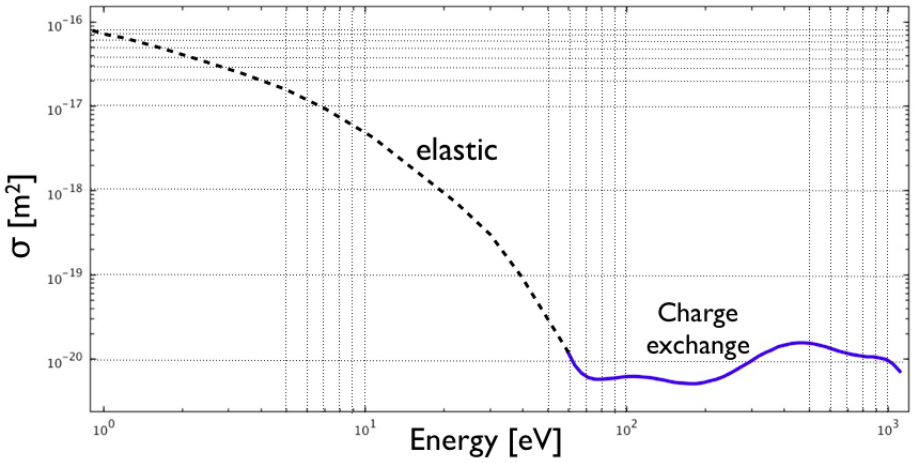

Figure 2.3: Cross section data for the reaction 2.8. The charge exchange data is obtained from reference [24] and then joined with the cross section of elastic collision.

of the interaction is very likely this one. If this subdivision of particle depending on their velocity is important for reactants, for the products of the reaction this is even more true; for instance, in modeling some beam related processes, the initial velocity of a particle produced in a reaction determines its contribution to the space charge, as it is the case for the simulations on space charge compensation, reported in section 4.1.2. Another option of the structure of the database is the possibility to label each reaction with a particular "importance" index. This is helpful, for instance, when the database is used to directly feed numerical code of thermodynamic equilibrium or collisional radiative models, allowing to deactivate a whole class of reactions by setting their importance index to 0.
Together with this routines devoted to write the database in numerical format, a large collection of other macro were written to support the consultation of the database. One of them is devoted to search the reactions by parameters: allowed keys include one or more reactants or products, the reaction type and the particle velocities. Crossed search are also possible and the final data are automatically plotted and compared to each other. Figure 2.4 reports a sample result of a database search for the impact of hydrogen (as H^+,H^0 or H^-) against H_2 target.

Further routines are dedicated to the conversion of cross sections into reaction rates, according to 2.6, by suitable choice of the energy distribution function$f(E)$, or to simple unit of measures conversion. Macro to export

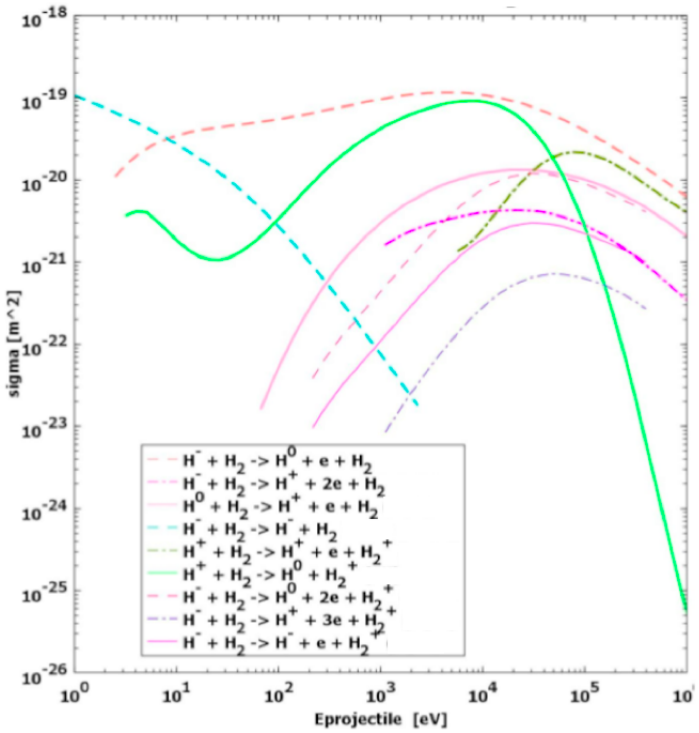

Figure 2.4: Cross section data for the reaction 2.8. The data is obtained from [24] joined with the cross section of elastic collision.

one or more reaction data to universal simple text tables are also available allowing great flexibility of usage. Even if the database assembly is still ongoing it was already used in many modeling application: the Bypo code, for instance, which will be described in section 3.4, can import data from the database to calculate the beam attenuation in the accelerator and to account for the secondary production in beam-gas interaction.
Moreover a kind of collisional radiative model to estimate the fraction of particles present in the source and the populations of their excited states was developed having a direct interface with the database. This model is still under development, and its description is outside the scope of this thesis.

Chapter 3

Beam Extraction and Acceleration

This chapter will analyze the problem of the extractions of the ions from an ion source, and their successive acceleration as a beam. In most ion sources for fusion applications, the ions are extracted from the free boundary of a plasma facing the acceleration region. As in the case of interactions with surface materials, also at this free boundary the plasma develops a charged transition layer to preserve its internal neutrality. This layer is known as *sheath*, and the first section of this chapter is intended to give an overview of the problem of its formation, addressing the main points of interest, and citing the relative published articles. A detailed analytical description of the phenomena is only given for a simple mono-dimensional case in section 3.2. Then, the section 3.3 will present the problem of the extraction of the ions from the plasma, and the beam formation and acceleration. In this context, a particular model will be presented and accurately described.

3.1 The Sheath Problem, an Overview

The problem of sheath formation was studied since the pioneering studies on plasma by I. Langmuir on plasmas [28],[29]. Since the subject is complex and still debated, it seems useful to give in this section an insight to the problem of the formation of a the sheath of charged particles in the general case of plasma-wall interaction. More specific calculations will be performed where required.
Let's assume a collision-less plasma faces a conducting material. Due to their higher thermal velocity, electrons are the faster species to reach the boundary of the plasma, charging the wall with negative potential. As the potential

rise, a progressively larger fraction of the incoming electrons is reflected back from the wall, and the positive ion accelerated toward it. The process will evolve in a kind of equilibrium between the fluxes of electrons and ions. A sheath of positive charge will formed around the surface, shielding the conducting wall from the plasma potential. The typical width of this sheath is proportional to the Debye length λ_D, an important variable depending on plasma characteristics: $\lambda_D = \sqrt{T\epsilon_0/N_0e^2}$ with N_0 and T the plasma density and temperature, e the electron charge and ϵ_0 the vacuum permeability. By assuming that the potential in the plasma is constant $V = V_p$ and that it undergoes a steep fall in the sheath, as shown in picture 3.1, the existence of a condition on the ion velocity to allow their access in the sheath region will be demonstrated in a simple mono-dimensional case. Under the hypothesis

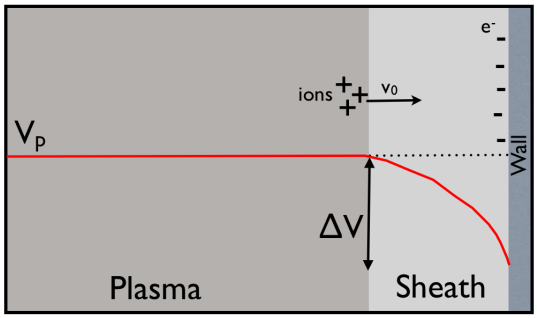

Figure 3.1: Schematic of the plasma wall interface showing the expected behavior for the potential.

that the ions will arrive at the plasma-sheath interface with a velocity v_0, their current density given by $J_i = v \cdot e \cdot n_i$, with v the ion velocity inside the sheath. Considering the quasi neutrality condition inside the plasma, $n_i = n_e$, and with the ion energies $eV_0 = Mv_0^2/2$ at the sheath plasma interface and $e(V_0 + \Delta V) = Mv^2/2$ inside the sheath, the ion density can be express as:

$$n_i = n_p \frac{v_0}{v} = n_p \sqrt{\frac{V_0}{V_0 + \Delta V}} \tag{3.1}$$

with n_p the common density of both species at the plasma boundary. For the electrons a Maxwellian velocity is usually assumed: $v_e = n_0 \exp(e\Delta V/KT)$, so that, under the hypothesis $\Delta V << V_0$ e $\Delta V << KT/e$ we can express both densities as:

$$n_i = n_p(1 - \Delta V/2V_0) \tag{3.2}$$

and

$$n_e = n_p(1 - e\Delta V/KT) \tag{3.3}$$

and inserting into the 1D Poisson equation;

$$\frac{d^2V(x)}{dx^2} = \frac{-e(n_i - n_e)}{\epsilon_0} \tag{3.4}$$

yielding:

$$\frac{d^2V}{dx^2} = -\Big(\frac{en_p}{\epsilon_0}\Big)\Big[\Big(\frac{e}{KT}\Big) - \Big(\frac{1}{2V_0}\Big)\Big]\Delta V \tag{3.5}$$

Now, from the behavior of the potential shown in picture 3.1 it is clear that the condition $d^2V/dx^2 > 0$ must hold. To guarantee this inequality we should impose:

$$V_0 > \frac{KT}{2e} \tag{3.6}$$

or, equivalently:

$$v_0 > \sqrt{\frac{KT}{M}} \tag{3.7}$$

known as *Bohm criterion*. The physical implication is that the ions must arrive at the plasma-sheath interface with a minimum velocity. This condition was derived using the simplest case of collision-less and generation-less plasma, anyway the existence of a condition of singularity on the ion velocity could be demonstrated both in the plasma and in the sheath region, for every general form of the terms of collisions and generation.
For the example of cold ions, in the plasma region, considering the ion momentum equation and the continuity equation:

$$\begin{aligned} \frac{d(n_i v_i^2)}{dx} + C &= \frac{n_i eE}{M} \\ \frac{d(n_i v_i^2)}{dx} &= G \end{aligned} \tag{3.8}$$

where C is the friction force experienced by ions per unit of volume due to collision with other plasma particles, G the generation term and $E = -dV/dx$ the sheath electric field. Using the same condition of quasi neutrality of the plasma and Boltzmann electron distribution, following for example [30] a linear system of equations for the quantity dn/dx and dv/dx can be derived, whose solution is:

$$\begin{aligned} \frac{dn}{dx} &= \frac{2Gv_i + C}{(v_i^2 - T_e/M)} \\ \frac{dv_i}{dx} &= \frac{Cv_i + G(v_i^2 + T_e/M)}{n(T_e/M - v_i^2)} \end{aligned} \tag{3.9}$$

again both singular for the ionic sonic velocity $v_i = \sqrt{T_e/M}$, disregarding the form of C and G.
A similar singularity is found in the sheath region in condition of negligible collisions and conservative particle flux ($C = G = 0$): Starting from the poisson equation in terms of the particle densities as a function of V, as in 3.5, we can define the normalized potential $\eta = -eV/T_e$ to get:

$$-\frac{d^2\eta}{dx^2}\frac{KT_e}{e} = -\frac{en_p}{\epsilon_0}\Big[\frac{e}{KT_e} - \frac{1}{2V_0}\Big] \tag{3.10}$$

now recognizing the expression of the Debye length λ_D and introducing also the adimensional coordinate $\xi = x/\lambda_D$ yields:

$$\frac{d^2\eta}{dx^2} = \Big[\frac{e}{T_e} - \frac{1}{2V_0}\Big]. \tag{3.11}$$

In the sheath the quantity $d^\eta/d\xi^2$ can be neglected, so that the condition

$$V_0 = \frac{KT}{2e} \tag{3.12}$$

is found again, at the sheath. The same equation can be found for the general case of non cold ions: (for the standard procedure, involving the Taylor expansion of the equation see, for example, [31])

$$\frac{d^2\eta}{d\xi^2} = 4y_0\big[\big(1+\frac{\eta}{y_0}\big)^{1/2} - 1\big] + 2\big(e^{-\eta} - 1\big) \tag{3.13}$$

with $y_0 = m_i v_0^2/2T_e$. Also here, to guarantee the positivity of the left hand term the condition $v \geq C_s$ must hold.

3.1.1 The Transition Layer

In principle we can conclude that the problem is well described by considering the plasma equation valid for $v < C_s$ and the sheath equation valid from the point in which $v \geq C_s$. However there exist a strong complication that behaves in the fact that the asymptotic behavior of the two equation is different as the ion velocity approach the sonic velocity, since:

$$\begin{aligned} &\frac{dv_i}{dx}\Big|_{v\to C_s} = 0 && \text{In the Sheath} \\ &\frac{dv_i}{dx}\Big|_{v\to C_s} = \infty && \text{In the Plasma} \end{aligned} \tag{3.14}$$

so the two equations are not joinable homogeneously. Different approaches were developed to overcome this problem, but two main methods can be identified:

The Matching

The studies developed with this method guess the existence of a transition region, the *pre-sheath*, which allows the connection of the two solutions in a homogeneous way. This is obtained by means of the method of the *matched asymptotic expansion*[32], initially introduced in the context of fluid mechanics by, Neyfeh [33]. Different authors applied this method to the plasma-sheath transition problem [34],[35],[36] and most of their works have in common the fact to identify the typical width of the transition region as

$$\ell = \lambda_D^k L_p^{1-k} \tag{3.15}$$

with $0 < k < 1$, λ_D being the Debye length and L_p the plasma width. Though Franklin and Ockendon [35] showed that this method is not able to give a uniform valid solution through the three regions, it allows to have a good estimation for the electric field, which is predicted to be proportional to $KT_e/(e\ell_R)$, ℓ_R being the width of the particular region. As an example, in [37] the value $KT_e/(e\lambda_D^{3/5}L_p^{2/5})$ is proposed for the field at the plasma border.

The Patching

This method suggests that the transition region is not necessary, and the solutions of the two equations can be joined smoothly. The reference theory, due to Godyak [38] [39], consists in the assumption that the plasma equation is valid up to a certain point at which the electric field value is supposed to be

$$E = \frac{KT_e}{e\lambda_D} \tag{3.16}$$

know as *Godyak condition*. The validity of this method is contested by Franklin [30] who compares the solution of the patching with the complete plasma sheath equation. It turn out that the method gives good results for some quantities, but for others, in particular the value of the field close to the wall, the results are not in agreement, since the request to have a potential fall in a shorter region gives an overestimation of the electric field. A revisitation of this method can be found in [40].

3.1.2 Effect of Collisions and Magnetization

Up to now I considered the case of a general, non-collisional, unmagnetized plasma. The effect of the collisions, in a sense, seems to simplify the problem, since, as showed in [41], the collisions makes not necessary the existence of a transition region between the plasma and the sheath. This point is

justified in [30], where the author guesses that, in presence of collisions, the plasma density at the edge drastically decreases, causing an increase in the Debye length, and making it impossible for the ions to reach the Bohm velocity, so that the transition layer can not be formed. For some other authors the collisionality simply modifies the Bohm criterion [42],[43]. In particular Valentini shows that the usual Bohm criterion is a condition sufficient but not necessary for the formation of the sheath of positive charge. Note that the generality of the Bohm criterion, for any kind of collisional term, was already showed in equation 3.9, in fact, in [30] Franklin concludes that also for a collisional plasma the sheath is formed, even if the Bohm criterion has no meaning, and he identifies a value of the velocity for which there is a transition from the collisional regime to an inertial regime. Finally, some studies were published about the velocity at which the ions reach the wall [44], with no reference to the transition layer.

The effect of the magnetization does not affect the sheath formation in case

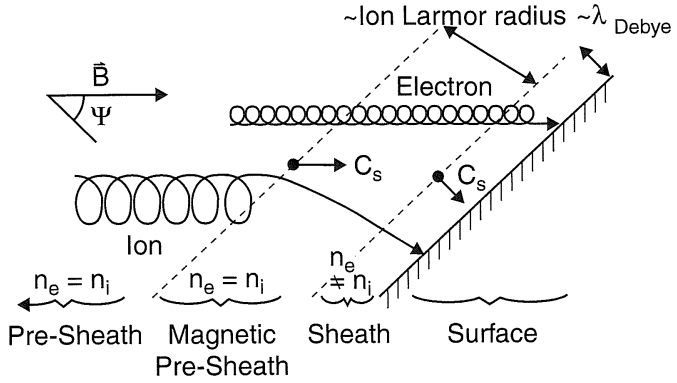

Figure 3.2: Schematic of the Plasma-wall transition in presence of a magnetic field, explaining the Bhom-Chodura condition. The picture was taken from [45].

of a magnetic field perpendicular to the wall [46], while the situation is more complicated in case of fields not normal to the wall. This kind of studies were introduced by Chodura in the context of the plasma-wall interactions inside the tokamaks [47] , [48] [49]. His theory guess the formation of a further layer, a *magnetic pre-sheath* between the classic pre-sheath and the sheath. The width of this layer is proportional to the ion Larmor radius and to the angle between B and the wall. In the same papers it is shown that a condition should hold on the velocity of the ions entering the magnetized

pre-sheath:

$$v_{//B} \geq C_s \tag{3.17}$$

at the interface between plasma and magnetic pre-sheath. This condition goes under the name of Bohm-Chodura criterion, and was also demonstrated with an alternative method in [50].

Since also the traditional Bohm criterion should hold at the entrance of the Debye layer, the magnetic pre-sheath has the function of transferring the ion velocity from the direction parallel to B to the direction perpendicular to the wall. This hypothesis is explained in figure 3.2

3.1.3 The Case of Electronegative Plasmas

In the case of plasmas containing also negative ions, and under the hypothesis of Maxwellian distribution for both negative ions and electrons [51],[52], the value of the potential at the sheath edge results to be a multivalued function. The reason is that the Bohm criterion is verified in more than one point [30]. The basic idea was proposed in [53], in the context of studies of a plasma containing two populations of electrons with different temperatures, guessing the formation of a double layer between the two plasmas; even if their calculations was non self-consistent the idea was accepted and reproposed in later works: in [51] is stated that for low pressure plasmas, different plasma regions could exist, each of them terminating with its own Bohm criterion, and the "coldest" species will also be the most confined. An interesting study, with similar considerations, is proposed in [54], which in its work also deals with the negative ion extraction. Finally, the work of Kono [55] treats the instabilities that arise in the case of low pressure electronegative plasmas.

3.2 Analytic Study of the Sheath Region

This section will present an analytical treatment of the sheath formation in the mono-dimensional case of a non collisional, non magnetized and non electronegative plasma formed between two plane parallel electrodes plates. With respect to the cases discussed in section 3.1 this is very general, but it can be helpful to have an insight of the standard procedures used to obtain the equations for the sheath and for the plasma region.
The case of a plasma formed between two plane parallel electrodes will be considered here, with the x axis having the 0 value in the center of the region, so that each electrode has a distance "a" from it. The potential $V(x)$

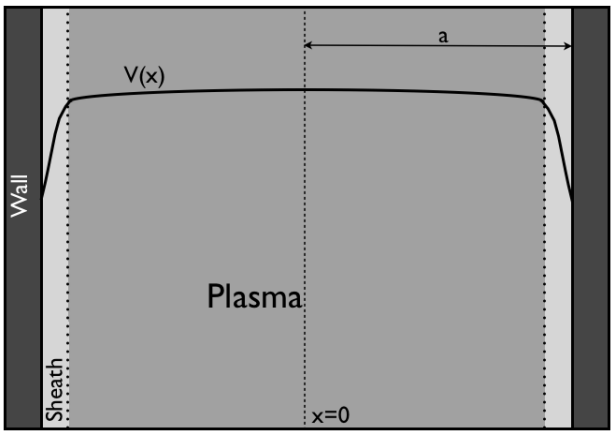

Figure 3.3: Schematic of the 1D potential behavior expected in a plasma facing two walls.

should satisfy the Poisson equation 3.4, where for the electrons, once again a maxwellian expression is adopted:

$$n_e = n_0 \exp\Big(-\frac{e(V(0)-V(x))}{KT}\Big) = n_0 \exp\Big(\frac{eV(x)}{KT}\Big) \tag{3.18}$$

since $V(0) = 0$.
To define the ion density, the quantity *g(x)* it is introduced, representing the rate of generation of ions per volume and time. Using this quantity it results that the ion density in a point x could be obtained by integration of the generation term of all the ions from the plasma center (x=0) up to that point, also accounting for the velocity the ions receive from the potential:

$$n_i = \int_0^x \frac{g(x_1)}{v(x_1,x)} dx_1. \tag{3.19}$$

Now, for the energy conservation, without collision, the velocity at which the ions move toward the electrodes it is obtained:

$$v(x,x_1) = \frac{2e}{M}\sqrt{V(x_1)-V(x)} \tag{3.20}$$

so the Poisson equation becomes:

$$\frac{d^2V(x)}{dx^2} = \frac{1}{\epsilon_0} n_0 \exp\Big(\frac{eV(x)}{KT}\Big) - \frac{e}{\epsilon_0}\sqrt{\frac{M}{2e}} \int_0^x \frac{g(x_1)dx_1}{\sqrt{V(x_1)-V(x)}} \tag{3.21}$$

now, using again the adimentional potential $\eta = -eV/KT$:

$$-\epsilon_0 \frac{KT}{e^2 n_0} \frac{d^2\eta}{dx^2} - e^{-\eta} + \frac{1}{n_0}\sqrt{\frac{M}{2KT}} \int_0^x \frac{g(x_1)dx_1}{\sqrt{\eta(x) - \eta(x_1)}} = 0. \tag{3.22}$$

On the left hand side it is easy to identify the Debye length ($\lambda_D = \sqrt{KT\epsilon_0/e^2 n_0}$). Using the adimentional length $\xi = x/L$, normalized to a length L to be defined later, the equation becomes:

$$\Big(\frac{\lambda_D}{L}\Big)^2 \frac{d^2\eta}{d\xi^2} + e^{-\eta(\xi)} - \frac{L}{n_0}\sqrt{\frac{M}{2KT}} \int_0^\xi \frac{g(\xi_1)d\xi_1}{\sqrt{\eta(\xi) - \eta(\xi_1)}} = 0 \tag{3.23}$$

which hold in the whole region between the electrodes, so that it can be called *complete plasma sheath equation*. The value of the generation term, g, can be inserted as:

$$g = \nu n_0 e^{-\gamma\eta} \tag{3.24}$$

where ν is a constant and γ is a parameter depending on the particular ionization process involved. Then, imposing $L = \frac{1}{\nu}\sqrt{\frac{2KT}{M}}$ yields:

$$\Big(\frac{\lambda_D}{L}\Big)^2 \Big(\frac{d\eta}{d\xi}\Big)^2 + e^{-\eta} - \int_0^\xi \frac{exp(-\gamma\eta_1)}{\sqrt{\eta(\xi) - \eta(\xi_1)}} d\xi_1 = 0 \tag{3.25}$$

For most laboratory plasmas $L >> \lambda_D$, thus, if the value of $d^2\eta/d\xi^2$ is small enough, we can neglect the first member of the previous equation, so that the expression becomes:

$$e^\eta - \int_0^\xi \frac{exp(-\gamma\eta_1)}{\sqrt{\eta - \eta_1}} d\xi_1 = 0 \tag{3.26}$$

Since neglecting $d^2\eta/d\xi^2$ is equivalent to have $n_e = n_i$, the neutrality condition, the last equation is defined *plasma equation*. Starting from 3.26 Harrison and Thompson [56] found solutions for ξ as a function of η. For the case of uniform ionization ($\gamma = 0$) the value was:

$$\xi = \frac{2}{\pi} e^{-\eta} \mathcal{D}(\sqrt{\eta}) = \frac{2}{\pi} \mathcal{F}(\sqrt{\eta}) \tag{3.27}$$

with

$$\mathcal{D}(x) = \int_0^x \exp(t^2)dt \qquad \text{and} \qquad \mathcal{F}(x) = exp(-x^2) \int_0^x \exp(t^2)dt.$$

This kind of solutions holds up to a limited value of ξ, that, for this case is $\xi_0 = 0.3444$, corresponding to a limited potential η_0, below which the equations are not valid, since the second derivative in equation in 3.25 cannot be neglected any longer. Hence, while inside the plasma we can obtain the potential behavior, there are some cases in which equation 3.23 is not easily solvable analytically, like in the case of the transition region between plasma and sheath (see also 3.1).
In this case the sheath approximation is used. The basic hypothesis is that in plasma used for the extraction of high current density beams, the plasma width is so large with respect to the sheath dimension that the fraction of current generated inside the sheath can be neglected. All the ions are so assumed to be created in a plasma whose potential solves the plasma equation 3.26. For this situation, it is more convenient to work on a first order differential equation equivalent to the plasma equation than on 3.26 directly. To obtain this equivalent equation we proceed by multiplying each member of 3.23 for η', the first order derivative of the normalized potential with respect to ξ. For the three items of the equation obtained the following relationships hold:

$$\eta'\eta'' = \frac{d}{d\xi}\Big(\frac{\eta'}{2}\Big)^2$$

$$e^{-\eta}\frac{d\eta}{d\xi} = -\frac{d}{d\xi}e^{-\eta}$$

$$\eta' \int_0^\xi \frac{g(\xi_1)d\xi_1}{2\sqrt{\eta(\xi)-\eta(\xi_1)}} = \frac{d}{d\xi}\Big[\int_0^\xi g(\xi_1)\sqrt{\eta(\xi)-\eta(\xi_1)}d\xi_1\Big] \tag{3.28}$$

so that we find the expression:

$$\frac{d}{d\xi}\Big[\Big(\frac{\lambda_D}{L}\Big)^2\frac{(\eta')^2}{2} - e^{-\eta} - \frac{L}{n_0}\sqrt{\frac{2M}{KT}}\int_0^\xi g(\xi_1)\sqrt{\eta(\xi)-\eta(\xi_1)}d\xi_1\Big] = 0. \tag{3.29}$$

demonstrating the constant value of the quantity in parenthesis. Now using the initial conditions and by substitution we find the differential equation equivalent to 3.23:

$$\frac{\eta'^2}{2}\Big(\frac{\lambda_D}{L}\Big)^2 + 1 - e^{-\eta} - \frac{L}{n_0}\sqrt{\frac{2M}{KT}}\int_0^\xi g(\xi_1)\sqrt{\eta(\xi)-\eta(\xi_1)}d\xi_1 = 0. \tag{3.30}$$

Now, let's consider the case of uniform ionization, with a constant value for g and $L = (n_0/g)\sqrt{2kT/M}$ in 3.30, obtaining:

$$\frac{\eta'}{2}\Big(\frac{\lambda_D}{L}\Big)^2 + 1 - e^{-\eta} - 2\int_0^\xi \sqrt{\eta(\xi)-\eta(\xi_1)}d\xi_1 = 0. \tag{3.31}$$

To use this equation inside the sheath we consider $\xi > \xi_0$ and integrate only up to ξ_0. Then, by differentiating the plasma equation 3.26 we obtain the relation:

$$\frac{d\xi_1}{d\eta_1} = \frac{1}{\pi}\Big[\frac{1}{\sqrt{\eta_1}} - 2F(\sqrt{\eta_1})\Big] \tag{3.32}$$

useful to rewrite the equation 3.31 by changing the variable as:

$$\frac{\eta'}{2}\Big(\frac{\lambda_D}{L}\Big)^2 + 1 - e^{-\eta} - \frac{2}{\pi}\int_0^{\eta_0}\sqrt{\eta-\eta_1}\Big[\frac{1}{\sqrt{\eta_1}} - 2F(\sqrt{\eta_1})\Big]d\eta_1 = 0. \tag{3.33}$$

If now also the spatial variable is changed from $\xi = x/L$ to $\zeta = (a-x)/\lambda_D$ to obtain a scale length that will be proportional to the Debye length, and measured from the sheath to the wall, an equation for the sheath region is finally found:

$$\Big(\frac{d\eta}{d\zeta}\Big)^2 = \frac{4}{\pi}\int_0^{\eta_0}\sqrt{\eta-\eta_1}\Big[\frac{1}{\sqrt{\eta_1}} - 2F(\sqrt{\eta_1})\Big]d\eta_1 - 2(1-e^{-\eta}). \tag{3.34}$$

3.3 Extraction and Acceleration Modeling

The previous sections gave an insight into the problem of the sheath formation in the presence of a transition between a plasma and a conducting wall. In the case of extraction of particles from the plasma, which is called plasma-beam transition, the basic physical mechanisms of sheath formation can be considered similar to previous case but some complications arise from the fact that here there is no static surface, but a free boundary facing an electric field. In this case plasma has to develop the sheath to preserve its neutrality against the penetration of this field. A balance will be established between the intensity of the field and the characteristics of the plasma, defining the shape of the plasma boundary at the interface plasma-beam. A figure of merit in this sense is the *meniscus*, that is the equipotential surface corresponding to the zero value of the electric potential, which has strong influence on the beam optics, representing the point at which the plasma particles start to feel the accelerating field and are extracted.
Further complications arise in the case of negative ion extraction, where the negative ion production mechanisms and their dynamics should be considered to account for the quantity of available extracted current density and the plasma boundary characteristics. This kind of modeling of the extraction region is usually made by means of hybrid PIC-Monte Carlo codes [57], [58],[59] which can accurately describe the atomic and molecular interaction of particles in the plasma and the sheath formation , but usually do not

give information on the beam optics after the extraction. Another class of codes couples the extraction and the acceleration problems, making simple assumptions on the extracted current of electrons and negative ions and on the meniscus shape to obtain information on the beam optics, using an iterative approach between the Poisson solver for the electric field and a ray tracing for the beam space charge deposition; within this category, where we can find both commercial codes and laboratory codes, I list : SCALA [60], KOBRA [61], SLACCAD[62] and OMNITRAK[63].

3.4 The Bypo Code

In the context of extraction modeling just described, the Bypo code [64] represent a considerable innovation, being capable of accurately describe the beam optics, with a self consistent calculation of the meniscus shape, obtained with the direct inclusion of some plasma physics features into the model rather then with simple assumptions on the extraction layer. The exhaustive description of this particular code will be the subject of the next section.
Even if real sources considered for fusion application are multi-beamlets systems, in which the final beam is obtained by the superposition of many small beamlets, extracted from the sources by means of gridded electrodes, in the Bypo model, as common in the standard extraction modeling, only the problem of the single beamlet extraction is treated, and the effects of interaction between different beamlets are partially considered with specific assumptions on the boundary of the domain. Further effects of mutual beamlet-beamlet interaction or grid offsets can be considered in the future. In picture 3.4 a schematic of a basic negative ion source for a single beamlet is shown, with a triode accelerating geometry. The particles involved are negative and positive ions and the electrons. In the description of the codes only the species lighter then H^- are considered, since the generalization to D^- is straightforward. The domain of the problem can be divided in 4 main regions:

1. The hot plasma region, where the plasma is unaffected by variations of the electrode potential and the electron temperature is high ($T_e \simeq$ 5-10 eV) and regulated by the ionization balance [65].

2. The Pre-sheath region, where only colder electrons may diffuse ($T_e \simeq$ 1-2 eV, thanks to the opposing effect of a filter field B_f and of collision. Here the plasma particle are thermalized to a reference temperature T and the quasi neutrality condition of the plasma still hold. It can be

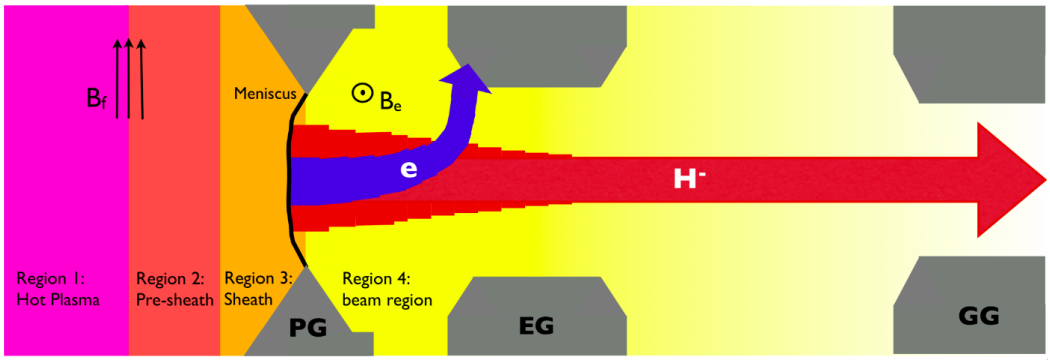

Figure 3.4: Schematic of a negative ion plasma source featuring a triode accelerating system. The division in sub-regions according to the plasma characteristics and the presence of the filter field B_f and the extraction field B_e are highlighted.

expressed in the form:

$$\frac{N_{H^+}}{N_{H^-} + N_{e^-}} \simeq 1 \tag{3.35}$$

with N_X being the density of the X species. In this region the potential is expected to have a plateau, a *crest*. Here the negative ions produced on the plasma grid surface (PG) are scattered and back-reflected toward the extraction apertures.

3. The Sheath region, whose width is extremely small, being proportional to the Debye length λ_D and a steep fall of the potential is expected. Here the meniscus is formed and the negative ions produced.

4. The beam region, dominated by the extraction electric field where the extracted particles are accelerated as a beam. A perpendicular extraction field B_e is included in this region, by means of permanent magnets embedded in the extraction grid (EG), with the scope of deflecting the electrons which are coextracted from the plasma before they gain the full acceleration. In the usual reference system the beam direction is z and B_e lies along the y direction. One of the main scopes of the model is to understand the effect of this y polarization of the B field, from which the name *Bypo* follows.

3.4.1 Basic Equations

Due to the big differences in the length scale involved in the problem, it is not convenient to consider all the regions in a single model. In Bypo the region 3 and 4 are completely included, and the domain starts on a so-called *startline*, placed some Debye length away from the PG surface. Some hypotheses are necessary to account for the plasma physics processes in the innermost region, in particular at the potential crest. Here a value of the potential $u(z = z_{cr}) = u_{cr}$ can be guessed, and an ion velocity given by

$$v_{cr}^{i} = \sqrt{\frac{T}{m_{H_-}}}\sqrt{t_{H^-}} = C_s\sqrt{t_{H^-}} \tag{3.36}$$

where C_s is the Bohm velocity required to access the sheath region, and $t_{H^-} = m_{H^-}v_{cr^2}/T$ represent twice the normalized kinetic energy of ions at the crest. The electron velocity will be, analogously:

$$v_{cr}^{e} = R_m C_s\sqrt{t_e} \tag{3.37}$$

with $R_m = \sqrt{m_H/m_e}$. As initial condition on the extracted current of ions and electrons the value: $J_{H_-}^0 \cong I_{H_-}/2r_h$ is used, where I_{H_-} is the extracted current density and r_h is the plasma grid aperture radius. The electron current density is expressed as $J_e^0 = R_j J_{H_-}^0$ where the quantity R_j represents the current density ratio between the two negatively charged species. The densities of the particles inside the code are normalized to the quantity N_0, defined as the numerical density of the negative species at the plasma crest.

$$N_0 = N_{H^-} + N_{e^-} = \frac{J_{H_-}^0}{eC_s t_H^{1/2}} - \frac{J_e^0}{R_m eC_s t_e^{1/2}} \tag{3.38}$$

obtained by exploiting the relationship $N_{cr} = J_0/V_z e$. So the relative densities are:

$$n_{H_-} = \frac{N_H}{N_0}; \qquad\qquad n_e = \frac{N_e}{N_0}$$

Concerning the positive ions, representing the confined species, their density is expressed by a maxwellian distribution:

$$n_{H_+} = K_0 \exp(u_{cr} - u) \tag{3.39}$$

with K_0 representing the normalized density at crest. Since in the plasma the quasi-neutrality condition must hold, meaning that $n_0 \simeq 0$, the value of K_0 should be close to 1. The adimensional quantities just defined will be

useful in expressing the Poisson equation in terms of relative quantities, but first the particle velocity will be obtained: using the energy conservation law between plasma region and electric field region:

$$\frac{m_e v_{cr}^2}{2} = \frac{m_e v^2}{2} - e\Phi \tag{3.40}$$

v can be obtained as:

$$|v| = \sqrt{v_{cr}^2 + \frac{2e\Phi(z)}{m_e}} \tag{3.41}$$

The velocity in a point is proportional to the starting velocity at crest v_{cr} plus the energy gain in the acceleration stage. Notice that the crest velocity is necessary, allowing particles to see the extraction potential. in our case electrons will experience a potential $\Phi = (\phi - \phi_{cr})$ It is convenient to define the adimentional potential:

$$u = -\frac{\phi e}{T} \tag{3.42}$$

where T is a reference energy unit (or a reference value for plasma temperature in energy unit), typically taken as T=1 eV. This value is constant and equal for all particle species considered, and it is used to rescale a lot of quantities in the code. By substituting back in 3.41 and remembering he definitions of C_s and R_m we find the velocity modulus:

$$|v| = \sqrt{v_{cr}^2 - \frac{2T(u - u_{cr})}{m_e}} = \sqrt{v_{cr}^2 - 2R_m^2 C_s^2 (u - u_{cr})} \tag{3.43}$$

Substituting now also the expression of v_{cr} taken from 3.37 the electron velocity is found:

$$|v| = \sqrt{t_e R_m^2 C_s^2 - 2R_m^2 C_s^2 (u - u_{cr})} = R_m C_s \sqrt{t_e - 2(u - u_{cr})} \tag{3.44}$$

and analogously the ion velocity:

$$|v| = C_s \sqrt{t_H + 2i_p(u - u_{cr})} \tag{3.45}$$

where i_p is a factor depending of the particle species, whose value is +1 for positive and -1 for negative ions.
Now starting from the canonical form of the Poisson equation:

$$\nabla^2 \phi = -\frac{\rho}{\epsilon_0} \tag{3.46}$$

ρ being the space charge density and considering two-dimensional case where z is the beam axis and x is the direction perpendicular to both beam axis

and magnetic field. Using the adimentional potential defined in 3.42, and the relation $\rho = e(n_H^+ - n_{H^-} - e)$, we gain

$$\frac{T}{e}\left(\frac{d^2u}{dx^2} + \frac{d^2u}{dz^2}\right) = \frac{\rho}{\epsilon_0} \tag{3.47}$$

and introducing also the adimentional densities defined in 3.4.1 the equation becames:

$$\lambda_d^2\left(\frac{d^2u}{dx^2} + \frac{d^2u}{dz^2}\right) = n_{H+} - n_{H_-} - n_e = n_a \tag{3.48}$$

where identified the quantity $\lambda_D = \sqrt{T\epsilon_0/N_0e^2}$, can be identified as the Debye length inside the plasma. Then, considering the relation $n_k = J_k/(eN_0v_k)$, being J_k , v_k the current density and velocity of the k species, we find

$$\lambda_D^2\frac{d^2u}{dz^2} = n_{H_+} - \frac{J_{H_-}}{eN_0v_{H_-}} - \frac{J_e}{eN_0v_e}$$

And finally, with the normalization of currents and densities, according to

$$\mathbf{j} = \frac{J}{i_p eN_0C_s} \qquad\qquad \mathbf{v} = \frac{v}{C_s} \tag{3.49}$$

and using the expression for ion and electron velocity obtained in 3.44 and 3.45 we get the Poisson equation in the explicit form solved by the numerical code:

$$\lambda_D^2\frac{d^2u}{dz^2} = n_{H_+} - \frac{\mathbf{j_{H_-}}}{\sqrt{t_H - 2(u-u_{cr})}} - \frac{\mathbf{j_e}}{R_m\sqrt{t_e - 2(u-u_{cr})}} \tag{3.50}$$

Notice that while potential, currents, velocities and densities are scaled, the lengths are not, since many length scales are present at the same time:

1. The radius of the extraction aperture
2. The Debye length
3. The Larmor radius for electrons
4. The Larmor radius for negative ions
5. The negative ion mean free path
6. The electron mean free path.

The procedure to obtain the motion equations for the particles, is to start from the Lorentz equation expression in case of z component:

$$\frac{dv_z}{dt} = \frac{i_p e}{m}(-\frac{\partial \phi}{\partial z} + v_x B) \tag{3.51}$$

Where was introduced the magnetic field $B = B_0 b$, necessary to deflect the coextracted electrons, and generated by permanent magnets embedded in the extraction grid [1]. With the normalized potential (3.42) and velocities (3.49), it is obtained:

$$\frac{1}{C_s}\frac{d\mathbf{v}_z}{dt} = \frac{d\mathbf{v}_z}{ds} = i_p(\frac{\partial u}{\partial z} + \frac{\mathbf{v}_x b}{L_i}) \tag{3.54}$$

Where L_i is the ion Larmor radius $L_i = C_s m/eB_0$ and s is an adimensional temporal coordinate defined as $ds = C_s dt$. In an analogous way we can find the motion equation along the x component:

$$\frac{d\mathbf{v}_x}{ds} = i_p(\frac{\partial u}{\partial x} + \frac{\mathbf{v}_z b}{L_i}) \tag{3.55}$$

and for the electrons:

$$\frac{1}{R_m}\frac{d\mathbf{v}_x}{ds} = -(\frac{\partial u}{\partial x} + \frac{\mathbf{v}_x b}{L_e}) \tag{3.56}$$

$$\frac{1}{R_m}\frac{d\mathbf{v}_z}{ds} = -(\frac{\partial u}{\partial z} + \frac{\mathbf{v}_z b}{L_e}) \tag{3.57}$$

where $L_e = C_s m/eB_0 R_m$. In order to find an equation for the particle densities, starting from motion, all solutions of the motion equation are collected by the functional ray map M, defined as:

$$x = M(z, x_s, \alpha_s) \tag{3.58}$$

[1]Notice that the only polarization of the field allowed is $\vec{B} = (0, B_y(z), 0)$. The field profile b is introduced in the code with analytical approximations; different models can be chosen, from a simple gaussian profile, up to an infinite array of permanent magnets in the upper and bottom part of the (z,x) plane, modeled with the expression:

$$B_y + iB_z = \frac{ik_7 B_r}{\pi}\Big[\arctan\frac{\sinh(\frac{a_z\pi}{L_y})}{\cosh\left(\frac{\pi}{L_y}(z - z_c + i(y-a))\right)}\Big]_{a=-a_y}^{a=+a_y} \tag{3.52}$$

for the dipole magnets, where B_r is the remanence of the permanent magnets, k_7 is a filling factor, and a_y and L_y define the position and dimension of the magnets.) and

$$B_y + iB_z = \frac{ik_7 B_r}{2\pi}\Big[\log\Big(1 + \sinh\big(\frac{a_z}{L_y}\big)\cosh\Big(\frac{\pi}{L_y}\big(z - z_m + i(y-z)\big)\Big)\Big)\Big]_{a=-a_y}^{a=+a_y} \tag{3.53}$$

for a quadrupole field.

depending on starting coordinate x_s and angle α_s with respect to the electric field of the x component of each ray. To fix ideas, let us consider electron and a fixed α_s value, so that $x = M(z, x_s)$. Since x_s may take continous values and an interval $(x_s, x_s + dx_s)$ of length dx_S of start positions, is mapped by 3.58, into an interval of length dx, using the electron conservation law gives

$$j_z^{st}(x_s)|dx_s| = j_z(x)|dx|. \tag{3.59}$$

By remembering that $j_z = v_z n_e$, substituting in previous equation, and solving for n_e yields:

$$n_e(z) = \frac{v_z^{st} n_e^{st} |dx_s|}{v_z(z, x_s)|dx|} \tag{3.60}$$

were the density of electrons trapped by the magnetic field is negligible for small values of B before the start line of the domain. Noting that $v_x = v_z dM/dz$ gives:

$$|v| = \sqrt{v_x^2 + v_z^2} = \sqrt{v_z^2 \Big[1 + \Big(\frac{dM}{dz}\Big)^2\Big]} \tag{3.61}$$

and

$$v_z = \frac{|v|}{\sqrt{\Big(1 + (\frac{dM}{dz})^2\Big)}} \tag{3.62}$$

The possibility that different rays can intersect each other, so that different starting conditions can belong to the same particular combinations of the points (z,x), bringing to multivalued functions should also be considered. To account for all of this we should sum over all starting positions:

$$n_e(z) = \sum_{x_s} \frac{j_z^{st}}{|v|} \frac{\sqrt{1 + (\frac{dM}{dz})^2}}{|\frac{dM}{dx_s}|} \tag{3.63}$$

Now we can express the particle density n_e as:

$$n_e = \frac{j_\Sigma}{\sqrt{t_e - 2(u - u_{cr})}} \tag{3.64}$$

in terms of the quantity

$$j_\Sigma = \sum_{x_s} \frac{j_z^{st} \sqrt{1 + (\frac{dM}{dz})^2}}{R_m |\frac{dM}{dx_s}|} \tag{3.65}$$

proportional to the absolute value of the current density; it can be shown that

$$j_\Sigma(z,x) = \int d^3v|v|\frac{f_e}{Rm} \tag{3.66}$$

f_e being the phase space density. The results still hold for ions , with the values $R_m = 1$ and with t_H^- instead of t_e.
Finally, if we define the quantity:

$$Q(z,x,w) = \frac{1}{R_m}\int dx_s\sqrt{1+(\frac{dM}{dx_s}^2)}j_z^{st}(x_s)\Theta(x-M(z,x_s),w) \tag{3.67}$$

where Θ is a smoothed Heaviside function, and w is the ray smoothing parameter, so that for $w \leq (x-M)$ the function becomes the normal Heaviside function. In physical terms, this quantity corresponds to the current passing below a particular point (z,x). Using the Dirac's delta properties [2] we can show that

$$j_\Sigma(z,x) = \frac{dQ(z,x,0)}{dx} \tag{3.69}$$

The derivative $dQ(z,x,w)/dx$ for $w > 0$ is a smooth approximation of $j_\Sigma(z,x)$, that is a smoothed current obtained by distributing the ray current into a strip:

$$M(z,xs) - w < x < M(z,xs) + w \tag{3.70}$$

this approximation is particularly useful in numerical computations when only a finite number of rays is available. Of course, summation on several α is understood.

3.4.2 Boundary conditions

Boundary conditions of the code are usual, with a particular condition on the start line. There, a mixed boundary condition is adopted, inferred from the mono-dimensional collisionless theory of positive ion extraction [66], [67] described in section 3.2 which gives a relation between the potential u and its derivative $\partial u/\partial x$. This kind of conditions makes the code intrinsically

[2] In particular it is exploited the relation:

$$\delta(f(x)) = \sum_i \frac{\delta(x-x_i)}{|f'(x_i)|} \tag{3.68}$$

where x_i are the zeros f(x). Note that the Dirac Delta is the derivative of the Heaviside function.

consistent with the ion source physics, and it represents a substitution of the pre-sheath region. This gives, in perspective, the possibility to use the code with different kinds of sources. To obtain this condition, starting from the equation:

$$(\lambda_D \frac{d\eta}{dz})^2 = -2(1+e^{-\eta}) + 4\int_0^\infty d\eta_1 \sqrt{(\eta-\eta_1)} G_0'(\eta_1) \tag{3.71}$$

that is equivalent to 3.34, with $G_0(\eta) = \pi^{-1/2} e^{-\eta} \mathrm{erfi}(\eta^{1/2})$ [3]. Since the case of negative ion extraction is being treated, the variable $\eta = -e(\phi - \phi_{cr})/T$ can be used.

The equation 3.71 expresses the behavior of the potential in the sheath region, starting from the position where the solution of the plasma equation has no meaning. The equation is implemented in the code in a smoothed version, obtained from [68] as:

$$S(\eta) = \begin{cases} a_1 \exp(a_2 \eta) & \eta \leq 1.25 \\ -2(1+e^{-\eta}) + 4G_0(\eta_0)\sqrt{\eta - a_3} & \eta > 1.25 \end{cases} \tag{3.73}$$

were the parameters values are $a_1 = 1.395 \times 10^{-4}$, $a_2 = 3.998$ and $a_3 = 0.146$. So, for the negative ion case, the boundary conditions at the start line ($z = z_{st}$) becomes:

$$-\sqrt{S(u_{cr}-u)} = \frac{\partial u}{\partial z} \tag{3.74}$$

in physical terms, the previous equation, together with the Poisson solver adjusts $u - u_c r$ at the start line to be of the order of η_0 in order to have a non zero $\partial u/\partial z$. In this sense it enforces an elaborate form of the Bohm criterion and also a small nonzero electric field for continuity with the pre-sheath [69]. As so far, u_{cr} and s_{st} were considered free parameters; in the framework of the analogy with the mono dimensional theory, equation 3.74 should hold also near the start line, so that is possible to calculate:

$$\frac{\partial}{\partial z}\Big(-\frac{\sqrt{S(u_{cr}-u)}}{\lambda_D}\Big) = \lambda_D \frac{\partial^2 u}{\partial z^2} \tag{3.75}$$

and substituting back in 3.50 to have n_{H_+}:

$$n_{H_+} = n_e + n_{H_-} + \lambda_D^2 \frac{\partial^2 u}{\partial y^2} - \frac{1}{2} S'(u_{cr} - u) \tag{3.76}$$

[3] erfi is the imaginary error function, defined as erfi(z)= -i erf(iz), and the following relation hold:

$$\mathrm{erf(z)} = \frac{1}{\sqrt{\pi}} \int_0^z e^{-t^2} dt \tag{3.72}$$

which, compared to the expression 3.39 gives:

$$K_{01} = \left(n_e + n_{H_-} + \lambda_D^2 \frac{\partial^2 u}{\partial y^2} - \frac{1}{2} S'(u_{cr} - u)\right) \exp\left(u_{cr} - u\right) \tag{3.77}$$

This value, generally different from the arbitrary chosen K_0, depend on z_{st}, x e K_0. By imposing K_0=K01 on the start line u_{cr} is determined. It means that a physical limitation exists on the crest potential crest in order to obtain a 1D sheath in the proximity of the start line.

3.4.3 Further development

The previous sections described the basic physics involved in the core of the model. There are other physical aspects whose influence on beam acceleration is usually considered to have less importance, but that can still affect the beam optics in several ways. Usually many codes for the beam optics neglect this effects, or account for their presence using successive approximations or data from other models. In Bypo some of these effects are included and their calculation is self-consistently added. Their implementation and other methods complementary to the code core are described in the following:

Electron stripping and pressure calculation

The negative ion beam, during its acceleration, as during all its propagation, is subject to interaction with the residual gas that from the source flows toward the end of the accelerator. The detailed consequences of this interactions will be the subject of the chapter 4, and here I only mention the most important, consisting in the detachment of the weakly bounded electron from the negative ion, resulting in a decrease of the beam density as the beams propagates. The calculation of the surviving beam transmission needs atomic cross section data, which are easily available thanks to the database introduced in section 2.3 and the residual gas pressure profile. Bypo calculates the pressure distribution inside the accelerator with a built-in partial differential equation model for the high vacuum gas pumping [70], as an alternative to the more exact but much more computationally expensive calculation of turbo-molecular flow with Monte Carlo methods or with direct view factors calculation [71].

Space Charge Compensation Model

The interaction of the beam with the gas, also creates secondary particles. Inside the accelerator these secondaries are subject to the electric field,

and rapidly accelerated, but at the accelerator exit, where the electric field is almost zero, the space charge of positively charged secondaries tend to accumulate and neutralize the negative ion beam space charge. Bypo accounts for this production of positive charges with two models: the first exploits the results of a mono dimensional model [72], and extrapolates them in 2D, while the second uses a simpler ad hoc Maxwellian for the positive ions. The models was compared with some Monte Carlo and fluid models [73] and the whole phenomenon will be described more in detail in section 4.1.2.

Extrusion to 3D domain

As already said, the original Bypo model [64] was not expanded in the cylindrical direction, since the magnetic field has a mono dimensional polarization. Anyway an approximated extension to cylindrical geometry of the results can be obtained considering only the multipole $m = 1$ in the 3D expansion of the potential u:

$$u(z, x, y) = u^0(z, r) + u^1(z, r) \cos\theta + ... \tag{3.78}$$

and it is implemented in the current version.

3.4.4 Numerical Implementation

The code was implemented in the Comsol Multiphysics environment, [74]. The geometry is fully parametric, allowing fast scanning of parameters of interest. It is convenient to describe the steps the code solves in terms of the vector solution $\mathbf{V}$, depending on the simulation parameters via the functional F, representing the code itself, as $\mathbf{V} = F(\mathbf{V_{in}}, j_\Sigma, d, I_N, C)$ where $\mathbf{V}$ includes u and u_{cr}. The non-linear solver uses the standard Newton-Raphson method [75], with a maximum number of iterations equal to I_N, a dumping factor between iterations d and an initial value $\mathbf{V_{in}}$. The variable C is the context, featuring the ensemble of equations used, including in particular the equations: (3.50),(3.77) e (3.64). Since it is known that for a stable solution the mesh should respect the law $\lambda/m_s \geq 2$, where m_s is the mesh size; the mesh is not homogenous in the domain but is very refined near the extraction ($\simeq \lambda_D/10$), and then gradually increases toward the acceleration region. The main steps solved by the code are summarized in figure 3.5. The parameters of the problem are fed to Bypo using an external input file, containing all the physical specifications. In a first step the code is initialized with the imported data, the geometry is created and the pressure profile calculated. For the first step solution an initial guess on the current density modulus j_Σ

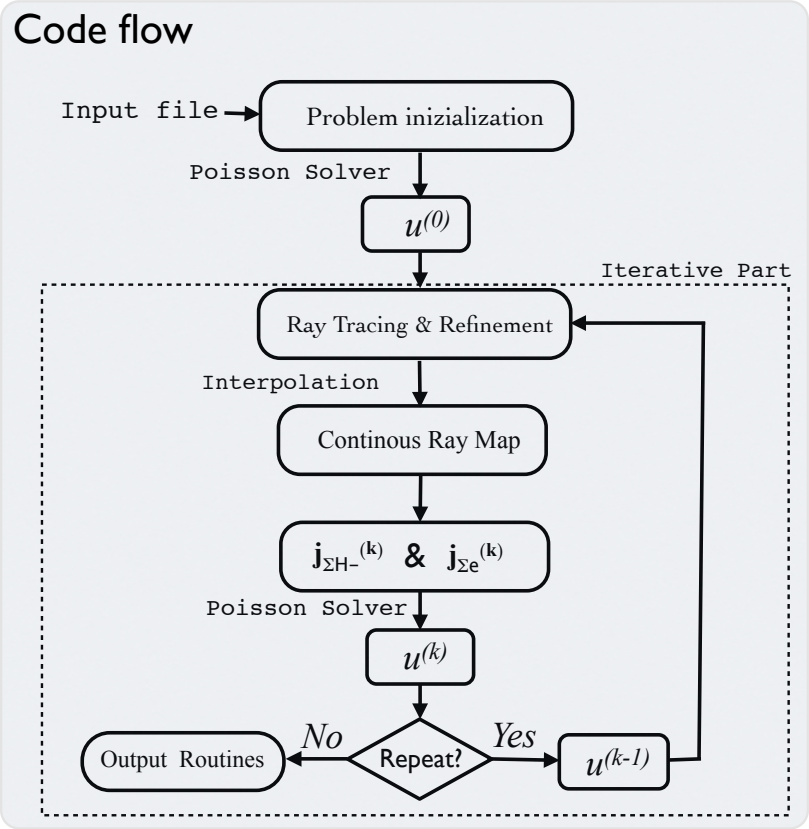

Figure 3.5: Summary of the steps executed by the Bypo code and its satellite routines.

is required, and for this scope a smoothed Heaviside function is used:

$$j_\Sigma(H^-) = j^0_{H^-}\theta(r_h - |x|, w_0(z)) \tag{3.79}$$

where $j^0_{H^-}$ is the nominal current density of the source, $r_h$the extraction hole and the smoothing factor $w_0 \approx 1/2m_s$ is proportional to the mesh size. This condition expresses the situations in which all extracted ions will travel parallel to each other; this is a good approximation of the real motion, and represents a better starting condition than the usual $j^0 = 0$ which simply gives the Laplace solution for u. For the initial value of the potential, necessary to avoid imaginary numbers in 3.64, the expression

$$u^{(00)} = u^{(00)}_{cr} - \eta_0 + (u_E - u^{(00)}_{cr} - \eta_0)\frac{(z - z_{st})^2}{(z_h - z_{st})} \tag{3.80}$$

is used. For the J_Σ calculation from the ray tracing, in order to simulate the effect of the plasma temperature on the particle motion at the emission, the ions and electrons are distributed in 3 groups , corresponding to different starting angles α_s (with respect to the electric field) and with different energies. Moreover the code performs a ray refinement near the beam edge, by increasing the number of rays in that region, to better investigate the beam envelope. This is achieved by interpolation and extrapolations of the initial rays. After the calculation of motion equation with a couple of Runge-Kutta integration, a continuos ray map $M(z, x_s, \alpha_s)$ is obtained by interpolation of initial rays. With the map the code can evaluate the integral 3.67 and obtain the value of j_Σ and thus the potential at the first step: u^0, by another calling to the Poisson solver. At this point the iterative process continues until the convergence, after a certain number k of iterations. Finally, to avoid oscillations of j_Σ between iterations another dumping is introduced: in terms of the solution vector previously defined:

$$u(k) = F(u^{(k-1)}, j_\Sigma^{(k)}, 1/2, 1, C). \tag{3.81}$$

Once the final convergence is reached, the result are stored and can be analyzed by a set of output routines, giving detailed information on beam emittance and divergence, beam transmission and optionally thermal loads on the structures (useful especially for the EG heating by coextracted electrons).

3.4.5 Some Results

Some general results of Bypo are reported here as samples of the potentiality of the code and of the kind of data it can provide. Further and more specific results will be discussed elsewhere in this work (see for example section 4.1.1). In this particular simulations Bypo implemented the geometry and characteristics of the SPIDER accelerator [76]. In figure 3.6 some sample trajectories from the ray tracing are visible; electrons are depicted in blu tones, negative ions in red tones. The ray refinement of ray tracing near the beam edge is highlighted, together with the different starting angles α_s of particles with respect to electric field, represented by different colors. Also notice the deflection of both species due to the extraction magnetic field, causing a small deflection of the primary beam, almost hitting the EG upper part, and a complete deflection of the electron beam. The periodicity on the upper and bottom boundaries is visible in the lengthening of electron trajectories between them. Figure 3.7 shows the surface plot of the quantity $n_a = n_+ - n_{H^-} - n_e$, the source term of the Poisson equation. Note the dishomogeneities of the negative ion beam, whose edges contain higher

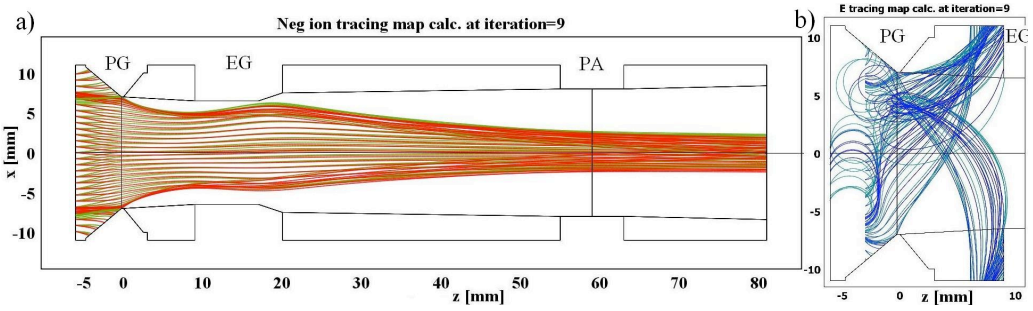

Figure 3.6: Some sample trajectories of the Bypo code. In a) the negative ions, in b) electrons. The different colors of the rays correspond to different groups of starting angles between the particle velocity and the electric field at extraction.

densities of H^-. Also in the extraction region the negative ion charge is very high ($n_a < -100$ are in white, for plot readability) due to contribution of both species and represent the strongest part of the sheath. Anyway the electron density is small, also near the upper dumping electrode,and the charge asymmetry in that region is small. Finally, in the drift region of the beam, downhill the grounded grid, the development of the space charge compensation of the beam is visible, as result of the simplified model included in Bypo mentioned in 3.4.3. Figure 3.8 show some equipotential lines with a contour plot of the potential u in the extraction region.

The value $u = 0$, in blue, represent the meniscus: the first equipotential surface that the plasma particles see before being extracted and accelerated. When the value of u_{cr} is within few volts from PG the plasma develops a flat plateau in the inner region finishing in a steep fall toward the meniscus, see b). The meniscus data from Bypo can also be exported to other codes. Thanks to the high degree of flexibility allowed in the geometry definition, Bypo is very suitable to perform scan test on geometry parameters. In the following simulations, for instance, the focus angle β, which is the angle between the PG electrode and the z axis was varie in a range of value of interest. As a consequence of this variation the final ray angles $\theta = \alpha_x(z_h)$ was studied, and their average value θ_{med} together with their standard deviation θ_{rms} are reported in the table 3.1 Since the H^- ray are converging in the chamfer region, the total extracted current I_{H^-} may be greater than the aperture $2r_h$ times the current density; the excess current F_E is defined by $1 + F_E = I_{H^-}/(2r_h j_{H^-})$. It is well known that to obtain a parallel beam, the optimal angle is $\beta = 67.5$ in planar geometry [77] and has an asymptotic value of $\beta = 74.160$ in cylindrical geometry. In our case, the ion beam has

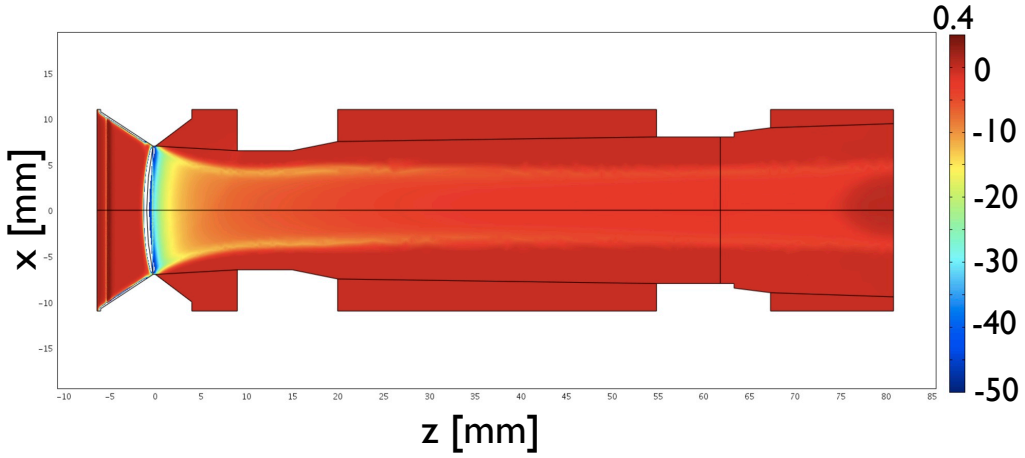

Figure 3.7: Surface plot of the total space charge of Bypo particles in terms of normalized densities defined in 3.4.1: $n_+ - n_e - n_{H^-}$.

to be convergent (say by an amount from 15^o to 25^o) at start since the EG aperture is smaller than the PG (in order to have space for placing magnets inside the EG); therefore a smaller optimal β (say by 15^o) can be expected. The results reported in the previous table for a planar geometry verify this rule. From θ_{med} and F_E it can be concluded that optimal focus angle is about $\beta = 55^o$ in planar geometry, as shown in 3.6. The ion deflection θ_{med} is proportional to the EG magnetic field, both as a direct effect of this field and as a reaction of the electrostatic field to off-axis beams. It can be corrected by magnets inside PA. Concerning the effect of varying the EG magnetic field, parametrized by the PM residual flux density B_R, there is not a significant range of choices allowed in this geometry. A 10 % increase from the fig 3.6 value, showing a limited ion clearance from EG, gives ion beam collision with EG. This is a bad failure, due to the probable cascade of secondaries. Conversely, A 25% decrease will spoil the confinement of primary electrons in the PG to EG gap; A result on the effect of magnetic field variation on the electron motion are reported in panel a) figure 3.9 to be compared with panels b) of figure 3.6 with the reference value field. A final example example of Bypo outputs is the possibility to have estimation on particle fluxes and heat loads. Maps of the normalized current density of primary particles j_z and j_x , in fact, can be obtained with some post-processing routines. Plots of j_z at particular z cuts are shown in figure 3.9. This kind of data are is still useful for a preliminary estimate of power load position, directly correlated to the EG magnetic field. Considering a cut at a negligible

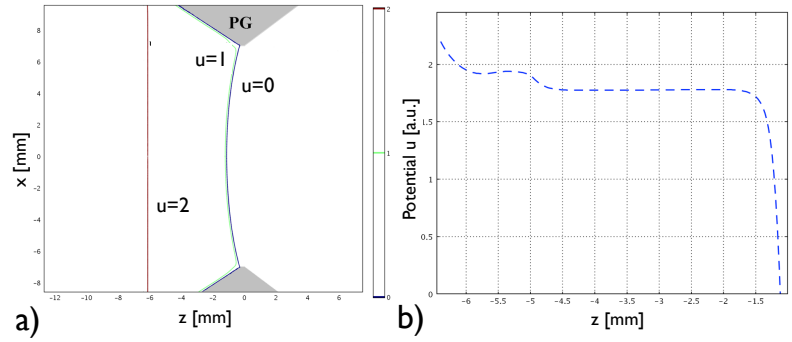

Figure 3.8: Bypo results for the meniscus calculation. In a) the meniscus shape is highlighted by plotting some equipotentials; in b) the potential behavior in the extraction region is showed.

β [°]	n_1	n_2	n_3	θ_{med} [mrad]	θstd [mrad]	F_E [%]
45	29	29	29	-8.3	20.6	1.9
50	30	30	30	-9.8	21.1	3.1
55	31	31	31	-9.8	21.0	3.2
60	24	27	27	-7.6	21.8	0.9
65	24	25	26	-8.0	22.9	1.2
70	26	26	26	-8.4	22.6	2.1
75	26	26	26	-0.9	22.5	2.1

Table 3.1: Results of a sensitivity analysis on EG focusing angle of the SPIDER accelerator performed with the Bypo code.

distance from the EG rear face, where most of the electron impinge, that is at $z = 9mm$: j_z contains only forward electrons, and thus j_z is the primary electron flow to wall. Moreover it is well known that power load to EG comes both from primary electrons and from the secondary particle generated [78]. For example a 10 keV electron impinging on EG wall, may produce, say, a 1 keV electron which is most probably pushed back to EG by the electric field: net effect is a small smoothing of power deposition. Another process is the generation of secondary electrons by beam collisions with background gas, which probably gives a diffuse load, so that peak position remains. More results about secondary production will be given in the next chapter. A rough estimation is still possible, remembering the equation of normalization of j_z, 3.49 we can obtain the real value of the current density, by multiplying

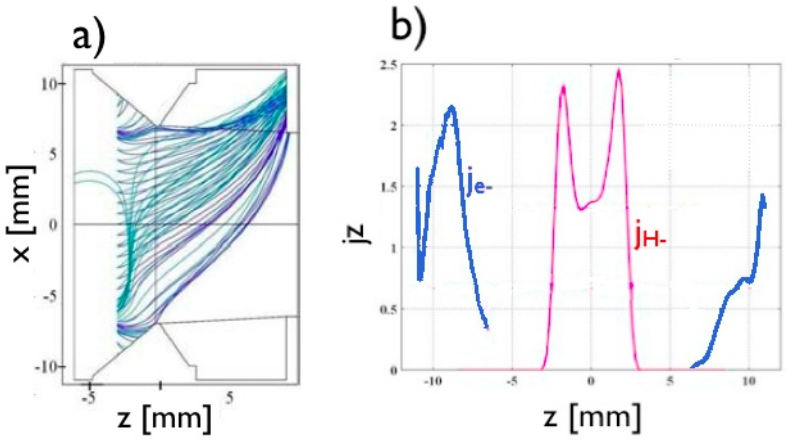

Figure 3.9: In a) Electron trajectories for the case of variation in the magnetic field leading to bad confinement ($B_R = 0.72$ T) in b) the normalized current density $j_z/(eC_sN_0)$ at different z planes: z = 81 mm (i.e. accelerator exit) for ions, in red, and $z = 9mm$ (i. e. EG front) for electrons, in blu.

for eC_sN_0, whose numerical value is 514 A/m^2. Now, being the extraction voltage V_{EG} = 9.8 kV a correspondent power load is found. for instance the peak infiugre 3.9, b) correspond to a power load deposition of about 11 MW/m^2.

Chapter 4

Beam Interaction with Gas and Surfaces

Once extracted from the source, the ion beam is subject to interactions with the residual gas flowing in the accelerator or with the electrodes or other surfaces of the device. The former produces of secondary particles by atomic reactions, causing heat loads on the structures and a reduction in beam propagation; the latter causes backscattering of particles and emission of electrons from the surfaces involved. As in the previous chapter, also in this section I will refer to the case of a hydrogen beam, since the extension to the deuterium case is straightforward.

4.1 Secondary production

In general all processes of beam interaction with the background gas can be expressed in terms of the impact of a H^- ion with a H_2 molecule. The most important ones are:

$$H^- + H_2 \rightarrow H + H_2 + e \qquad \textit{Single Stripping} \qquad (4.1)$$

$$H^- + H_2 \rightarrow H^+ + H_2 + 2e \qquad \textit{Double Stripping} \qquad (4.2)$$

$$H^- + H_2 \rightarrow H^- + H_2^+ + e \qquad \textit{Ionization} \qquad (4.3)$$

the relative importance of each reaction can be weighed on the product of the cross section σ with the H_2 gas density N_{H_2}, (both dependent on the axial coordinate z), and the single stripping reaction results to be the most effective for the secondary production. Further details on atomic and molecular processes, and their cross sections were given in section 2.3.
The study of trajectories of the newly created particles inside the accelerator is useful to estimate the heat load deposition and to account for their space

charge which, in some cases could even affect the potential distribution. To investigate these aspects of the beam gas interaction a particular model was developed as an add-on for the Bypo code described in section 3.4.

4.1.1 Collisions add-on for the Bypo Code

The interaction of the beam with the gas causes beam attenuation, depending on the z coordinate and the total cross section $\sigma_{tot} = \sum_i \sigma_i$, and the production of secondary electrons and positive ions. The first effect is already included in Bypo (see 3.4.3) as a correction to the total beam space charge, according to the expression:

$$F_s(z) = \exp\Big[-\int_0^z N_g \sigma_{tot}(z) dz\Big] \tag{4.4}$$

representing the surviving beam fraction, with N_g the gas density calculated by the internal pressure distribution routine
The secondary electrons and ions, affected by the electro-magnetic field, are quickly swept away from the negative ion beam, so that their contribution to the space charge is expected to be small. On the other hand they represent the main contribution to the heat load on the device structures. The model I am going to describe, developed as an add-on for the Bypo code, is intended to investigate the effect of secondary production both in terms of contribution to the potential distribution, and heat loads.

Model Description and implementation

The electric and magnetic field are provided, together with the main parameters of the simulation by Bypo itself. The add-on acts inside the main program flow at the end of each iteration, by evaluating the position at which the interactions take place, creating and moving the relative secondaries and correcting the space charge density map of Bypo before the next iteration. The position of interaction and which kind of interaction could occur are chosen by a Monte Carlo approach; first the trajectory of each primary particle is divided in a certain number of intervals Δz: the probability P that a reaction occur in an interval is:

$$P = 1 - \exp[-N_g(z)\sigma_{tot}(E_b)\Delta z] \tag{4.5}$$

for each interval a random number R_1 is generated by the pseudo random number algorithm (inbuilt in MATLAB) with uniform distribution between 0 and1. If $R_1 \leq P$ a reaction occurred in the Δz interval.

The kind of reaction is defined using another random number R_2 uniformly distributed between 0 and 1 so that the relative probability of the i-th reaction is σ_i/σ_{tot}
The primary rays, are injected in the domain with 3 different angles with respect to the electric field, as in Bypo, and each of them represents a number n_p of macro-particles, so that the current density assigned to the created secondary is a fraction $1/n_p$ of the current carried by the primary ray involved, and their density n_s, obtained by the simple formula $n_s = j_s/v_s$, is recorded on a density matrix. This process is the most time consuming, since for a good statistical average a number $N > 10^5$ of particles is needed. The standard output are 4 density maps, one for each kind of secondaries produced: electrons, H^+, H^0 and H_2^+.
Note that the secondary velocity v_s depends on the starting velocity of the particles, plus the velocity gained from the electromagnetic field once accelerated. The starting velocity is very different from a reaction to another: in case of stripping reactions, the secondary electrons and H^0 (or H^+), being fragment of the primary H^-, preserve all the primary velocity, depending on the beam energy E_b. Conversely, in case of ionization, the electron and the H_2^+ ions come from the background gas, that, being neutral, is not affected by the fields of accelerator and has only a small kinetic energy whose value was estimated to be $E_{H_2} \simeq 0.18\text{eV} \simeq 2000$ K, as measure for the beam temperature in the RF source BATMAN at IPP [8]. This aspect will have great importance in increasing the positive charge density, as highlighted in the next sections. To preserve this difference in starting velocity of particles a further subdivision can be optionally imposed in the code, with the production of further density maps, also dividing the secondaries according to their initial conditions.

Results

Bypo and its secondary add-on were tested for the case of the SPIDER accelerator [79],[76], and a benchmark with a similar code was obtained [78]. Here I will focus on the result about secondary beams only, produced by the Bypo add-on, in terms of space charge density and power deposition.
Figure 4.1 shows the secondaries density maps. in a) the electron distribution shows an accumulation point near the extraction grid, were most of the electrons are deflected by the electromagnetic field. Here the electrostatic potential had not sufficient time to give the particles high acceleration, and their density is consequently higher. Nonetheless, as expected, the final amount of electrons is small with respect to the beam density, and the correction to potential distribution can be neglected. In the second part of the accelerator the

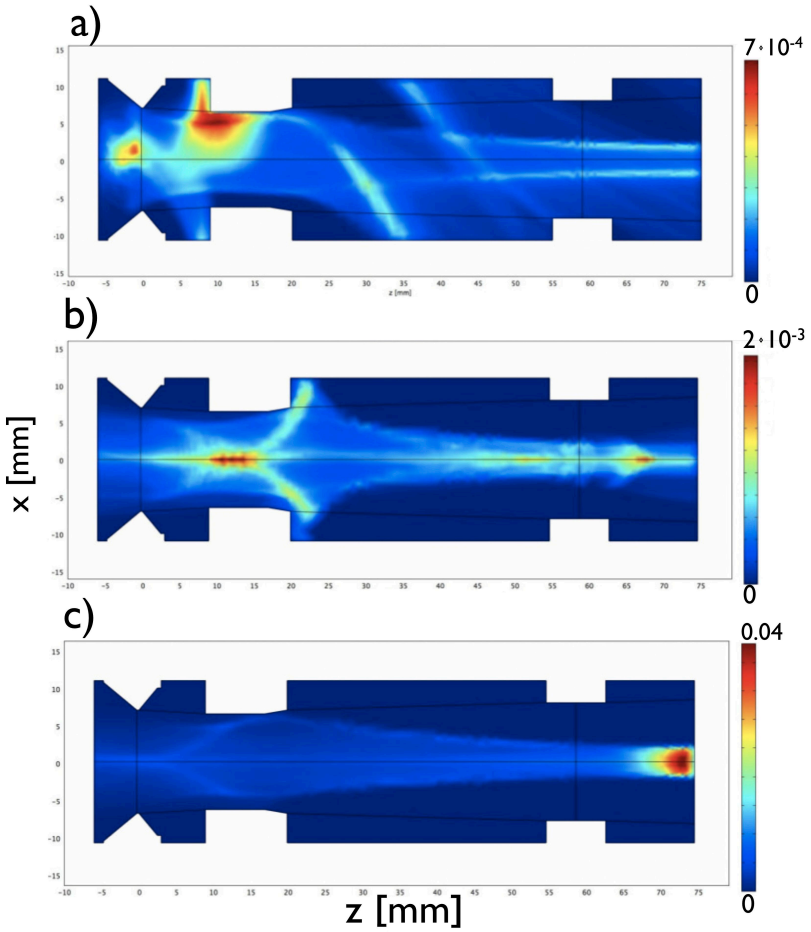

Figure 4.1: Surface plot of the normalized densities of secondaries for electrons (a), positive ions H^+(b) and H_2^+ (c).

electrons are subject to strong potential and quickly accelerated, so that their density is even lower. Also note the periodicity imposed to the trajectories in the upper and bottom boundaries. Figure 4.1 b) shows the H^+ distribution. Here the density maxima correspond to the points were the ions revers their motion. We should remember, in fact, that when H^+ ions are produced, they still keep the parent H^- velocity, thus, before being back-accelerated by the electric field they have to zero their z-velocity and reverse the motion; as the velocity decreases an increase in density is recorded, but also in this case it is ineffective in modify the potential distribution. Finally, in c) , the H_2^+ contribution shows a strong accumulation point in the grounded grid region, were the positive charge begins to be so high to compensate the space charge

density of the beam. This is due to the small starting velocity of the ions in a region were the electric field is almost constant. As evident form the trajectory analysis, the particles perform multiple oscillations in the beam potential well before reaching the region where the electric field is effective and the back accelerations begins, having sufficient time to accumulate a strong positive space charge. This results reflect the phenomenon of space charge neutralization which will be treated in the next section. In figure 4.2

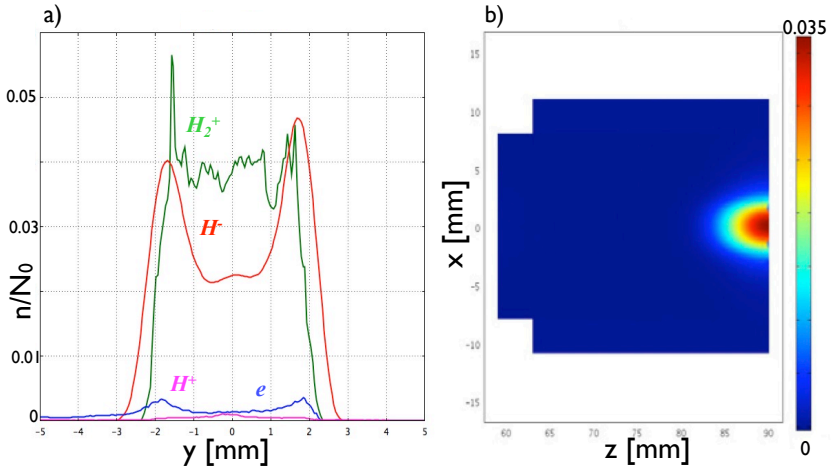

Figure 4.2: Secondary space charge at accelerator exit. In a) the secondary densities are compared with beam density value. In b) the result of the Bypo model for the SCC are reported, for comparison.

b) the outputs of this calculation are summarized in the plot of the normalized densities of all secondaries at the end of the accelerator, with respect to the beam density: the importance of the H_2^+ contribution is evident, while the density of other secondaries can be neglected in the potential calculation. These results on the H_2^+ density were compared with the analytical model of the space charge compensation included in Bypo (see section 3.4.3), finding a reasonable agreement for the small value of beam overcompensation. For this reason the analytical model, faster to converge, and giving smoother density map, was preferred to the Monte Carlo model for the space charge computation of Bypo between iterations. Some differences are anyway present for the position at which the beam starts to be fully space charge compensated, justifying the further investigations on the phenomena reported in section 4.1.2.
While the contribution of secondaries in terms of density is small, the beams

they form could be source of considerable stresses for the structures of the device. The power load deposition by primary particle is already included in Bypo, while the secondaries can be evaluated by the add-on just described. The multi-physic environment of Comsol [74] in which Bypo was written, allow us to couple the power deposition problem with a thermal analysis problem, to estimate the temperature rise in the grid of the accelerator as a consequence of the power deposition [80]. A first analysis was performed considering the power deposition on the extraction grid, where a large amount of heat loads is foreseen, and using the 2D geometry with the Comsol stationary heat transfer module. The equation solved in this case was the classic heat transfer relation in the absence of source term:

$$-\nabla \cdot (k\nabla T) = 0 \tag{4.6}$$

With k representing the material conductivity and T the temperature. In our case the grids are made of copper (conductivity 400 W/m K), the cooling pipe inside it is simulated with a Dirichelet boundary condition corresponding to a fixed temperature (75 °C , estimated by previous analyses and empirical considerations) and the heat load on the external surfaces is considered with a Neumann boundary condition, expressed as:

$$n \cdot (k\nabla T) = P_0 \tag{4.7}$$

n being the surface normal and P_0 the power load deposition coming form the impinging particles. For the case here reported the average power density value is about 4 MW/m^2 for the grid front, causing a temperature rise limited to 10 K, and a clear peak is found in the lower part of the extraction hole, as shown in fig 4.3 Since for an accurate heat load estimation a 3D simulation is required the 2D (xz) power density profile of Bypo was extrapolated in the y direction according to the formula:

$$P_b(x,y) = \frac{1}{2}\Big(1 + cos\theta\Big)P_b(r) + \frac{1}{2}\Big(1 - cos\theta\Big)P_b(-r) \tag{4.8}$$

with r and θ the polar coordinates. This heat load P_b ant the consequent temperature increase in the EG are shown in fig 4.4 The total power load obtained from the Bypo profile from 2D boundary integration and multiplying for cell height, is 435 W due to primary electrons and 8.6 W due to secondary electrons. This data were also benchmarked with the result of EAMCC [78], a similar code whose peculiarities will be described elsewhere in this work, and the results were found in good agreement [80].

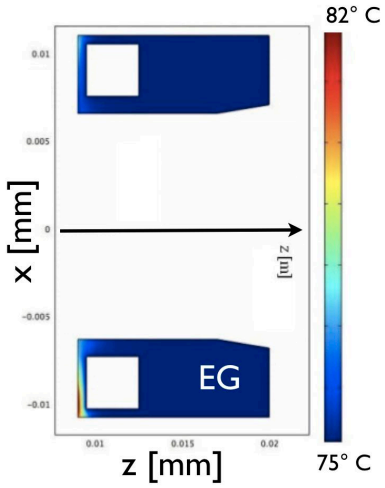

Figure 4.3: Temperature rise in Spider EG, including the cooling channels.

4.1.2 The Space Charge Compensation

The space charge compensation (SCC) is a typical phenomenon in accelerator physics, consisting in the accumulation inside the beam of secondary particles having charge of the opposite sign with respect to the beam particles, evolving in the formation of a plasma. This charge is produced as the beam traverses the drift region, where the electric field of the electrodes is negligible, by beam-gas interactions; in the absence of acceleration due to external fields such particles remain trapped inside the beam potential. For the case of positive ion beams the electrons represent the neutralizing species, and their source is mainly the atomic reaction of ionization:

$$X^+ + X_2 \rightarrow X^+ + X_2^+ + e \tag{4.9}$$

X^+ being the beam particle and X_2 the gas target. In this case the electrons stay trapped in the positive potential well created by the beam itself, while the X_2^+ is quickly expelled. At a certain point an equilibrium is reached in which the beam potential is shielded by the secondary charge. This phenomenon greatly helps beam propagation, avoiding the beam spread under the effect of its own space charge, and in some cases electrons are intentionally added to the beam to help its neutralization. From the analytical point of view the process involves four equations: the continuity equation for ions and electrons:

$$\frac{\partial n_i}{\partial t} = n_g n_b \sigma_i v_b \tag{4.10}$$

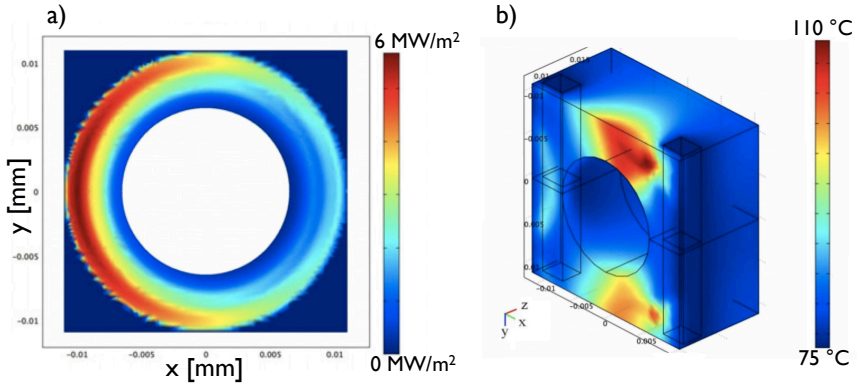

Figure 4.4: Power density profile on EG front (a) and the relative temperature rise(b).

with n_b and n_g beam and gas density respectively, σ_i the ionization cross section and v_b the beam particle velocity, an equation for the energy balance of plasma, yielding the electron temperature, and the Poisson's equation for the radial electric field. This system, involving highly non linear integral differential equations, was challenged by several authors [81],[82],[83]. For the space charge neutralizations of negative ions two process are involved: the basic ionization reaction, like for the positive beam case:

$$X^- + X_2 \rightarrow X^- + X_2^+ + e \tag{4.11}$$

and the complementary equation in which the beam particle is also subject to stripping, creating fast electrons; anyway, since the secondary heavy particles and electrons are created retaining the high parent velocity, their contribution to the space charge is small and can be neglected. Notice that the basic difference with the positive beam compensation case consist in the fact that the neutralizing species, H_2^+ for the case of an hydrogen beam, is a heavy particle. The reference theory for negative ion beam compensation is due to A. Holmes [84], also developed by E. Surrey for the specific case on negative ion based neutral beam injector [72]. In this case overcompensation of the beam could occur, causing a focusing effect on the beam and , in the worst case, beam stall.

Numerical Methods

Many studies on space charge compensation can be found in literature, where the problem was usually adressed by means of 1D radial transport

codes [85] or Monte Carlo codes [86],[87]. In this section a PIC-Monte Carlo code is presented, developed in MATLAB - COMSOL environment [27],[74] to investigate the space charge neutralization for a negative ion beam in a 2D domain on the zx plane, z being the beam axis. With respect to the classical 2D xy transversal simulations (see, for instance [88]), the particular geometry chosen allows to investigate the beam parallel dynamics of the phenomenon.
The simulation is performed by starting from an assigned space charge distribution n^0_{tot} corresponding, at the beginning, to the beam density alone ($n^0_{tot} = n_b$, n_b being the beam density) and the electric field is computed by the Comsol Multiphysics solver for Poisson equation, according to

$$\epsilon_0\Big(\frac{d^2u}{dx^2} + \frac{d^2u}{dz^2}\Big) = qn^0_{tot} \tag{4.12}$$

Then new particles are generated continuously according to 4.11; newly created secondary particles (and the old ones if any) are advanced with a leap-frog method implemented in an external routine in MATLAB, for a given number N_s of time steps dt (typically 1). After this, the total space charge is updated, by modifying the density source term in the potential solver as $n_{tot} = -n_b - n_e + n_2$, where n_2 is used to denote the H_2^+ density. Then the Poisson equation is solved again, and time evolution is resumed.
Also the H^- beam trajectories, even if they constitute a quasi fixed background, can be updated, and a longer period dt_2 is chosen for them, distributing the stationary ray along the whole domain, and assigning their charge to the nodes of the density matrix. Differently from the case of secondaries the primary particles are moved as a continuous ray with the internal Comsol Multiphysics routine, involving a couple of Runge-Kutta methods of orders four and five. Secondary particles are created according to the equation:

$$R_s = \frac{dN_2}{dt} = N_g v_b n_b \sigma_1 \tag{4.13}$$

were N_g is the gas density, σ_1 the cross section of the process[1], v_b and n_b the beam velocity and density respectively. An effective density of secondary particles $n_s = R_s dt$ is created at each time step, and divided into suitable number of macro-particles, having a specific weight $W = n_s/N_p$, with N_p being the number of macro-particles injected in the domain at each time step, whose positions are chosen randomly inside the beam region with a velocity

[1]The cross section for the ionization of background gas by H^- projectile, according to 4.11 is unavailable in literature, and the cross section of 4.9 was used instead, as usual in negative ion based NBI modeling [78].

depending on particle species. Since the number of secondaries is increasing at each time step, especially during the transient phase of the SCC when the particle losses are small, a limit N_{max} on the number of particle can be imposed in the code, so that when N_{max} is exceeded the specific weight of each particle is increased and their number decreased by some percent. Due to the nature of this approach, compared with the huge spatial dimension of the problem, the code tends to yield a noisy signal for the secondary density. For this reason the final density map used to feed the potential solver was smoothed, using the implementation of a 2D convolution product between our density with a *window* function[2]. Regarding the boundary condition, a potential value $u = 0$ is imposed at the lateral boundary corresponding to the GG exit position and on the opposite boundary, corresponding to the calorimeter position or any other grounded part where the beam arrives. The distance between the GG and this grounded part will define the domain dimension along z, L_z. For the upper and bottom boundaries, a situation in which the beamlet is surrounded by walls situated at a distance $w = R_t - 0.5L_x$ from our boundary is simulated, L_x being the domain vertical dimension; by a series expansion in w, the potential u at the wall is approximated with $u + w\mathbf{n} \cdot \nabla u$ at boundary, with $\mathbf{n}$ the outward normal, and this value is set to zero. Introducing $i_w = 1/w$ we can write our boundary condition in a generalized Neumann form, as:

$$\mathbf{n} \cdot \nabla u = -i_w u \qquad \text{at} \quad x = L_x/2 \tag{4.15}$$

Such model is flexible and can be adopted to different cases and beam characteristics. In the following discussion we will refer to the results obtained for a SPIDER like beam. In the following table, the main input parameters needed by the model are reported, with the relative notation; SPIDER [76] parameters are summarized in table 4.1:

Where the beam value of current of SPIDER was obtained by considering a 20% stripping on the nominal extracted value of current density ($340[A/m^2]$) and dividing by the number of beamlets of SPIDER (1280) to have the single beamlet value. The electron temperature refers to the slow electron created in the ionization of background gas, as in 4.11. The corresponding 10 eV were used to account for a minimum energy transfer from the projectile H^- during the reaction. Conversely the H_2^+ velocity comes from

[2]the convolution W between two matrix A and B is defined as

$$W(t) = \int A(s)B(t-s)ds \tag{4.14}$$

in this case A will be our density matrix and B the window function, usually a Gaussian. The dimension of the window matrix will define the smoothing factor.

SCC simulation input data			
Beam Energy	E_b	100	[keV]
Beam Voltage	V_B	100	[V]
Beam current	I_b	$\simeq 0.04$	[A]
Beam Radius	r_b	$4 \cdot 10^{-3}$	[m]
H_2 Gas Temperature	T_{gas}	0.18	[eV]
Slow e^- temperature	T_e	10	[eV]
Residual gas density	N_g	$2 \cdot 10^{-18}$	$[m^{-3}]$
Domain length along z	L_x	0.5	[m]
Domain length along x	L_x	$2.2 \cdot 10^{-2}$	[m]

Table 4.1: Summary of data used in numerical simulations.

Derived quantities			
Beam velocity	$v_b = (2qE_b/m_{H^-})^{1/2}$	$\simeq 5 \cdot 10^6$	[m/s]
Beam density	$n_b = I_b/(qv_b\pi r_b^2)$	$\simeq 1 \cdot 10^{15}$	$[m^{-3}]$
H_2^+ thermal velocity	$v_2 = (2T_g/m_{H_2^+})^{1/2}$	$\simeq 1 \cdot 10^3$	[m/s]
Slow e^- thermal velocity	$v_e = (2T_e/m_e)^{1/2}$	$\simeq 2 \cdot 10^6$	[m/s]
Debye length	$\lambda_D = (\epsilon_0 T_e/(qn_b))^{1/2}$	$\simeq 7 \cdot 10^{-4}$	[m]

Table 4.2: SCC simulation data.

the gas temperature, estimated from IPP measures [8], since the heavy core of the molecule is expected not to be perturbed by the ionization reaction. Starting from this data, the other simulation parameters can be derived from the basic equation contained in table 4.2 together with the corresponding values in the case of SPIDER With q representing the electron charge and ϵ_0 the vacuum permeability. To follow the dynamics of the whole system the characteristic time step dt of the simulation should be chosen. So, according to electron velocity and Debye length of the plasma the value of the time step could be chosen according to $dt = \lambda_D/v_e \simeq 1.7 \cdot 10^{-10}$ s. Anyway, since both the cell size and the time steps depends on the beam density, a scaling of this quantity to a lower value was use in the analysis here reported. This correction still preserves all the physical information of the phenomenon and was found useful to speed up the simulation. The beam density was thus decreased to $n_b = 10^{13} m^{-3}$, and all the quantities are rescaled consequently. This gives a value of the time step $dt = 10^{-9}$ s used in the following simulations.

Results

In a first series of simulation, secondary charge was zero at start, that is $n_a^0 = n_b$, in order to investigate in detail the transient phase of the space charge neutralization; this gives a huge negative potential well, so that the beam opens up at the beginning until SCC is enough to significantly reduce this potential well; after that the beam can propagate with lower perturbation. A typical snapshot of the situation, for different time steps is reported in figure 4.5. In the first plot, corresponding to the beginning of the simulation, after a time $t = 0.06\ \mu s$, the secondary H_2^+, in green in the first graph, are well confined in the radial direction, due to their isotropic generation along the beam and their low velocity. Electrons, in blue in the same plot, have a greater mobility and are quickly expelled from the domain. The behavior of the potential in the axial and radial direction is reported in the other two plots on the left. Notice the high depth of the potential well ($\propto 8000V$) self induced by the beam, which is consequently defocused. On the right hand side the radial distributions of density of all particles are reported, together with the total density. This densities in the radial direction are obtained by performing an average over several densities at different axial positions along z. Also notice the smoothing performed on the total density, to feed the potential solver with a more stable density. After 5.5 μs the H_2^+ had enough time to move in the domain, and tend to sit where the potential is more negative, in the position around $z = L_z/2$ causing the depth of the potential well to reduce to roughly 1/8 of the initial value. Notice that also electrons tend to concentrate in the same position, due to the flattening of the potential in that region, corresponding to an almost zero electric field. Their contribution to space charge is however small, as is clear form the density plot on the right. Conversely the H_2^+ density is already almost compensating the beam density. For $t = 8.5\ \mu s$ the SCC is completed: the potential is close to zero, and the density of positive ions and beam particles compensate each other. From this time onward the potential starts to have some oscillations between the accumulation of the positive space charge and their expulsion, as the potential starts to be positive. This first set of analyses also highlighted the possibility of beam reflection in the case of dense beam: considering higher beam density, for instance $N_b = 5 \cdot 10^{15}\ m^{-3}$, it will bring to an extremely deep negative potential well at the zero time step of our simulation, as it can be estimated also by a rough 1D estimation of the Poisson equation, considering

$$\frac{du}{dz} = -\frac{q \cdot N_b}{\epsilon_0} \tag{4.16}$$

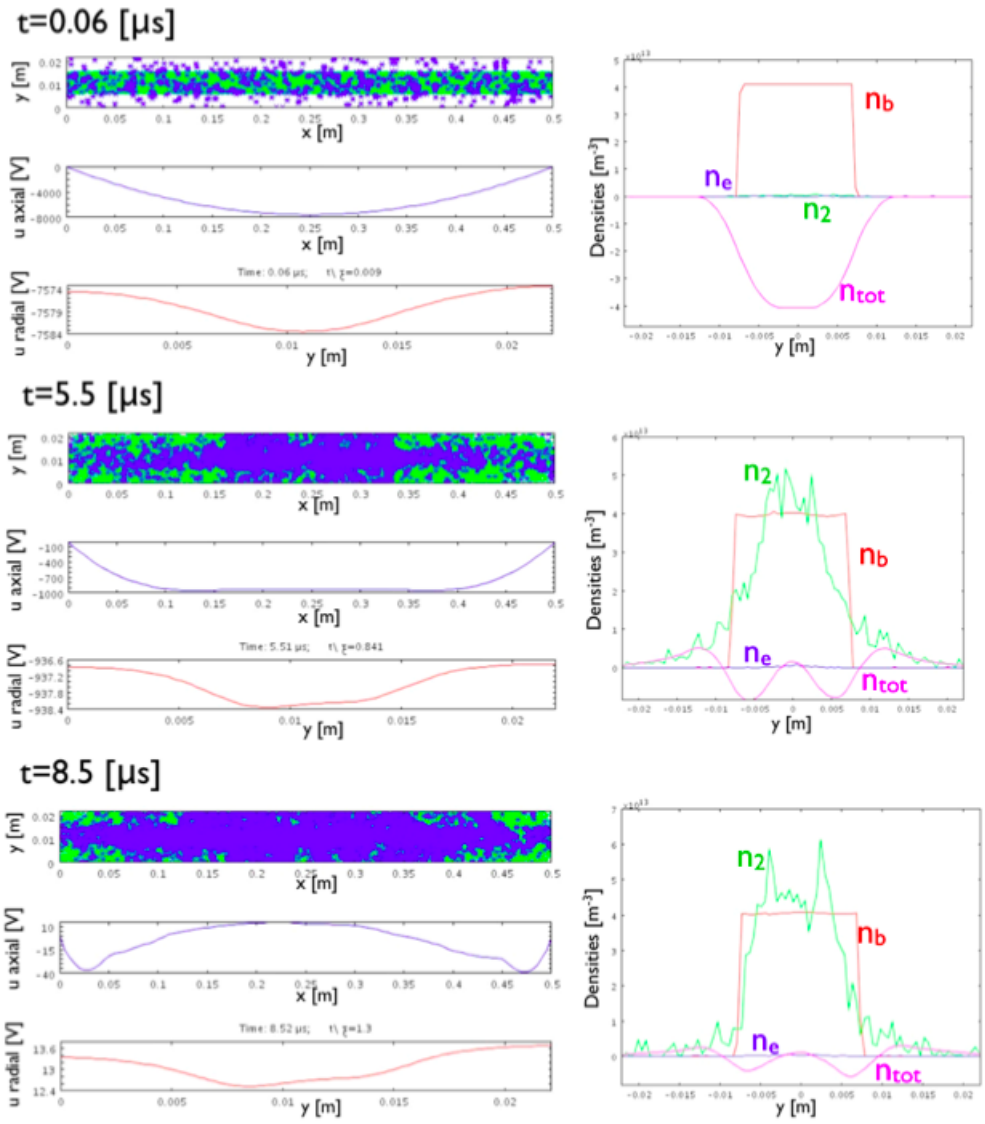

Figure 4.5: Temporal evolution of the SCC. Some graphics containing data from 3 different times are reported, each of them containing 4 different plot of the plasma characteristics. In the firs the secondary H_2^+ (green) and electron (blue) position are reported; in the second and third the axial and radial behavior of the self induced potential u; in the fourth, on the right, the radial distribution of particle density are reported.

solving the equation for the potential u, with the boudary conditions $u(z = 0) = u(z = L_z) = 0$ and calculating the potential in the position $x = L_z/2$,

where the minimum is expected, yields:

$$u(z = \tfrac{1}{2}L_z) = \frac{N_b \cdot g_0 \cdot q \cdot L_z}{8\epsilon_0} \simeq 10^5 V \tag{4.17}$$

where we use the factor g_0 containing the geometric ratio between the domain and the beam dimension to account for the localized space charge deposition of the beam with respect to the whole 2D space. Notice that the potential well depth is comparable or even higher than the beam energy, causing beam reflection, as reported in figure 4.6

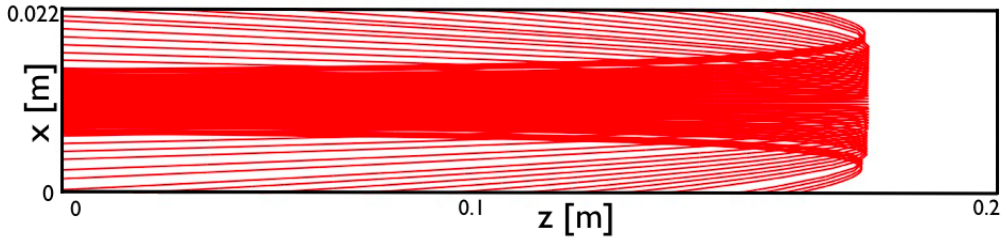

Figure 4.6: Sample trajectory plot of a primary negative ion beam drifting with a density $n_b \propto 10^{15}$ $[m^{-3}]$. The highly negative space charge induce a total reflection of the beam.

To stay well below this situation, a scaling of n_b to a lower value was used also for our case.

Due to the many time scales involved, some time oscillation may appear (and maybe damp): generally, ion losses oscillate between axial and radial directions; electron losses roughly have the opposite phase. The potential is expected to have a maximum depth at the central point $z = L_z/2$ and $x = 0$; let ϕ_R be the ratio of this potential depth and its value at $t = 0$. Figure 4.7 shows time evolution of ϕ_R and of the normalized particle densities. This depth is drastically reduced by the accumulation of H_2^+ ions, and the neutralization is reached in a time $\tau_n \simeq 8 \cdot 10^{-9}$ s, close to the theoretical SCC time defined as $\tau_{th} = 1/(\sigma \cdot N_g \cdot v_b) = 6.3 \cdot 10^{-9}$ s. Electrons apparently do not play a role in the transient phase of compensation, since they are rapidly expelled from the beam. This aspects are more clear in figure 4.8, reporting the fluxes of electrons and H_2^+ expelled form the beam in time for a similar situation. In the first inset the evolution of the minimum of the potential is plotted with respect to the time step of the simulation. the second inset report the behavior of the electrons expelled form the domain. It result that most electrons are expelled axially, during the developing of the space charge, depending on the high negative potential of the beam. As soon as the beam

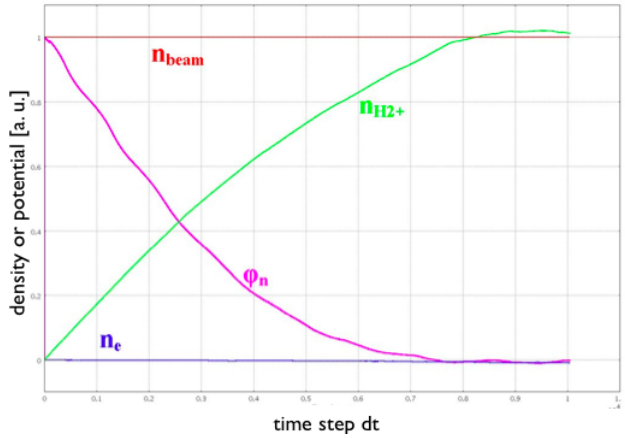

Figure 4.7: Time evolution of the SCC phenomenon. The depth ϕ_n of the potential well induced by the beam is reported, together with the densities of the primary beam and secondary particles.

potential starts to be neutralized the axial losses become lower, until they reach contained up to reach the level of the radial losses, whose behavior is almost constant during the transient phase. When the potential starts to be almost constant the radial losses start to oscillate, following the potential evolution. this aspect will be treated later. For the positive ions the situation is reversed: the axial losses are almost zero, since the particles are trapped inside the beam and starts to increase as the electric field goes to zero. The radial behavior of ions is almost constant, only showing a small increase after $\simeq 5000$ time steps. This can be interpreted with the idea that for small enough values of the axial electric field, the velocity acquired by ions in the axial direction helps the ions in to leaving the domain in the radial direction, due to the large dimension ratio ($L_z/L_x \simeq 23$). To better investigate this phenomenon some dedicated simulations were performed, starting with an almost compensated beam, to better analyze whether the SCC is stable or not: the transient phase of the SCC was shortened by starting with a neutralization degree of 99.9% and the potential evolution is observed. Picture 4.9 b) shows the value of the potential depth $\phi_M = \phi(L_z/2, 0)$. An oscillating potential is found, reflecting the way the beam adjusts itself for maintaining its degree of neutralization: secondaries are expelled or accumulated depending on their charge and the potential oscillates between the points of maximum accumulation of both species. Compared to the beam accelerating voltages of 100 kV the amplitudes of these oscillations are relatively small, and tend to decrease in time; their effect on beam optics is negligible and the SCC

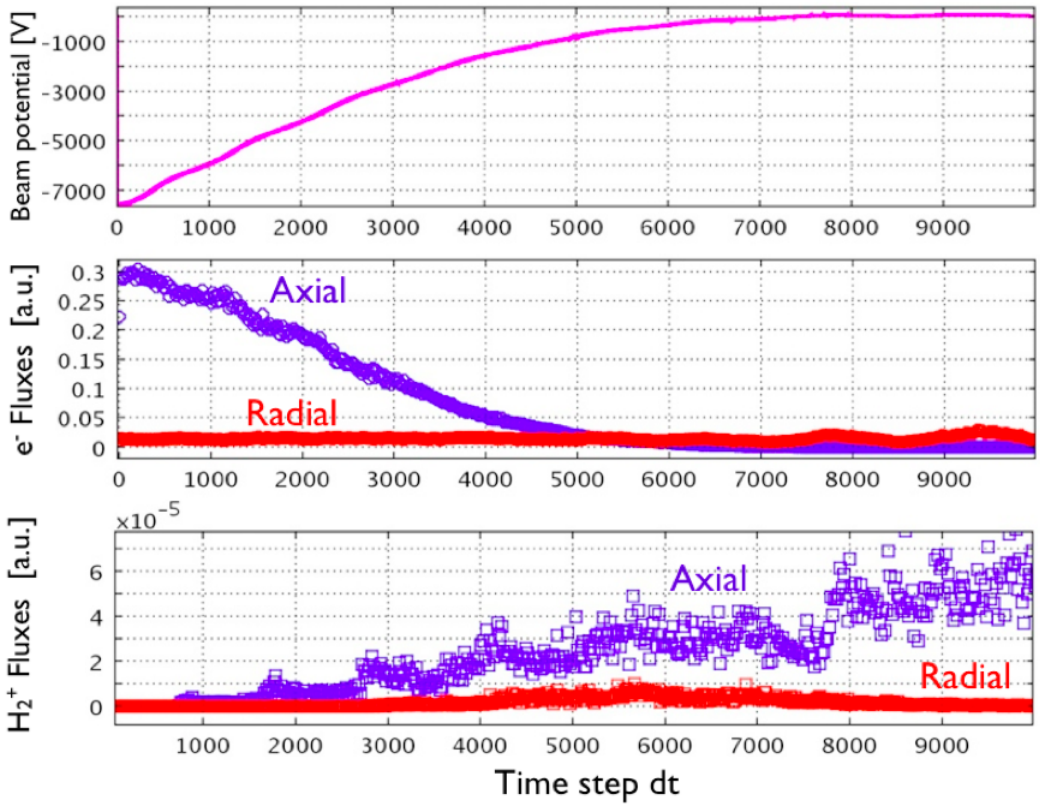

Figure 4.8: Particle fluxes leaving the domain. The particles exiting from the radial direction are reported in red, the ones exiting from the axial direction in blue. Circles identifies electrons and squares the ions).

appears basically stable.

The results on fluxes of H_2^+ ions expelled from the beam and leaving the domain in the axial or radial direction in this second series of analyses shows their correlation with the beam potential: ions leave the domain radially especially during the H_2^+ accumulating phase ($\phi < 0$) while, when potential becomes positive they are expelled axially, gaining an acceleration proportional to potential . Electrons follow a similar dynamics with opposite phase. So, in spite of the qualitative results of this simulation, an important topic was pointed out thanks to the 2D geometry: due to the fact that the radial potential is very small compared to the axial one, particles are expelled from the beam in all directions, meaning the dynamics of the phenomenon is not simply radial, as previously supposed. This aspect can also be highlighted by a direct comparison of the electric field values: during the stationary phase

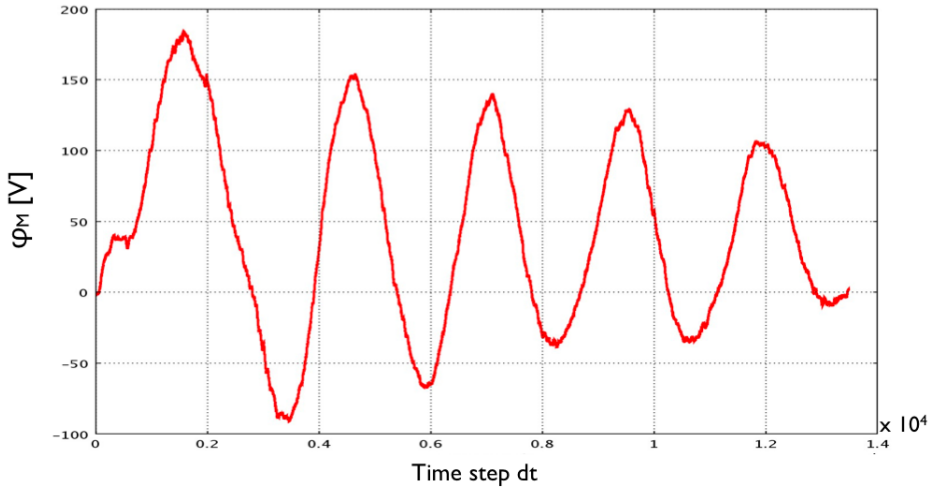

Figure 4.9: The evolution of the potential for the second kind of analysis are reported, showing the stability of the phenomenon in time.

of the SCC, considering the average radial potential difference $\Delta V_R \simeq 0.5\ V$ and the axial one, $\Delta V_A \simeq 50V$, a particle being in the beam center will feel an electric field having components

$$E_x \propto \frac{\Delta V_R}{L_x/2} \simeq 50[V/m] \tag{4.18}$$

and:

$$E_z \propto \frac{\Delta V_A}{L_z/2} \simeq 200[V/m] \tag{4.19}$$

Even if this result should still be weighed by taking into account the domain length ratio, favoring the radial expulsion of particles, the contribution of the axial dynamics still seems to be important. Further deepening on this kind of simulations was also discussed in [73] where the problem is studied with some ad-hoc developed fluid models also comparing the results of the Bypo model for the space charge compensation.

4.2 Beam-Surface Interactions

The interactions between the beams and the surfaces occur mainly by means of the secondary particles created in beam-gas interactions, whose dynamics was described previously. In case of direct collision of the beam with a surface, in fact, the power deposition could be so high to compromise all

the device, and the phenomena of interactions and production of particles becomes less important. (Conversely, the direct interception of the coextracted electron beam is usual on the extraction grid, and specific cooling systems are used to preserve the grid integrity) The processes involved can be divided in two main branches: the impact of electrons with the surfaces, which can bring to particle reflection or backscattering or secondary emission from surfaces, and the impact of heavy particles, mainly H_0, leading to secondary electron production and, in small part, to backscattering.
In the accelerator, this kind of interactions are modeled by means of the EAMCC code [78],[89], which accurately describes these phenomena[3]. On the other hand some accelerators, as in the case of SPIDER, include in the drift part of the accelerator, downhill of the grounded grid, a further structure, the *electron dump*, devoted to sink the power carried by the high divergence particle, mostly electrons, coming from the accelerator, before they damage more delicate structures. The electron dump, ED, cannot be included in the domain of the EAMCC code, and the studies of the interactions between particles and surface in this region required the development of ad-hoc models.

4.2.1 The BACKSCAT Code

The BACKSCAT code, developed in Comsol Multiphysics [74], can estimate the transmitted and dumped particle fluxes also taking into account the backscattering of the electrons impinging on the ED plates. The numerical environment allows a large flexibility in defining the 2D geometries to be treated: a simple COMSOL draw or CAD file can be used to define the problem domain, allowing to compare different ED solutions and designs. In the case reported here, the code implements the geometry of the SPIDER ED [90], consisting in vertical arrays of actively cooled pipes, where it was used to investigate in detail the power load deposition on the rear part of the grounded grid by means of electron backscattering from the pipes. The computational domain extends from the rear of the GG up to the end of the electron dump. The particle data are taken from the output of an EAMCC run, and injected 20mm downstream of the accelerator exit. Once the electron trajectory is calculated, with accurate solution of motion equation (max step size less than 0.5 mm) different models can be selected to account for the backscattering of electrons on ED tubes. The first model is based on the work by P.F. Staub [91], used also in EAMCC with few differences. The

[3]Some results and the application of this code is case of interest will be given in section 5.2 and 6, being outside the scope of this section

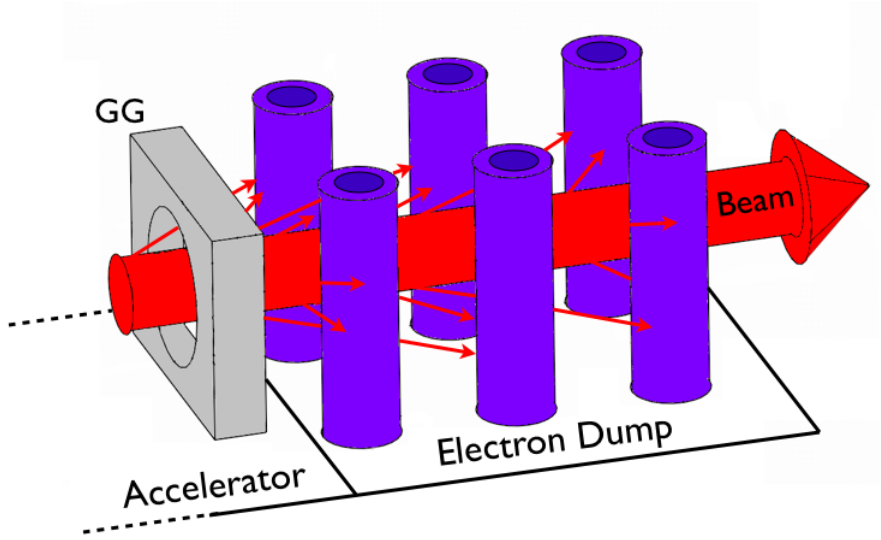

Figure 4.10: Schematic of a SPIDER-like electron dump system for a single beamlet. The small red arrows represent the high divergence beam particles, dumped on consecutive array of water cooled pipes.

probability for an electron impinging on a pipe to be backscattered is expressed as a function of the incidence angle θ between the particle trajectory and the surface normal and electron energy E_0.

$$\eta(\theta) = \eta_0 \exp(A_0(1 - cos\theta)) \tag{4.20}$$

where A_0 is obtained by fitting experimental data as:

$$A_0 = \left[1 - \exp(-1.83 E_0(keV)^{1/4})\right] \ln(1/\eta_0) \tag{4.21}$$

E_0 is the particle energy and η_0 is the probability to be backscattered at normal incidence ($\theta = 0$). The value of η_0 depends only on the material and has only a slight dependence on E_0, so that in our simulation the fixed value $\eta_0 = 0.25$ can be used with negligible error. The model also accounts for an energy loss of the primary electron on the impact point, so that the backscattered electron energy E_B, is:

$$E_B = E_0 \left[\frac{1}{\gamma}\left(1 - \frac{70|\ln B_\theta|^4}{\ln(S/P)^{(1/P)}}\right)\right]^{1/\alpha} \tag{4.22}$$

with:

$$S = \exp\left[\left(70|\ln B_\theta|^4\right)^p\right]$$
$$\gamma = 1 - \exp\left[-6|\ln B_\theta|^{-3/2}\right]$$
$$B_\theta = B_0\Big[\exp\left(\tau(1-cos\theta)\cdot\exp(\tau(1-cos\theta_2)\right)\Big]$$

B_0, τ, p and α are obtained from fit of two sets of experimental data [92],[93] and in our case their values are fixed as 0.27, 0.35, 0.27 and 2.2 respectively. P is a random number uniformly distributed between 0 and 1 and θ_2 is the angle at which the particle is backscattered (with respect to the surface normal) that has a random value in the interval $[-\pi/2, \pi/2]$, under the hypothesis of isotropic backscattering, well justified in our energy range.

The second model is based on the work by E.W.Thomas [94], which has a simpler formula for the backscattering probability:

$$\eta_B = 0.891 \cdot \left[\frac{\eta_0}{0.891}\right]^{cos\theta} \tag{4.23}$$

Where η_0 has the same meaning as in the model 1, but here his value is set to be $\eta_0 = 0.29$. This second model does not account for any kind of energy loss: backscattering electrons keep all the energy that they have before the impact. (Note that this is not a so strong approximation, since about 80 percent of electrons dont́ lose energy during the impact)

Results

The results obtained using BACKSCAT with the two different models are reported. Since the input data comes from the EAMCC code, which performs the simulations of co-extracted electrons and stripped electrons in two separate runs, BACKSCAT was adjusted to performed two runs too. The corresponding results are divided into two tables, in figure 4.11 (the first correspond to the co-extracted electrons the second to stripped electrons data), together with a benchmark with the EDAC code. EDAC is an old version of BACKSCAT, which accounts for the power loads on the electron dump structures, without the backscattering effect. For this reason the two codes were compared by deactivating the backscattering effect in BACKSCAT ($\eta_0 = 0$).

It can be observed that the agreement between the two codes is reasonable. The differences among the two models of BACKSCAT are due mainly to the energy transfer during the impact included in the first model. Since a

A) Co-extracted electrons data	EDAC Result		BACKSCAT (No Backscattering)		BACKSCAT Model 1		BACKSCAT Model 2	
	kW	%	kW	%	kW	%	kW	%
GG iron plate	0	0	0	0	33.1	9.9	42.6	12.7
1st tube array	136	41	137.2	41	118.3	35.4	111.7	33.4
2nd tube array	81	24.5	79.4	23.8	72	21.5	68.1	20.4
3rd tube array	63	19	66.7	20	54.2	16.2	50.2	15
Not dumped	50	15	50.4	15.1	55.6	16.6	60.1	18

b) Secondary electrons data	EDAC Result		BACKSCAT (No Backscattering)		BACKSCAT Model 1		BACKSCAT Model 2	
	kW	%	kW	%	kW	%	kW	%
GG iron plate	0	0	0	0	17.4	10.4	22.8	13.6
1st tube array	70	41.1	66.6	39.8	58.9	35.2	56.4	33.7
2nd tube array	56	32.9	52.5	31.4	47.1	28.2	44.5	26.6
3rd tube array	38	22.3	41.1	24.5	32.7	19.5	30	18
Not dumped	6	3.5	6.8	4.1	9.7	5.8	12.7	7.6

Figure 4.11: The result of the BACKSCAT code are compared with the result of the EDAC code and resumed. in Table a) the results corresponding to the coextracted electron simulations. In b) the data from the secondary electron.

richer physics is contained in model 1 this was selected as the reference for the following analyses.

It can be noted that the load recorded on GG refers to the whole left boundary, including also the hole, and so represents an overestimation of the real load on GG. A more accurate simulation was performed using the entire accelerator geometry. In this case the particles traveling backward toward the source are subjected to the electrostatic and magnetic fields of the accelerator once they cross the GG. Some sample trajectories for this case are reported in figure 4.12. Anyway, in the standard case were the restricted domain starting from the GG was used, we should consider the fact that BACKSCAT uses a planar model where the back- streaming current is overestimated by a factor proportional to the ratio between the hole of area πr^2 and the square with area $4r^2$, r being the hole of GG. Finally, being the geometry of the code fully parametric, it allows easy scans of geometric parameters of interest. In particular a set of simulations were performed with variations in the gap d between the first tube array and the grounded grid. The results of this kind of analysis, as reported in figure 4.13, confirm the results of EDAC about the optimum value of d (about 33.5 mm) which minimize either the power load on the GG and the power not sinked on ED. The final design of the electron dump obtained by this kind of numerical modeling[95] was implemented, and a schematic of the whole accelerator can be found in figure 5.1.

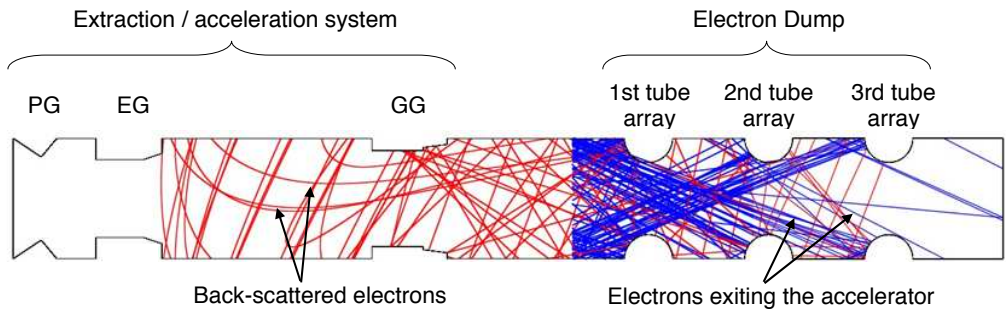

Figure 4.12: Sample trajectories of the BACKSCAT code. The extended domain is shown, also including the accelerator region.

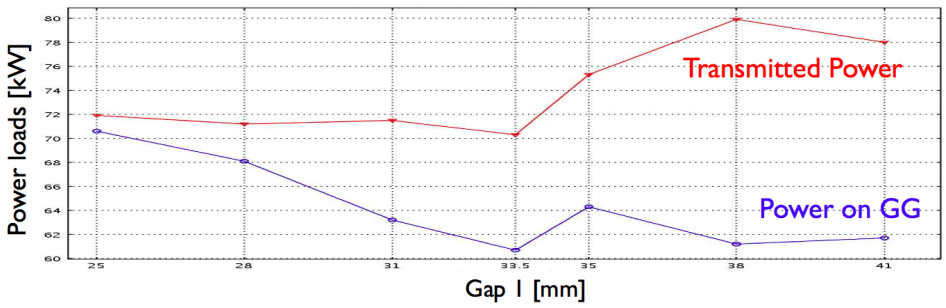

Figure 4.13: Sensitivity analysis on the value of the gap 1 between the end of the GG and the first array of pipes of the ED.

Chapter 5

The Full RFX Suite of Codes

In the context of the of the research on the neutral beam injection at *Consorzio RFX*, the most important step is represented by the design and development of two experiments: the SPIDER source and the MITICA injector, whose characteristics were described in 1.3.1. In the perspective of designing and developing this complex devices the modeling hold a fundamental role, allowing to better understand the physics involved and giving preliminary estimation on the expected performances. Since the neutral beam injection present dozen of coupled physical problems, spanning from atomic physics to materials science, accelerators and plasma physics, the use of several code is needed to have a full point of view of the entire problem. From the last years the NBI group of *RFX* is involved in the set up of a complete suite of models and numerical codes and tools devoted to investigate all this aspects, acquiring the state of art codes from other laboratories or commercial company, and developing its own models and codes where necessary. At the same time specific work was required to interface this codes each other, allowing them to exchange informations and data, to obtain results and estimations more and more reliable. The first part of this chapter will present shortly the most important of this codes, while in the second a practical example of their use is given with the designing and optimization of the SPIDER source. The last section contains some preliminary considerations on a benchmark performed between some of this codes and real experiments.

5.1 Summary of Codes

Here I will shortly describe only the most important codes used at RFX for estimations of the beam acceleration and heat loads, quoting the relative references, since the whole list include several codes and a complete descrip-

tion of all of them is unuseful at this point. Some of them, as Bypo or BACKSCAT, also if widely used, were omitted in this sections, since their description was already given is sections 3.4 and 4.2.1 respectively.

SLACCAD

The SLACCAD code is a modified version of the SLAC code [96], developped at the Stanford laboratories in the '70 to deal with electrons acceleration. The implementation of the negative ions, including beam attenuation and a free plasma boundary is due to J. Pamela and its group [62]. At present it simulates the acceleration of negative ions in a linear accelerator, considering a 2 dimensional axial symmetric geometry, giving self consistent result on the potential distribution due to both accelerating electrodes and space charge distribution of the beam. In spite of the fact that it neglects many physical aspects such the magnetic field, the electrons space charge and the absence of any kind of plasma physic calculation, thanks to its long-time usage on different laboratories it is considered one of the most stable and efficient code to calculate the single beamlet optics for negative ion beams. It also includes some satellite modules to calculate the grid conductances (CONDUCT), the pressure profile and stripping losses (STRIP).

OPERA

OPERA is a commercial code belonging to the Cobham group [60]. Its environment include several modules to deal with different physical problems. At RFX, in particular the module SCALA and TOSCA are used. The first of them is devoted to calculate the tridimensional space charge deposition of beams of particles, including, in the latest issue the stripping losses for negative ion beams, while the second focus on the magnetic field calculation, considering permanent magnets and flowing currents. In SCALA the beamlet is been simulated by launching a large number of macroparticles from a suitable emitter surface generated with a macro in MATLAB. The two modules can also be coupled to obtain the trajectories of negative ion beams in the full electromagnetic environment. Moreover the flexibility in the geometry definition allow the simulations of several beamlets together, with the possibility to study the mutual beamlet beamlet interaction and related effects.

EAMCC

The code EAMCC (Electrostatic Accelerator Monte Carlo Code), developed at CEA [1] by G. Fubiani [78], is devoted to investigate the beam transmission inside the accelerator, considering the interaction with the residual gas and the surfaces and the consequent production of secondary particles. The atomic interaction of the beam and the creations of secondaries is modeled with a Monte Carlo approach, while the electric and magnetic field are imposed a priori from third part codes, usually SLACCAD for the electric field and OPERA for the magnetic field. EAMCC is used to obtain estimations of the heat load on the accelerator grids, and to acquire informations on the beam transmission and composition. In the past years the relativistic correction of the motion equation and the 3D geometry allowed this code to obtain reliable results on different geometry of interest, including the comparison between the Mamug and Singap concept foreseen for the ITER NBI [89].

Codes Enhancement and Adaptation

Sometimes modifications of the codes appeared necessary to include new effects. In particular, in SLACCAD, the code "CONDUCT" was substituted by a new code which calculates the grid conductances with a better approximation, allowing to evaluate the conductance for tapered holes and takes into account the effects of using gases other than D_2. In order to handle the interaction of SLACCAD with the accompanying codes and with the post-processing routines, a suitable graphical user interface was developed, having the possibility of handling multiple analyses and allowing initializing hundreds of simulations at once. The interactions between EAMCC and SLACCAD, was completely integrated with the development of an user interface in Matlab [27] environment, allowing to deal with both code parameters and yielding a common file which perform both the models, also managing the simulations of ions and electrons, which were performed separately in the standard version of EAMCC. Moreover defining a special system of labels for the output file it makes simple to recover the results in a single database, in order to have a fast consultation and comparison of the run of interest.
Also the post-procesing routine of EAMCC was completely re-written in MATLAB, to have the possibility to directly deal with the data, export the power loads and obtain the beam transmission data and diagnostics in a single run.

[1] Commissariat á l'Énergie Atomique, France

5.2 Modeling of the SPIDER Source

The device specification were already given is section 1.3.1, as results of extensive analysis performed with the help of the full set of codes. Since the author of this thesis was mainly involved in a second part of the design, consisting in the exploration of the off normal condition that the device can met during its operational phase, the use of the codes mentioned in the previous section will be given in that context, and only a short summary of the simulations devoted to designing the source will be given first. For details on this first kind of analysis I remand to [76].

5.2.1 Design and Optimization

The simulations carried out during the accelerator optimization phase led to the present design, reported in figure 5.1 for the single beamlet frame. The major responsible of the beamlet optics are the values of grids voltages, together with the electrodes shape and the distance between them. For their

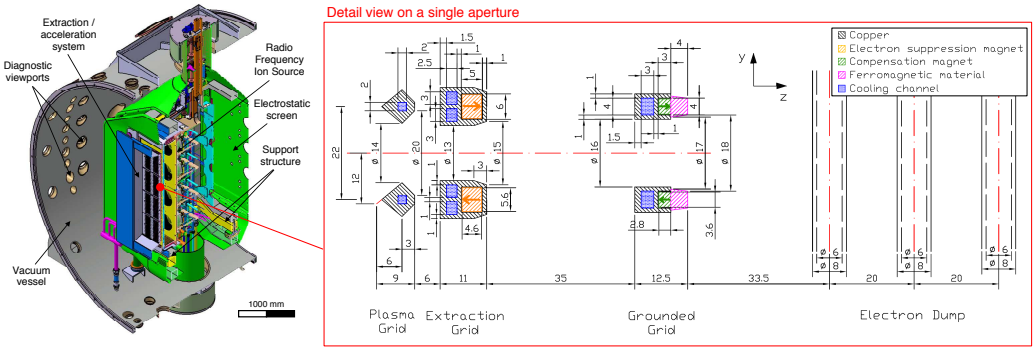

Figure 5.1: Vertical section view of the SPIDER Extractor/Accelerator system and Electron Dump. All the dimensions are in mm.

optimization, in principle, some single beamlet optics analysis are sufficient, and they were carried out by means of the SLACCAD code. In particular a large set of crossed analysis with variation in the extracted current density and voltage of the EG were performed, and their effect on the beam optics quality was measured in terms of beam divergence. Then the OPERA code was used to consider the tridimensional effects, to account for the beamlet beamlet interaction and to include the effect of the magnetic field in the beam calculations. Comparison between different magnetic field configurations, for both the extractor field and the source filter field were done with TOSCA.

About the interaction between beamlets, also the IRES code (Ion Relativistic Equation Solver)[97], developed at Consorzio RFX was used, showing good agreement with the OPERA results. OPERA was also used to evaluate the effects of grids offset inside the accelerator to compensate the beamlet deflection. In fact, in the presence of an offset among the apertures, due to the curved shape of the equipotential surfaces, the beamlet is deflected, and this effect is exploited to compensate the deflections the beamlets suffer for the mutual beamlet-beamlet repulsion or for the presence magnetic field in the extraction region. After a comparison between different proposals, the adding of permanent magnets also inside the GG was selected as the best solution to compensate the beamlet deflection. In the context of the grid alignment optimization between the grids the ALIGN code, internally developed at RFX, was used. For the estimation of the power load deposition, due to secondaries inside the beam useful to dimensioning the cooling systems, the EAMCC code was used, and its output data were used to evaluating the grid deformation and the thermal stresses by means of the commercial code ANSYS [98] also benchmarked with COMSOL[74]. Further aspect of the source operation, as the cesium effect or the operating temperature can only be tested experimentally, and for this reason the design have an high degree of flexibility, in order to allow further modifications and optimization during the experimental phase.

5.2.2 Exploration of Off-Normal Scenarios

As it is expected that the accelerator shall operate also in case of pre-programmed or undesired off-normal conditions, the investigation of a large set of off-normal scenarios was necessary for the evaluation of the real performances of the machine, and to help in interpreting experimental results, or in identifying dangerous operating conditions.

Influence of Field Dishomogeneities

In order to investigate the consequences that the device could experience in case of voltage ripples and to individuate trends of interest helpful in optimizing the accelerator divergence, some sensitivity analysis on the EG voltage were performed on the latest version of SPIDER, by means of the SLACCAD code, considering as reference parameter the value of θ_{RMS}. This is defined as:

$$\Theta_{RMS} = \sqrt{\frac{\sum_i |r_i| \theta_i^2}{\sum_i |r_i|}} \tag{5.1}$$

i.e. the root mean value of the average divergence angle of single particles, weighed over the radius, to respect the 2D axial-symmetry of the model. The results are plotted in figure 5.2. The points found by SLACCAD numer-

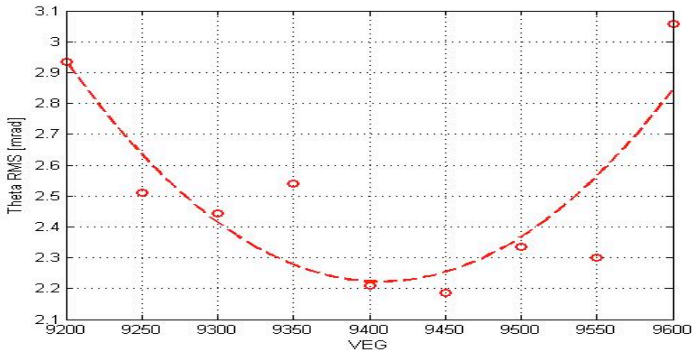

Figure 5.2: SLACCAD analysis of Θ_{RMS} as a function of the EG voltage.

ical simulations are fitted with a second degree polynomial curve to better highlight the trend. The beam divergence results fairly constant for small variations of the voltage around the reference value of 9.4 kV, corresponding to the best quality of the optics. Regarding the magnetic field, one case of interest is the lack of homogeneity that can be caused by the inefficiency of one of the permanent magnets embedded in the grids, due to manufacture inaccuracy, or, more likely, to loss of the magnetic properties in case of magnet overheating. In fact the extended exposition to heat loads could statistically cause losses of magnetization also with temperatures well below the Curie temperature of the magnet, which is about 800 °C. The worst case has been tested, namely a total failure of the magnet in the EG, where the largest fraction of electrons should be filtered. To model this effect, a 3D OPERA analysis was performed using an array of vertical beamlets, with one of the magnets turned off. Figure 5.3 shows the consequent magnetic field behavior with respect to the case of a nearby functioning magnet. The resulting magnetic field basically preserves its distribution along the z direction, but the field intensity is decreased roughly by 50%. The field of surrounding beamlets results unperturbed. Both the beam optics and the heat loads are affected by this failure. As a consequence, under the effect of the compensating magnetic field of the GG, the beamlet suffers a strong over deflection, estimated with OPERA itself in term of the angle $\beta = -3.35$ mrad, with respect to $\beta = 0.02$ mrad in the reference case. To account for the variations in terms of power deposition of co-extracted electrons and the secondary they produce, some analysis in EAMCC were carried out to ac-

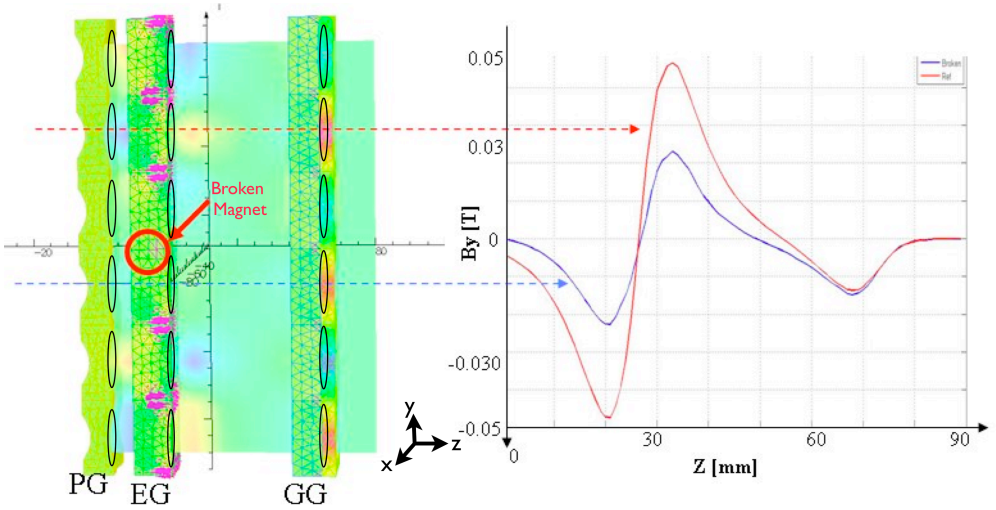

Figure 5.3: OPERA Analysis of a vertical array of SPIDER beamlet. One of the magnet embedded in the EG, in the red circle, is turned off. The consequent modification in the field behavior is visible in blue on the right side plot, together with the behavior of the reference case field, in red, corresponding to a nearby hole.

count for the relative heat loads. The total power deposition on EG is quite similar in both cases, but in case of broken magnets, the smaller magnetic field causes more electrons to impinge in the inner cylindrical part of the EG, aperture where they produce additional secondaries or being backscattered toward the accelerator exit, gaining the full acceleration. This results in a significant increasing of the load on the GG, which passes from about 300 W per aperture in the reference case to more than 430 W; this values, however, are still well manageable by the cooling system.

High Pressure Scenario

The pressure in the source is strictly related with the needs of containing the stripping losses in the accelerator and the investigation of its distribution in the whole NBI was the subject of several studies [99]. The values usually assumed in standard modeling, are about 0.3 Pa for the source pressure, and 0.05 Pa for tank pressure. The uncertainty on this parameter, due to difficulties to directly control it in the source, justifies the following series of analyses. A first test was performed with SLACCAD, setting a fixed value of 0.05 Pa for the tank pressure, and by varying the source pressure around the

reference value. It should be noted that since SLACCAD accounts for the pressure difference between source and tank only with the module "STRIP", by calculating the stripping loss profile inside the accelerator. Therefore such variation affects the space charge deposited by the rays representing the macro particles along their path, which, in turn, can cause small differences in the beamlet divergence. The resulting trend clearly exhibits a minimum close to the reference value. This result is not surprising, since the whole accelerator was optimized for this pressure. Changing the value of the tank pressure has an even smaller effect on the optics, since it affects the pressure profile only in the final part of the accelerator, where the largest part of the stripping has already occurred. However, a similar trend could be identified, showing an increased Θ_{RMS} for increasing pressure In case of high pressure, a larger amount of secondary particles is produced and accelerated by the electric field. In order to estimate the consequences on the device components in terms of thermal stresses, some analyses were done with the EAMCC code, capable of quantifying these secondary fluxes and the power load they deposit on the accelerator grids. The same quantities were then estimated in the electron dump with the code BACKSCAT code. To simulate the worst condition of loads, the value of 0.5 Pa of source pressure was imposed in both codes, whose results compared with the loads for the reference pressure value are resumed in the table reported in figure 5.4. Even if the thermal stress

Pressure [Pa]	**EAMCC**					**BACKSCAT**			
	Transmitted Particles [kW]			**Thermal Loads [kW]**		**Thermal Loads [kW]**			
	H-	e	H0	EG	GG	GG_{rear}	P-1	P-2	P-3
0.3	5720	400	330	666.4	470	50.5	177	119	87
0.5	5150	480	420	685	584	65.4	228	150	112
Variation %	-9	+17	+21	+3	+20	+23	+22	+21	+22

Figure 5.4: Result from the EAMCC and BACKSCAT code for the transmitted particles and heat loads on the SPIDER components, for the 0.3 and 0.5 Pascal source pressure scenarios.

of the grids and pipes increases, they are still manageable by the cooling system, which is dimensioned to tolerate load 100 percent greater than the reference case; the increased flux of back- streaming ions is acceptable too. The BACKSCAT code also allows evaluating the power deposition on the rear of GG due to backscattering electrons, and, since its value is not negligible in both cases, adding a dedicated cooling system in the GG was necessary to protect the ferromagnetic material.

Extracted current ratio sensitivity analysis

The ratio between the extracted current of negatively charged particles, defined as $Rj = J_e/J_{H^-}$ is another parameter difficult to be controlled, which can have consequences on the performances of the device. Since the electron space charge is distributed asymmetrically in the accelerator tube, following the suppression magnetic field, the negative ions beam optics could be influenced in case of high value of R_j. The Bypo code was used for this kind of analysis, being the unique code which accounts for the space charge of both electrons and ions together. The results, in 5.5 show the behavior of Θ_{RMS} with respect to R_j. Here only slight variations around the values of R_j sug-

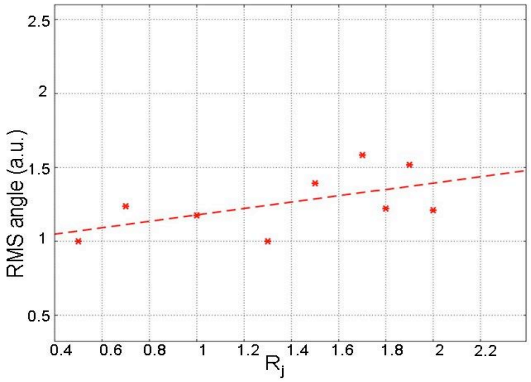

Figure 5.5: Bypo sensitivity analysis on the R_j parameter. Numerically found points and their trend. Note the Θ_{RMS} value in normalized to the minimum.

gested by the IPP experience ($0.5 \leq R_j \leq 1.5$) were performed. Note that the values of Θ_{RMS} of Bypo are not comparable with those given by SLAC-CAD, due to the different symmetries of the models (2D Cartesian and 2D axially symmetric respectively). A clear trend is however found, and the fit shows increasing beam divergence for increasing extracted electron current.

Mechanical Modification

The thermal expansions and the bowing of the grids, due to the load of impinging electrons, the electrostatic pressure of nearby grids and the vibrations of the whole device, could all have influence on beamlet optics. The net effect is, in all cases, a variation in the accelerator geometry, resulting in an offset of the accelerating grid apertures in the horizontal (x-axis) and vertical (y-axis) directions or in a shift of the grid along the beam direction

(z-axis). The in-plane grid offset, corresponding to a misalignment which causes an electrostatic deflection of the beamlets, is due to thermal loads on the grid; these phenomena do not affect the entire grid in the same way but are more effective in the more external rows with respect to the positions where the grids are supported (fixed points). The effect has been minimized by an appropriate cooling: in the horizontal direction the shift should remain under 0.2 mm and in the vertical it is even negligible. An estimation of the beam deflection due to this expansion can be found by exploiting the linear relationship found in previous works [90] between the grid offset δ and the beamlet deflection angle α:

$$\alpha[mrad] = K \cdot \delta[mm] \tag{5.2}$$

with K=7.7 for the EG and -8.06 for the GG. With our values the deflection stays under 1.5 mrad which respects the requirement for the grid alignment. Another contribution to the misalignment could come from the expansion of the support frame of the grid, which accounts for other 0.1-0.2 mm in the worst case. This effect is accounted at the expected steady-state temperature of the support frame in beam-off configuration, setting an offset in the fastening position of PG, EG to the support frames; notice that aperture misalignment will rise during beam operation. In the case of a grid shift in the z-direction, the effect is a variation in the beamlet optics. The thermal expansion is expected to shift the grids in the beam direction by 0.1 mm for the EG or 0.6 mm for the GG. Also in this case, in spite of the smaller shift value, the EG deformation is the principal responsible of the beam optics variation, and the analysis were oriented towards its modification. Also in this case, the deformation of the support frames of the grids could increase the total shift, acting on the whole grid in a homogeneous way. Some preliminary analyses showed large values of the shift of the whole grid (about 0.5 mm), calling for further investigations and possibly reference configuration adjustment to the actual design. Another factor which can change the z-position of the EG is the electrostatic pressure of nearby grids. The consequent shift can be estimated, by considering the EG and GG as two slabs of copper having length L, height h and thickness s as

$$\delta = \frac{5}{384}\frac{qL^4}{E_y \cdot I} \tag{5.3}$$

where $E_y = 1.1 \cdot 10^{11}$ [N/m2] is the elastic modulus for copper, I the moment of inertia of the slab and $q = (\epsilon_0 \cdot E^2 \cdot h)/2$, the load due to the electric field. The resulting δ value, representing the maximum shift which is expected in the grid centre, is about 0.1 mm. Even in the case of breakdowns of the

system, when this load suddenly disappears and the grid a start vibrating around its nominal position, the amplitude of this oscillation stays below δ. Obviously a similar effect should be expected for the PG-EG interaction, but the potential difference is much smaller, so the electrostatic pressure in the backward direction is lower. The SLACCAD analysis reported in figure 5.6 shows the result on the beam divergence of different positions of the EG with respect to the nearby grids, to account for all the conditions which can cause a grid movement. The trend highlighted by the fitting curve suggests

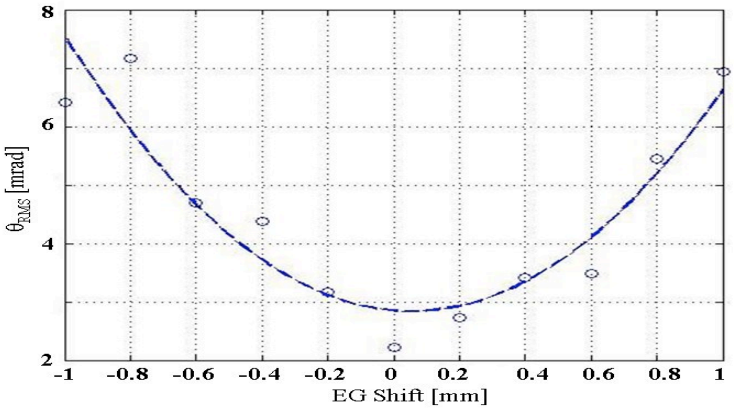

Figure 5.6: SLACCAD sensitivity analysis of the EG position along the beam direction. The 0 correspond to the design value for the EG position: 6 mm after the PG and 35 before the GG.

that for small grid deflections the beam quality stays almost constant, but it rapidly decreases in case of larger values of the shift.

These kind of analysis on the SPIDER source showed the usefulness of the modeling, to design the device, explore particular operational conditions and aiding its experimental phase. SPIDER appeared basically stable to quite all the off-normal conditions tested: beam optics reasonably keeps its quality for small deviations of quite all tested parameters and the cooling system is expected to handle the increased thermal load in the structures without particular problems. In the cases where the thermal load increase was unacceptable, some modification to the cooling systems were implemented, as it was the case of the overheating of the ferromagnetic material covering the rear part of the GG. The preliminary analysis of the support frame deformation for the accelerator grids revealed higher values than expected. Since this effect could affect the beam divergence, further investigations are foreseen.

Chapter 6

Code Benchmark

A collaboration between RFX and the Japanese laboratory of NIFS [1] was established in the latest years, with the purpose of benchmarking the models and numerical codes with existing experiments , and to prove the accuracy of the simulations and the soundness of the SPIDER and MITICA design. At the NIFS laboratories, in fact, the world largest negative ion based neutral beam injectors are installed on the LHD helical device[100],[101],[102], designed to inject 15MW of power in the plasma. In this section, after a short introduction to the characteristics of the injectors, an overview of the current status of the benchmark will be given, comparing the estimated power load deposition with the experimental data, and benchmarking the beam optics code.

6.1 LHD Beam-lines at NIFS

In the LHD experiment, the largest existing helical device, the plasma heating is mainly sustained with neutral beam injection. A set of 5 beam lines is presently installed, 3 of which use the acceleration of negative ions, representing the state of art devices of this kind. It is convenient to note that through NIFS also hosts a dedicated test bed for negative ion acceleration and neutralization, benchmarks with this injector were not performed, since the present codes are not compatible with the geometry; the test bed accelerator which features a *multi slotted* grounded grid, where several beamlets pass through the same slit in the grid; this shape was found to drastically reduce the conditioning time of the accelerator. At the moment this feature can not be implemented in the single beamlet codes SLACCAD and Bypo, and also EAMCC, even if 3 dimensional, can not deal with it, since its geometry is

[1] National Institute for Fusion Science

obtained from a simple revolution of the SLACCAD geometry. The same kind of GG was successfully installed on the beam line 1 [103],[104], leaving the beam line 2 (BL2) as the best candidate for the code benchmark.
BL2 features 2 arc driven negative ion sources, placed side by side and facing a 4 grids acceleration system. The injector set up is shown in fig 6.1, while the accelerator is in figure 6.3. The accelerator is constituted by a plasma

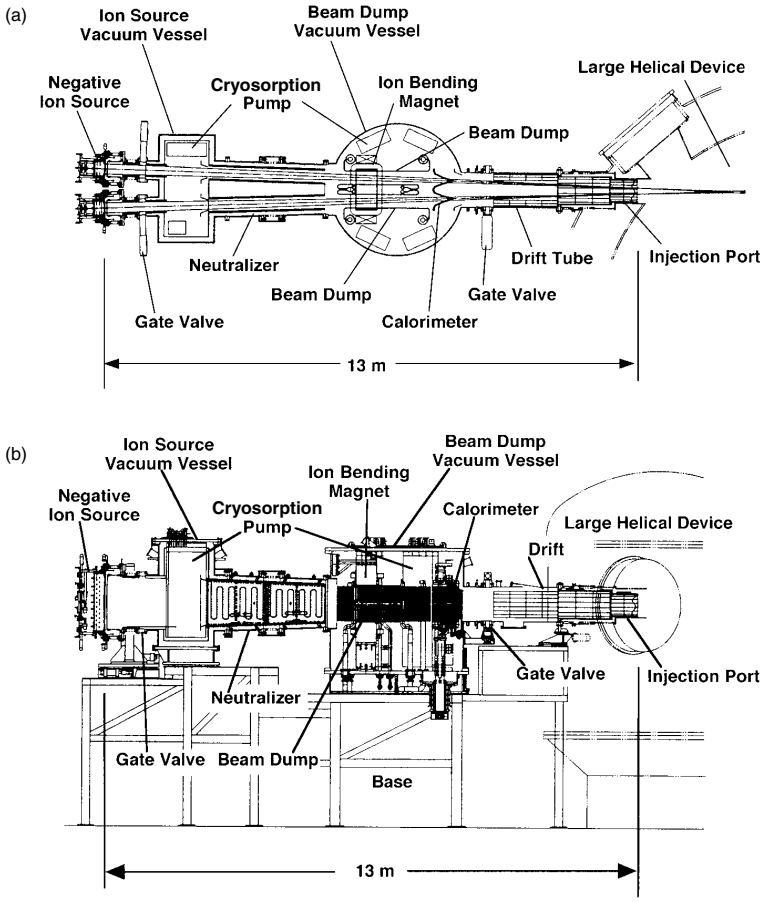

Figure 6.1: (a) Plan view and (b) an elevation view of the beam line number 2 of the neutral beam injection system of LHD experiment. The picture was taken from [102].

grid with classical tapered holes, the extraction grid, also embedding the magnets for deflection of the coextracted electrons and a dedicated cooling system, a steering grid (SG) , biased at the same potential as the EG and dedicated to correct the beam deflections by grid offset, and a multi-rounded grounded grid. Once accelerated the beamlets coming from both sources are

neutralized via a gas stripper and the residual ions are deflected by means of dedicated magnets, so that the neutral beam can be injected into LHD after a drift distance of some meters. Along its path the beam can be intercepted by 2 calorimeters, the first positioned just after the ion dump, about 9 m downhill of the source, the second directly installed on the LHD inner wall, about 20 m far from the sources. The nominal injector energy and power are 180 keV and 5 MW respectively. The schematic of the whole device, is reported in figure 6.2, also including a view of the heat load measurements, while figure 6.3 reports a sketch of the accelerator.

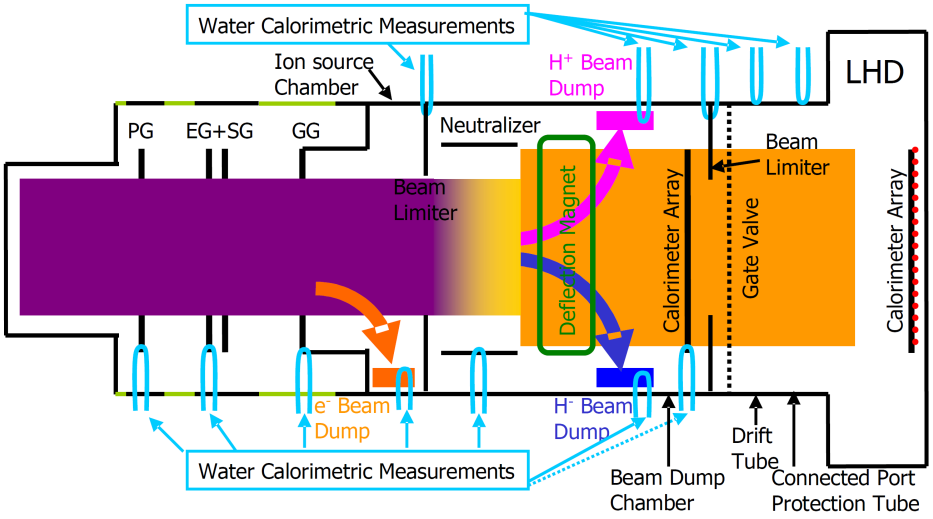

Figure 6.2: Schematic view of the beam line 2 injector

6.2 Power Load Deposition benchmark

The goal a first benchmark, was the compare the measured values of the power load deposition measured on the accelerator grids by calorimetric diagnostics with analogous data obtained from numerical simulations exploiting the codes previously described.

6.2.1 Experimental Measures

The pressure distribution was measured in the source by ion gauge, finding the value of $p_{fill} = 0.25$ Pa in the source, without the plasma. For the pressure value in the vacuum tank downhill of the GG, also needed by

the codes, the value p_{tank}=0.08 Pa was guessed from indirect measurement. Since this pressure distribution was measured without the plasma, the effect

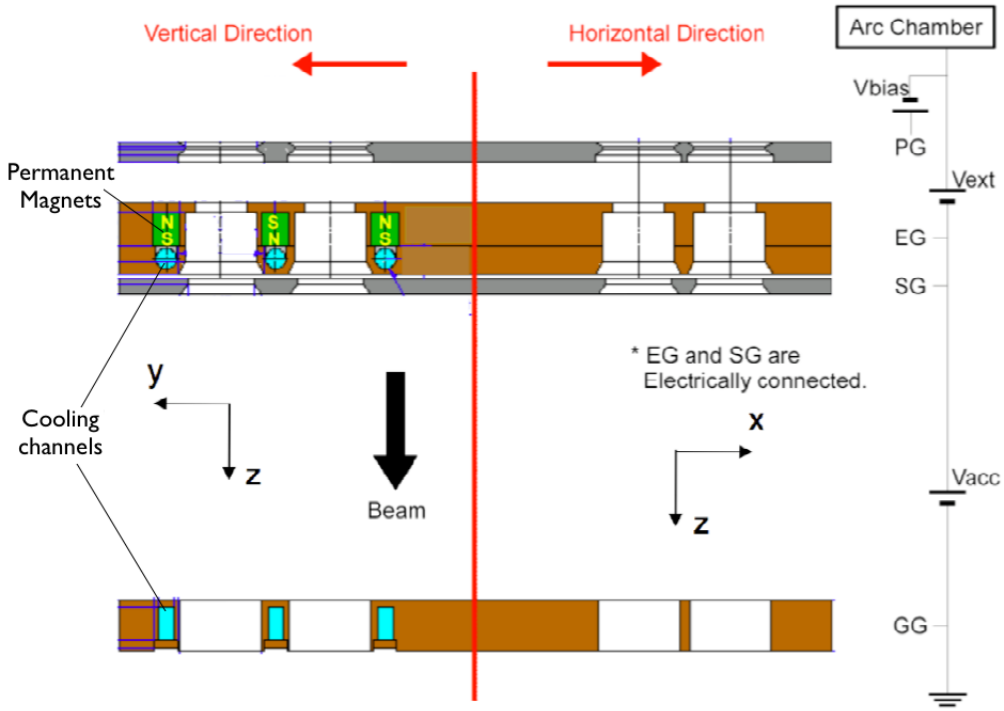

Figure 6.3: Sketch of the LHD beam line 2 accelerator: horizontal and vertical view.

of temperature is missing. To take into account its effect, it should be noted that with a fixed flow rate and molecular flow conditions, the molecular velocity inside the accelerator increases as the gas temperature increases, and the grid conductance increases as well. For this reason the correction to the source pressure:

$$p_{eff} = p_{fill} \cdot \left(\frac{T_{room}}{T_{source}}\right)^{1/2} \tag{6.1}$$

was used, following the model proposed by Krilov and Hemsworth [99] and using the values of T_{room}=300 K for the room temperature, and a set of value for the source temperature ranging from 1000 to 5000 K, due to the uncertainty on this parameter. The first analyses were focused on a single shot result, the shot 98006, whose characteristics are summarized in table 6.1: Note that the values of I_{extr}, I_{acc}, P_{EG} and P_{GG} correspond to the sum of data from both sources. For the power load data, the values are obtained from the

Shot 98006: Experimental Data			
Pulse length	Δt	[s]	1.96
Extraction Voltage	V_{EG}	[kV]	9.7
Acceleration Voltage	V_{GG}	[kV]	172.7
Extraction current	I_{extr}	[A]	91.9
Acceleration current	I_{acc}	[A]	70.5
Average Power on EG	P_{EG}	[kW]	312
Average Power on GG	P_{GG}	[kW]	1189

Table 6.1: Summary of data measured for the shot 98006 in LHD-BL2 Injector.

calorimetric measurement starting form the total energy absorbed by each component, which can be estimated by integrating the power carried away by the cooling water during and after the pulse, according to the formula:

$$E_{tot} = \int_0^{\Delta t} f_w C \Delta T dt \tag{6.2}$$

where C is the heat capacity of water, f_w its flow, ΔT the difference between the inlet and outlet temperature of cooling water during and after the pulse. From E_{tot} the total power deposited can be obtained by simple division by the pulse duration time Δt:

$$P = \frac{E_{tot}}{\Delta t} \tag{6.3}$$

6.2.2 Numerical Simulations

The codes used for simulating the shots are SLACCAD, for the potential distribution, including its satellite codes for the stripping losses and pressure profile calculation, and TOSCA for the magnetic field evaluation, considering both the co-extraction field due to permanent magnets in the EG and the filter field inside the source. Notice that a detailed benchmark specifically dedicated to the magnetic field was performed in a recent work [105], showing a very good agreement between the experimental measures and the codes TOSCA, ANSYS[98] and PERMAG [106]. The electric and magnetic fields are fed to EAMCC code in order to evaluate the power depositions on the structures of the injector. In order to correctly estimate the current density emitted form the source, in terms of the contributions from ions and electrons, a preliminary calibration of the code was needed, by running the simulation with some reference values, that was tuned in a second moment

to match the values of current measured by the power supply of the injector. This procedure, explained in detail in [107], allows to obtain the numerical power load deposition, and to estimate extracted negative ion and electron current density. The result of the codes for the shot 98006 are reported in

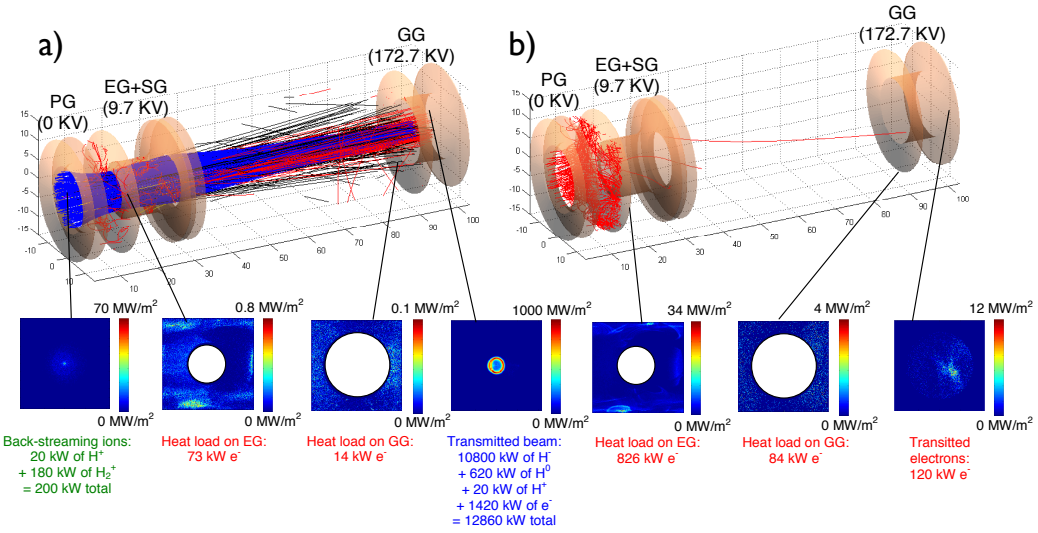

Figure 6.4: EAMCC simulation (a) of a negative ion beamlet and relative secondaries and (b) of the co-extracted electrons in the LHD BL2 accelerator showing some samples particle trajectories (electron in red, H^- in blu and H_0 in black) and the relative surface plot of the heat loads transmitted and on grid.

figure 6.4 and summarized in the following table, reporting data from high and low temperature scenarios: As is evident from a comparison with the experimental data reported in the previous table, some discrepancies between data are present in the power load deposition. In particular, if the differences in the power load values on the EG are small, the situation for the loads on GG is drastically worse, showing numerical values from 2 to 3 times smaller then the measured data. Other simulations were performed with different shots, but the results were similar. Even if the reason of this discrepancies is still an open point, some hypotheses were proposed to explain them:
Uncertainty on pressure distribution: since the pressure can only be measured without the plasma on, some underestimation of its value is possible. Higher pressure in the source (and in the accelerator gaps by consequence) will cause more secondary to be produced and accelerated, increasing

Shot 98006: Numerical Results			
	$T = 5000\ ^oK$	$T = 1000\ ^oK$	
Accelerated H^- current	69	75	[A]
Accelerated e^- current	15	22	[A]
Extracted electron to ion ratio	0.2	0.33	
Stripping losses	15	22	%
H^- power at accelerator exit	10.9	11.9	[MW]
e^- power at accelerator exit	1100	1400	[kW]
H^0 power at accelerator exit	270	460	[kW]
H^+ power at accelerator exit	10	40	[kW]
Total Power on EG	220	271	[kW]
Total Power on GG	384	527	[kW]

Table 6.2: Results of numerical codes on LHD-BL2 injector.

the power load deposition on all grids, and particularly on the GG. Another possible and more reliable cause of wrong estimation of the pressure could come from the fact that the tank pressure needed by the code was estimated on the basis of a measure of pressure performed in the ion source vacuum vessel just before the neutralizer (see figure 6.1), where the value $p_{vv} = 0.8$ Pa was found; then, a rough estimation based on the geometrical ratio between the vacuum vessel volume and the volume of the duct at the end of GG gave the value $p_{tank} = 0.08$ Pa used in the codes for the tank pressure.

Beamlet halo: The beamlet halo constituted by high divergent fraction of the primary beam could represent a cause of additional power on the structures with an additional increased load of true secondary electrons due to heavy ion impacts on grids. The EAMCC code implement the possibility to add a beamlet halo effect in the simulations, but the run on LHD BL2 were performed without this effect, which, in similar cases, was found responsible of large increases in the thermal load on the grids. Anyway it is worthwhile to note that some experimental measures performed with a beamlet monitor on the BL2 seemed to suggest a negligible halo fraction.

Enhanced secondary production: Another possible cause of underestimation of the power load could be given by physical effects not considered in the code, which can enhance the production of secondary electrons from the surfaces. For instance, there was experimental evidence of the presence of cesium on the front part of the GG, in a quantity sufficient to form a monolayer on it. Since the cesium can reach the GG only by flowing as Cs^0 from the source into the accelerator, its presence on the back side of EG and SG is likely. In this case the production of secondary partickes on the Eg

and SG downhill surface, and their acceleration toward the grid downhill is expected to increase due to the lowered work function of the grid surfaces. The some phenomena could also be responsible for production of negative ions H^- on the conical external part of the PG. This ions will have a bad optics and increase the halo. In any case, since there are no experimental evidences for any of these hypothesis, further work to better investigate the causes of this discrepancies should be addressed.

6.3 Beam Optics Benchmark

In order to obtain a direct benchmark of the beam optics codes, without passing trought the calorimetric measurements, subject to errors in pressure estimations, a perveance match experiment was performed on the BL 2 of LHD experiment. The codes used for the benchmark in this case were SLAC-CAD and Bypo, both previously described in this work, in sections 5.1 and 3.4 respectively. The codes were set up to meet all the characteristics of the real shots in term of voltages, geometries and extracted current density. The currents can be evaluated considering the extraction and acceleration currents measured on the power supplies, according to their set up reported in figure 6.5. With these measures a rough estimation of the extracted currents

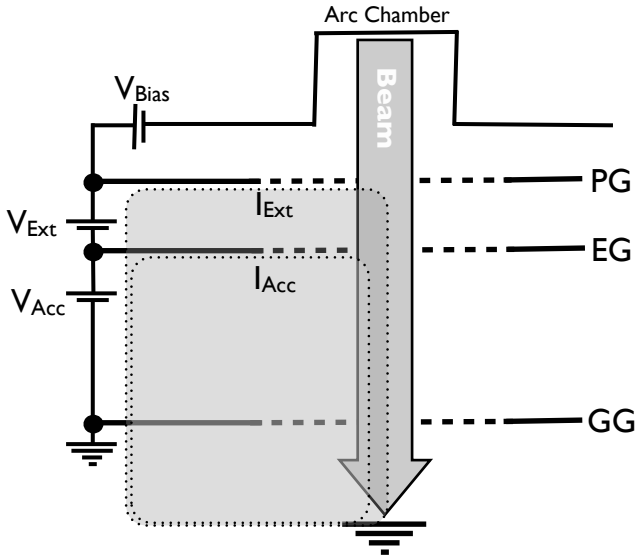

Figure 6.5: Schematic of the current measures and power supply of the BL2 accelerator.

can be obtained, under the hypothesis that:

1. All the current measured after the GG are due to H^-, i.e. $I_{Acc} = I_{H^-}$.
2. The current lost in the accelerator is all carried by the co-extracted electrons dumped before the GG, i.e $I_{Extr} - I_{Acc} = I_e$.

by dividing the second relation by I_{H^-} we find:

$$\frac{I_{Extr}}{I_{Acc}} - 1 = \frac{I_e}{I_{H^-}} = R_j \tag{6.4}$$

so that:

$$\begin{aligned} I_{H^-} &= I_{Acc} \\ I_e &= I_{Acc} \cdot R_j \end{aligned} \tag{6.5}$$

relating the experimental measures of current in the power supply with the ion and electrons extracted currents. Notice that the validity of the first hypothesis can be estimated from earlier EAMCC analysis of the transmitted particles after GG, showing a H^- fraction corresponding to about 90% of beam composition; For more reliable estimation the procedure mentioned above and reported in [107] is needed, considering the current of all secondaries, but in this case the independence from the EAMCC code was preferred. Figure 6.6 reports some sample negative ion beam trajectory from both codes. In the case of Bypo also the electron trajectories are reported. The beam perveance defines a relationship between the beam current and voltage of a charged particle beam, according to the equation:

$$P = \frac{I}{V^{3/2}} \tag{6.6}$$

with I representing the beam current and V the total beam voltage, corresponding to $V = V_{extr} + V_{acc}$. The goal of the experiment is to perform a scan of different values of the perveance and to evaluate the consequent effect on the beam, whose shape is monitored by using the intermediate calorimeter, placed about 9 m downhill of the GG, to intercept it. The calorimeter is equipped with a crossed array of electrically insulated thermocouples, giving the possibility to evaluate the horizontal and vertical full width at half maximum (FWHM) of the beam. For our experiment only the horizontal FWHM was considered, and the perveance was varied by acting on the acceleration voltage, since the beam optics is too sensitive to variations in the extraction voltage, and the risk to cause damages on the structures by fairly small variation of this parameter is too large to be tolerated.

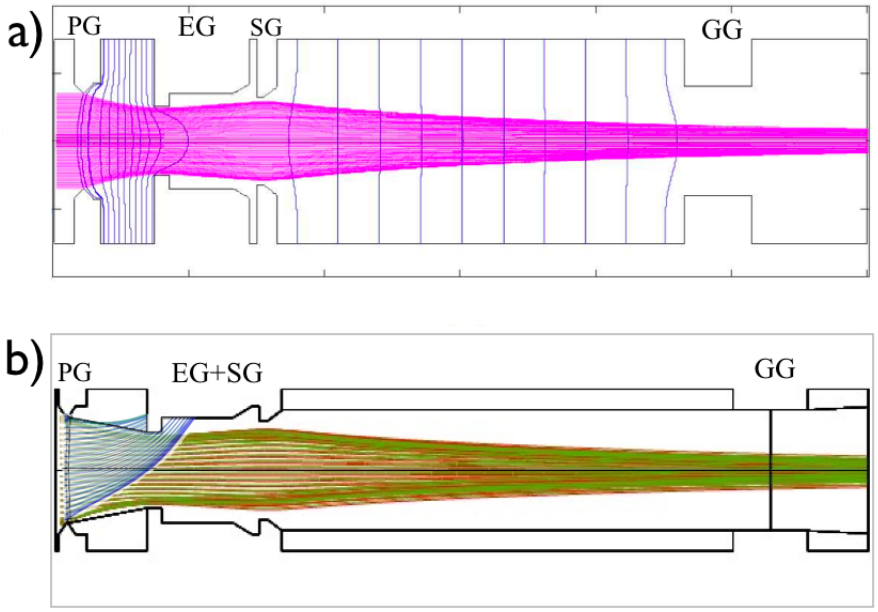

Figure 6.6: Some sample particles trajectories for the LHD simulation, obtained by means of SLACCAD code(a) and Bypo Code(b). In the case of Bypo also the electrons trajectories are reported, in blue. The different tonalities correspond to different starting angles of the emitted particles.

The acceleration voltage was varied in the range 137 to 178 kV, and a total of about 40 beam shots were measured on the calorimeter and the corresponding data recorded. For values greater than 178 kV the breakdown frequency was too high and the shots were interrupted. The data of measured FWHM exhibit a minimum in correspondence to the voltage value of 165 kV, corresponding to the smallest width of the beam, and a kind of relation of this point with the minimum divergence point for single beamlet numerical analysis is expected. It is important to note, in fact, that the experimental measures on the beam optics quality are performed for the whole beam, including 1540 beamlets coming form 2 sources, while the codes use single beamlet optics; for this reason it was not expected to met the same result about beam optics data of single beamlet and whole beam, but only a kind of correlation between them was searched.

The divergence values obtained by varying the acceleration voltage was measured by means of the RMS angle value, defined in 5.1 as the the root mean value of the average divergence angle of single macro-particles. The results for this kind of analysis are summarized in figure 6.7, including the RMS

angle data from both codes and the horizontal FWHM of the beam of one source. The values are normalized to the minimum of the relative data set for graph readability and the acceleration voltage was used instead of the beam perveance directly, to highlight the position of the minima point with respect to the voltage. As it is evident the experimental results are not in agreement

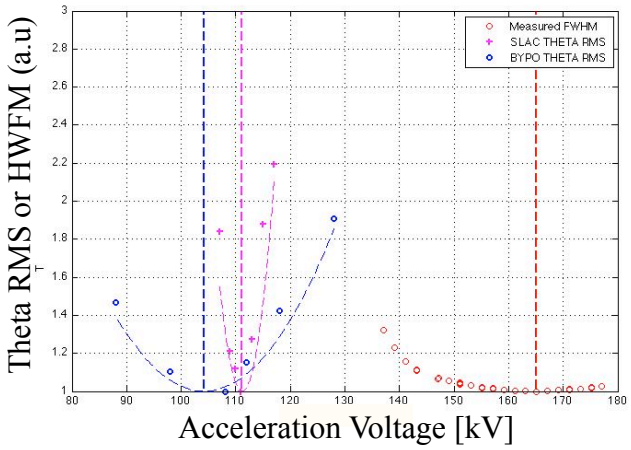

Figure 6.7: Summary of the benchmark between the experimental measures of BL2 of LHD and the numerical codes Bypo and SLACCAD. RMS and HWFM values are normalized to their minima.

with the numerical ones, meaning that the experimental point which minimizes the full beam transversal profile does not correspond to the minimum divergence angle found with the codes. On the contrary, a reasonable agreement is found between the two codes, taking into account the huge difference between them, first of all in the symmetries of the models (SLACCAD is 2D axial-symmetric, Bypo 2D cartesian). The discrepancies with experimental data can be explained in terms of 2 main reasons. The most important is the superposition of multi-beamlets effects, which the codes can not account for, like the beamlet-beamlet repulsion, the merging effect, and the grid offsets. A second point is represented by the 2D nature of the codes, which can be source of errors or uncertainty, for instance in terms of field calculations or in neglecting the effects of beam aiming, with respect to the real 3D accelerator. Anyway, as stated in the introduction, this analysis was preliminary, and it is evident that further studies are needed, probably involving detailed 3D and multi-beamlet simulations to better highlight a relationship between the single beamlet best optics numerical results and the experimental smallest pattern of the full beam on the calorimeter. The OPERA code, set up with

the support of Bypo or SLACCAD could be a good choice for this kind of studies.

Chapter 7

Conclusions and Future Work

This thesis presents several aspects of the issues related to the extraction and acceleration of negative ions in the context of neutral beam injection for fusion machines. In the present status of activities leading to the ITER neutral beam test facility PRIMA, the design and optimization of the features of the facility required massive use of modeling tools and for this reason most of the material presented in this thesis describes models used to deal with the physical and engineering aspects of those devices, explaining the basic theory and discussing the most important result of the codes.
The modeling has required the development of some specific tools, as it is the case of the database mentioned in section 2.3 and partially reported in C. It constitutes a common reference for the modeling of the whole injector, and helped in having more reliable data on atomic and molecular cross sections, in some cases also by completing the missing data, for instance where the energy range was unsatisfactory.
In some cases, where the interpretation of the physics underlying a particular process appeared particularly controversial or where existing theoretical and numerical tools were not sufficient to give accurate predictions of the phenomena, specific models were developed. This is the case of the code Bypo, whose exhaustive description is given in section 3.4. The development and exploitation of this code was performed during a large fraction of these 3 years doctorate period, and the Bypo code is being continuously improved, including more and more detailed effects; this gives an idea of the efforts toward the understanding and modeling of beam formation and optics. For a complete validation of Bypo and other codes, the first important test bed will be the *NIO1* project, a test facility which is under construction at Consorzio RFX [108],[109]. Some preliminary benchmarks with the code SLACCAD showed a reasonable agreement between them, despite the different geometries.

For other kinds of studies the existing numerical models and codes seemed sufficiently reliable, and in this case some work was necessary to acquire general knowledge on their usage in order to perform some adaptations, to improve the capability of the codes to catch realistic traits of the cases of interest . This was accomplished, for instance, for the SLACCAD and for the EAMCC codes with the creation of the BACKSCAT tool. The knowledge of this large set of modeling tools allowed to complete the designing and optimization phase of SPIDER and are expected to play a fundamental role in the design of MITICA as well.

Regarding the benchmark with the experiments, whose description was given in section 6, some interesting results were found, suggesting the underestimation of some effects in the modeling of thermal loads on structures. The EAMCC results, in fact, gave smaller values of power fluxes on the grounded grid with respect to the measured ones. Different hypotheses were suggested to explain those discrepancy in data, calling for a better understanding of the role played by the beam halo, and for more accurate estimation of the distribution of the gas pressure inside the accelerator. This last issue, in particular, had already emerged as an important topic also in the analysis of the SPIDER and MITICA accelerator, where a strong lateral pumping is present due to large gaps between grids directly connected to the vacuum tank. This aspect can lead to lack of homogeneity between beamlets, and requires further investigations, maybe by developing dedicated 3D Monte Carlo codes for the pressure distribution determination.

From the point of view of the optics benchmark reported in 6.3, further analyses are needed using 3D and multi beamlet analysis codes, since the 2D codes employed in the present studies are unable to catch all the information of beam optics. The OPERA code should be a good alternative for this kind of studies.

The collaboration with the Japanese laboratories will continue: the possibility of using the RFX suite of codes on the injector of the NIFS test bed, rather than on a beamline directly installed on a fusion device. This will allow to have more flexibility in the benchmark between models and experiment, but requires some strong modification in the present state of codes, to account for the particular geometry adopted in the test bed (as in other beamlines of LHD as well). The problem arises from the particular shape of the grounded grid, which is multi-slotted instead of multi-rounded, breaking the cylindrical symmetry of codes like SLACCAD. Since also the EAMCC code used for the power load estimate is based on the geometry the potential of SLACCAD, a possibility could be to modify EAMCC in order to work with a potential calculated in the OPERA environment, where there are no restrictions on the grid shape.

Another topic which deserves further efforts regards the space charge compensation reported in section 4.1.2. The results reported there suggest the novel idea of axial dynamics for the expulsion of particles sustaining the space charge neutralization, together with the classical radial dynamics. Some upgrades of the numerical codes can be useful to work with smaller time steps or to investigate the phenomenon for longer times and with a better spatial resolution, meaning more particles and smaller cell size for each simulation. An interesting possibility in this direction could be represented by the implicit "particle in cell" methods [110] already used in the NBI context for the simulation of the plasma source [111].
In conclusion, an important contribution to the understanding and developing of neutral beam injectors physics was given, covering in particular the problems of beam formation in the source and its successive acceleration. At the same time the knowledge acquired in specific numerical methods and techniques allowed to expand the contribution toward other aspect of the injector, as the calorimeter or the electron dump, whose design for the SPIDER device was completed.

Appendices

These appendices are intended to complete the thesis with the description of further models and studies still related to NBI modeling. Since they are not directly connected with the main topic of extraction or acceleration or since they only represents the deepening of some arguments already treated, I preferred to collect them in an an appendix, rather then in a dedicated chapter of the thesis.
Contribution of the author to the design of the instrumented Calorimeter for SPIDER are described in appendix B, whereas the list of the expected reactions of interest in NBI physics, supporting the section 2.3, are reported in appendix C.
Some originally developed work is presented in appendix A, describing some studies about the high voltage holding modeling which is a very important issue for NBIs and accelerators in general, defining the breakdown frequency, recognized as a key factor in terms of pulse duration and failure of the injector. The inclusion of this dedicated appendix complete the description of the efforts of RFX in the context of accelerator modeling.

Appendix A

High Voltage Holding Modeling

The holding of voltages > 100 kV (high voltage regime, HV) has a reputation for being a subject of difficult predictability and repeatability. Phenomena of micro-discharges between the electrodes of high voltage accelerating tubes are common, but their physical aspects are not yet fully understood [112],[113]. The complexities are due to the fact that the large variety of accelerator applications leads to different electrode conditions, being the accelerator itself made from several parts, or to uncertainties of surface preparation. Other phenomena are more clearly related to multiphysics modeling, as the fact that a current leakage may heat an electrode (which is a positive feedback, leading to a spark) or may clean the electrode, which reduces emission and is a negative feedback, leading to a short transient discharge. Even if HV systems are designed not to exceed by a good safety margin a given surface field over which field emission is possible, there are at least three known mechanisms for the onset of discharge in vacuum, discussed in the literature [114] and relevant here:

1. Isolator surface discharge occurring, for instance when an electron strikes an insulator, producing on average δ secondary electrons; when $\delta > 1$, the insulator surface charges up and design fields are altered locally, with possible discharge (also in relation to adsorbed gas or imperfection in the isolator or in its junction to the electrode); A possible remedy can consist in modifying the design, to obtain a lower field near the junction;

2. Emission of micro particles: if V_1 is the anode to cathode voltage and d their distance a micro particle detaching from the anode will get a positive charge ($\propto V_1/d$) by induction and will impinge on the cathode with an energy ($\propto V_1^2/d$), which may be sufficient to locally melt the electrode and to trigger a discharge; otherwise the micro particle

may bounce, getting a negative charge by induction (and repeat the process); By postulating a micro particle emission, Cranberg [112] was able to predict a $V_1 \propto \sqrt{d}$ trend.

3. Microdischarges by regenerative ion emission: an H^+ ion emitted from the anode impinges on the cathode, extracting negative particles, including an average number μ_- of H^- from hydrogen or pump oil absorbed on the cathode); in turn each H^- accelerated against the anode extracts an average number μ_+ of H^+ ions. According to [113], when $\mu = \mu_-\mu_+ > 1$ current rises until absorbed contaminants decrease, so that μ become less than 1 and discharge decreases; further studies assuming parallel electrodes and an emitted particle velocity distribution [115] conclude that the discharge spreads over these electrodes and thus weakens.

A.1 Cascades of Secondary Particles in High Voltage Accelerators

The work here reported is based on the third hypothesis of the introduction above, guessing micro-discharge phenomena be driven by regenerative ion emission. In this context a model for high voltage test is studied, with the aim of understanding the reasons for failures of voltage holding which are not covered by conventional and local design criteria. A first understanding of the problem is obtained by solving the electrostatic potential in a 2D axisymmetric geometry with Comsol Multiphysics [74]; the detail of the electrode shapes is taken into account and a cascade of particles between opposite electrodes is generated: the impact of an ion (say an H^+) with an electrode extracts particles of the opposite charge (say electrons or H^-) which are in turn accelerated in the opposite direction. Due to the high voltages involved, electrons are treated relativistically. Very specific attractors were found for the impact points; physical reason is that the highly non uniform electric field may focus, defocus or move the discharge.

A.1.1 Model description and implementation

The model uses a 2D geometry axially symmetric aroud the z axis, and the geometry used to test it reported in figure A.1, consisting in a Cockroft-Walton type accelerator. This geometry is similar to the ones used in some voltage tests of ion sources, considered for Neutral Beam Injectors (NBI) in fusion devices, in the 800 kV to 1 MV range [116],[117]. Let $r\theta z$ be a system of

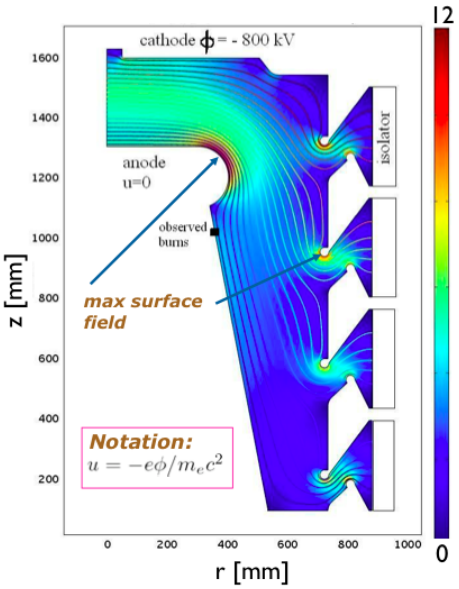

Figure A.1: Simulation geometry, with a surface plot of electric field and equipotentials. Note the black spot indicating the position of a melting point experimentally found.

cylindrical coordinates. The electric potential ϕ is obtained by means of the standard Poisson solver of Comsol; note that potential energies and electron rest energies $m_e c^2$ are comparable, so that the scaled potential is defined as $u = -e\phi/m_e c^2$. Here a trajectory of particles consist in a motion from one electrode to another, while an orbit is defined as a connected sequence of trajectories starting from the anode until the first time that it returns back to the anode or until it escapes from the system or it reaches an isolator. Since there are several cathodes (at different voltages), at any electrode the emitted particle charge sign is assumed equal to the sign of $u_{,n}$ where n is the inward normal (for later consistency) and the notation $x_{,k}$ denotes the partial derivative of x with respect ot k. At isolators, tracking is stopped. Mass of negative and positive particles is assigned by the user. For the relativistic equation of motion the expression for the force $F = md_t(\gamma v)$ with m the particle rest mass becomes (by expanding the derivatives):

$$\mathbf{F}/m = \gamma[\mathbf{a} + \gamma^2\beta(\beta \cdot \mathbf{a})] \tag{A.1}$$

Solving A.1 for the acceleration $\mathbf{a}$ yields:

$$\mathbf{a} = \gamma^{-1}[(\mathbf{F}/m) - \beta(\beta \cdot \mathbf{F}/m)] \tag{A.2}$$

and, in cylindrical coordinates:

$$\mathbf{a} = \hat{r}(\ddot{r} - r\dot{\theta}^2) + \hat{\theta}(r\ddot{\theta} + 2\dot{r}\dot{\theta}) + \hat{z}\ddot{z} \tag{A.3}$$

with $\hat{r}$, $\hat{\theta}$ and $\hat{z}$ denoting the r, θ and z direction respectively. Thus, the equation without the magnetic field is:

$$\mathbf{F}/m = 1e\mathbf{E}/m = i(m_e/m)c^2\nabla u \tag{A.4}$$

Substituting equations A.2, A.3 and A.4 and using the convenient scaled time s as $s = ct(m_e/m)^{1/2}$ we get the relativistic motion equation in cylindrical coordinates as:

$$\hat{r}(r_{,ss} - r\theta^2{}_{,s}) + \hat{\theta}(r\theta_{,ss} + 2r_{,s}\,\theta_{,s}) + \hat{z}r_{,ss} = i[\nabla u - (m_e/m)\mathbf{x}_{,s}\,w]/\gamma \tag{A.5}$$

with $w = r_{,s}\,u_{,r} + z_{,s}\,u_{,z} + (\theta_{,s}\,u, \theta/r^2)$;. This form is numerically convenient for both electrons and protons. Assuming now azimuthal symmetry of u and no magnetic field, we have that $L_1 = \gamma r^2\theta_{,s}$ is constant on a trajectory, so that trajectory equations simplify to

$$\begin{aligned} r_{,ss} &= \frac{L_1^2}{\gamma^2 r^3} + \frac{i}{\gamma}\Big[u_{,r} - \frac{m_e}{m}r_{,s}\,w\Big] \\ z_{,ss} &= \frac{i}{\gamma}\Big[u_{,z} - \frac{m_e}{m}z_{,s}\,w\Big] \end{aligned} \tag{A.6}$$

notice that $\gamma = \gamma_1 - i(u_1 - u)(m_e/m)$, with u_1 and γ_1 the initial values.
A first simple iteration model, consists in assuming that particles are emitted with zero speed, so at each impact (or iteration), one trajectory stops and another starts. A plot of this kind of orbits is reported in picture A.2 Note that all particles rapidly acquire a velocity perpendicular to the electrode since this is the E direction; moreover in this case $L_1 = 0$ and θ is thus constant. In some cases, the orbit bounces between cathodes for some iterations before resuming the usual anode-cathode cycle of bouncing, as seen in A.2, with two consecutive proton emissions. Also many starting positions can be traced at the same time, so that the distance of two particles can be monitored. This kind of simulations shows the existence of some accumulation points, corresponding to the attractors of the problem, where the orbit start point coincides with the orbit end point, so that the same orbit is always repeated. In the particular geometry studied, different attractors can be found, in correspondence with the different intermediate electrodes, as shown in Fig A.3; each one influences the motion of particle emitted in the neighboring positions. Moreover the upper intermediate electrode has a stronger attractor, since it has a higher energy and a better position, allowing

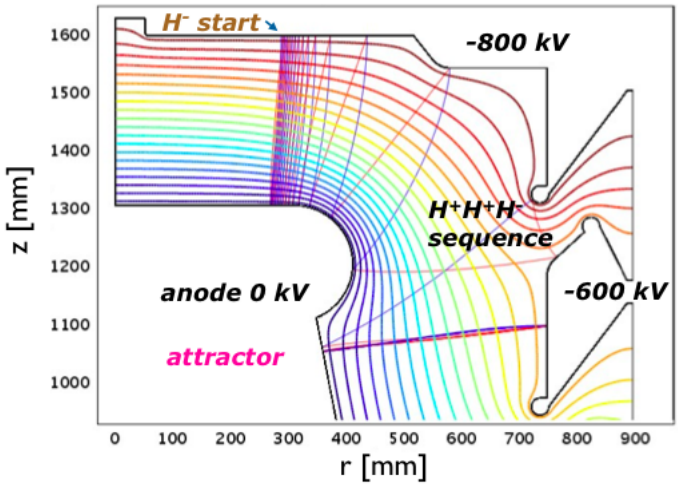

Figure A.2: A cascade of H^+ and H^- for 40 iterations; starting position was tuned until two consecutive proton emission was observed.

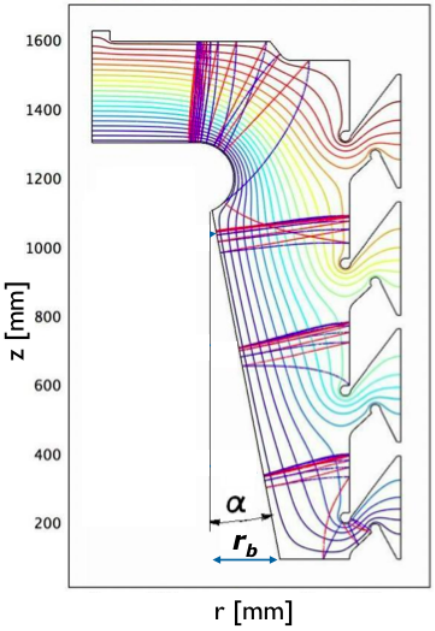

Figure A.3: Cascade of particles consisting of 35 iterations, with 3 different starting position for the first emission.Three attractors are found. Note the α angle used for geometry variations.

it to collect cascades of trajectories originating from most of the upper region. Other simulations were performed setting the normal emitted velocity to a nonzero value, introducing the free parameters K, that is the fraction of the parent particle speed which is transmitted to the emitted particle velocity. Variations in K only result in a little displacement of the attractor position, which seems to holds all its properties, up to values of $|K| < 0.5$. Since values over this high limit seem to be unphysical, the conclusion is that attractors always exists, in 2D analysis. With the purpose of studying the effects of attractors on different geometries, further analyses were performed. In particular the tapering angle α (the semi aperture of the conical support of the anode electrode, as defined in figure A.3) was changed; since the top part of the anode was kept unchanged, the radius of base of the conical support r_b changes with α. The main effect of such variation is again a displacement of the attractor position, which however maintains all its properties even in the $\alpha = 0$ case (cylindrical anode support). Moreover when $\alpha = 191$ mrad to make our geometry similar to the real NBI device mentioned in the introduction [117], the attractors position fits well the melting points found experimentally. This confirms the capability of cascade attractors to predict the electrodes damages caused by micro discharges. This analysis was also enriched by moving in the 3D domain, and challenging the problem by means of statistical methods and setting up a Fokker-Plank equation. The results of this kind of studies are reported in [118].

A.2 Voltage Holding Predictions in Multi Electrode Systems.

Another exemplum of HV modeling at RFX is represented by the probabilistic model for the predictions of the breakdown probability in complex systems, described in [119]. Since the author of this work was only involved in the numerical implementation, only a short description on the model will be given in this section, remanding to the published work for further details. The model is based on the implementation of the micro particle (clump) induced breakdown Cranberg-Slivkov theory [120] into a statistical approach. The clump mechanism, based on the existence of electrically charged microparticles leaving one electrode and clashing to the electrode with opposite polarity with sufficient energy to vaporize, underlies the presence on the electrode surface of a micro-particle surface density N $[m^{-2}]$ which can provoke the voltage breakdown if the electric field at the receiving electrode is sufficient to initiate a Paschen discharge across the vapor bubble. The problem

is challenged with a probabilistic approach, exploiting the basic assumption that the N number of micro-particles that potentially can produce breakdown, from which the breakdown voltage can be obtained, is an increasing function of the W parameter, representing the energy transferred by the electric potential to a micro particle. For simple geometries the evaluation of W can be determined analytically (parallel plane or coaxial geometries), but for multielectrode-multipotential systems as in the case of the accelerator of the MITICA experiment, the voltage difference and the anodic electric field experienced by a clump are determined only by calculating its trajectory. Some routine in Comsol environment were implemented, exploiting a couple of Runge-Kutta integration using the potential calculation of the internal Poisson solver of Comsol, to obtain the particles trajectories. The routines were written in a way to allow great flexibility in the electrodes shape, whose surface is divided in an arbitrarily great number of subregion, each of them used as starting position for the trajectory. The Result of the model were compered with some experimental results found in literature showing good agreement. The breakdown voltage evaluation in terms of probability makes this model suitable for an engineering approach to the insulation design and the model showed to behave correctly even in the case of complex electrode geometries.

Appendix B

Design of the STRIKE Calorimeter

The main goal of the SPIDER source is to improve the beam characteristics for a low current acceleration stage, since most of the full beam features depend on the ion source performances. In particular, the most important ITER NBI requirements to be fulfilled regard the beam uniformity, whose value has to remain within ±10%, and the beam divergence, to be kept below 7 mrad. The diagnostic calorimeters are probably the most important instrument dedicated to measure these quantities. Most of the existing calorimeters used in NBI systems are constituted by simple surfaces with a clever machining and a suitable arrangement of thermocouples so as to provide some local measurements of the energy flux and beam shape, as the one used in the case of the measures on LHD beams, reported in section 6.3. The instrumented Calorimeter STRIKE (Short-Time Retractable Instrumented Kalorimeter Experiment) [121] designed for the SPIDER source, belongs to a most advanced family of devices of this kind, also featuring thermal cameras monitoring the calorimeter plates, and current sensors. The thermocouples are anyway present for absolute calibration of cameras. In order to reproduce the geometry of the SPIDER beam, which is made of 4x4 groups of 80 beamlets each, STRIKE is divided into 16 tiles directly exposed to the beam. In the design phase of this complementary device, several numerical analyses were performed, and a summary is given in the following.

B.1 Beam Divergence and Uniformity

Both the analysis of beam uniformity and divergence were made by means of finite element methods, mostly performed in the Comsol environment [74].

Since the beamlet divergence estimation requires two measurements of the beamlet width in different positions along the beam, STRIKE has the possibility to be shifted and to intercept the beam at different position. The simulations were made by solving the classic heat transfer equation

$$\nabla \cdot \big(k(T)\nabla T\big) = \sigma_{SB} T^4 \tag{B.1}$$

also including the radiation term, with k representing the material conductivity, T the temperature and σ_{SB} is the Stefan-Boltzmann constant ($\sigma_{SB} = 5.67 \cdot 10^{-}8[W/(m^2K^4)]$). In the case of STRIKE the cameras scan the rear part of the tiles, since the observation of the front is perturbed by the high level of radiation expected due to beam-gas interaction. This characteristic requires the use of particulars materials for the tile composition, having anisotropic properties, to allow having a good resolution in the backside footprints of the beamlets. In particular high value of thermal conductivity in the beam direction is required, while the transversal should be small, to preserve the resolution. After several tests the MCF-1A carbon fibre composite (CFC) was selected as the best candidate material. Its characteristics are reported in figure B.1 a) together with a surface plot of the rear part of a simulated sample tiles, showing a good beamlet resolution.

The incident power of the beam was represented by imposing a Neumann

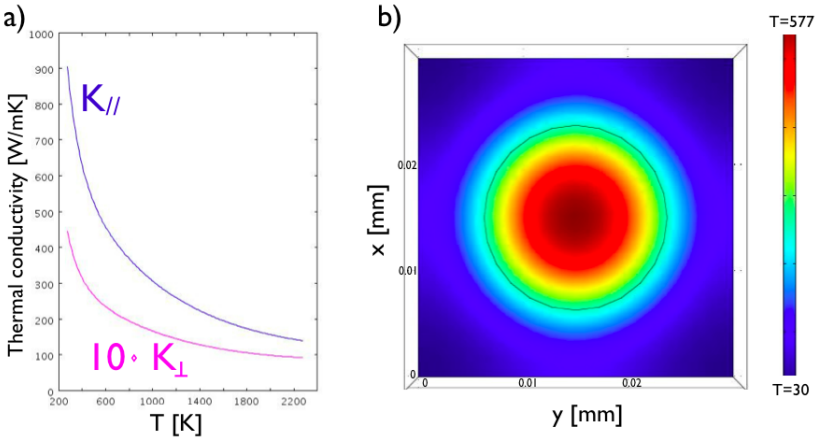

Figure B.1: Thermal analysis of the MFC-1A CFC target. In a) the target characteristics: $K_{//}$ = parallel conductivity, $K_{\perp}$ =perpendicular conductivities. In b) the temperature surface plot of rear part of the tile.

condition on the front part of the 3D domain of the numerical simulation, as:

$$n \cdot \big(k(T)\nabla T\big) = P_0(x, y) \tag{B.2}$$

where n is the outward normal and P_0 the beamlet power density profile. For P_0 there are 2 choices: import power load deposition data from other codes (i.e. EAMCC [78]) or use an analytic expression. In the examples here reported P_0 was set up to reproduce a multi-gaussian shape, as expected for the full beam profiles, anyway, thanks to the intrinsic symmetries, it is sufficient to simulate only one fourth of the whole tile. Moreover, in order to account for the effect of a beamlet divergence, the gaussian profile is modified, according to

$$P_0(x,y) = A_g \exp\Big[- \frac{(x-x_0)^2}{2\sigma_x^2} - \frac{(x-x_0)^2}{2\sigma_y^2} \Big] \tag{B.3}$$

where σ_x and σ_y are respectively the beamlet half-widths in the x and y directions, also containing the divergence correction as $\sigma_{x,y} = \sigma_{0x,y} + \delta z$ expressing the angular aperture of the beamlet as a function of the distance along z from the GG. A_g is the amplitude of the energy flux at the maximum position (x_0, y_0). Since the thermal pattern on STRIKE tiles are modified by the divergence variation, using different values of the divergence in P_0, different beam profiles are obtained on the target rear side, as reported in figure B.2. With a least mean square fit the results were processed in order to reconstruct the variation on the average width of the beamlet for values of P_0 corresponding to different positions of the calorimeter. The values of divergence reconstructed with these measures match the divergence imposed in the beam profile, showing the good diagnostic capability of STRIKE in case of divergence measurements. For the beam uniformity the result were positive as well, reporting variation in temperature of about 10 K for flux changes of 1%, marginally feasible with real thermal cameras, which have an error of 1-2%.

B.2 Current measures

Measuring the currents hitting the electrically insulated tiles of the calorimeter will be helpful in aiding the interpretation of experimental results and the benchmarking with numerical codes (for instance simultaneous measurements of current and deposited power provide a way to estimate the stripping losses inside the injector, under the assumption that stripped electrons are dumped before the calorimeter; see section 6.3). When the beam collides on the calorimeters surface, a strong secondary emission occurs (using the available data for secondary electrons emission in the case of graphite surface it is estimated that more than one negative charge will be emitted per incident particle), calling for a biasing of the tiles in order to push the electron back

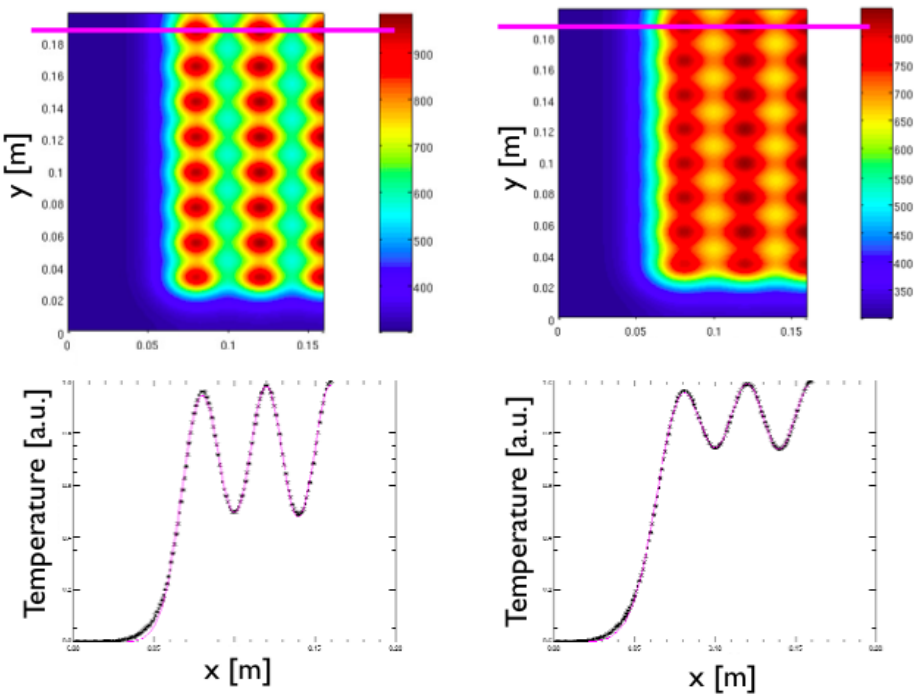

Figure B.2: Simulation of measurements performed at different distances from the GG: 0.5 m from the GG (left) and 1 m from the GG (right); thermal pattern on the rear side (top) and temperature profile along the line shown (bottom); the best fitting curve is superposed to the temperature profile.

toward it. Even if this phenomena do not affect the thermal measurements, since the ion/atom energy is anyway deposited inside the crystalline lattice also if electron emission occurs, it can be source of noise in the current measures, since electrons can be back-pushed in a tile which is different from the one form which they were emitted. Some finite elements analyses where performed in the same Comsol environment, in order to define the bias potential needed to contain the electron emission and do not affect the measurements. A 2D simulation featured the potential distribution as a result of the Laplace equation and estimated the electron motion. The electron trajectories were started with 1 to 3 eV emission energy, according to [94] and for that value a potential of $\Phi_{Bias} = 200$ V was sufficient to obtain that all secondary electrons should return to the tile they were emitted from. More details on this kind of simulation can be found in [122].

Appendix C

Atomic and Molecular Database

This appendix will include the last updated version of the atomic and molecular database of reaction which can happen in a H_2 or D_2 negative ion source or in the interaction of the corresponding beam with the background gas. The motivations for the constitution of this kind of database arose during the CCNB Workshop on NBI modeling, held in Padova in March 2009, with the idea of assembling a reference common tool to uniform the NBI oriented modeling, and to join the data coming from different laboratories. At the present state the list includes more than two hundred reactions, and the number, considering the internal excitation of molecules, increases to more than one thousand. The database here reported includes all the reactions expected, but the cross section data are only available for few of them, identified by quoting the reference in the relative space, highlighting the further steps required to complete it. The database was released with some remarks reported in the following:

- The list is based on Hydrogen. Extension to Deuterium is foreseen in a second step.
- Surface processes are not yet included.
- At this level reactions whose cross section is expected to be negligible are also included.
- Collisions between two particles are considered: the first is the projectile, the second is the target. Target particle is assumed to be at rest, and the whole energy comes from the projectile. Where the center of mass (C.M.) reference frame is used it is explicitly noted.

- The excited states of projectiles and target are not considered for all cases. Where it happens the symbol X^* denotes the excited state of the X atom or molecule. The specification on the quantic state is generally included in brackets.

Electron Collisions					
N	Reactants	Products	Range (eV)	Reference	Remarks
1.	$e + H^+$	H	1.0e-1 - 1.5e3	[21]	
2.		$H^*(2s)$	1.0e-1 - 1.5e3	[21]	
3.		$H^*(2p)$	1.0e-1 - 2.0e2	[21]	
4.		$H^*(n' = 3)$	1.0e-1 - 1.8e2	[21]	
5.		$H^*(n' = 4)$	1.0e-1 - 1.5e2	[21]	
6.		$e + H^+$			
7.	$e + H$	$e + H^*(2s)$	1.5 -2.0e4	[21]	
8.		$e + H^*(2p)$	1.5 - 2.0e4	[21]	
9.		$e + H^*(n' = 3)$	2.0 - 2.0e4	[21]	
10.		$e + H^*(n' > 3)$			
11.		$e + H^+ + e$	1.36e1 - 2.0e4	[123]	
12.		H^-			
13.	$e + H^*(2s)$	$e + H^*(2p)$	1.0e-1 - 2.0e4	[21]	
14.	$e + H^*(n = 2)$	$e + H^*(n' = 3)$	1.7e-1 - 2.0e4	[21]	
15.	$e + H^*(n = 2)$	$e + H^+ + e$	3.4 - 2.0e4	[123]	
16.	$e + H^*(n = 3)$	$e + H^+ + e$	1.51 - 2.0e4	[123]	
17.	$e + H^*(n)$	$e + H^*(n')$			
18.	$e + H^-$	$e + H + e$	9.06e-1 - 2.0e4	[21]	a)
19.		$e + H^+ + e + e$	1.66e1 - 2.0e4	[21]	
20.		$e + H^-$			
21.		$e + e + H^*$			
22.	$e + H_2^+(\nu)$	H_2			
23.		$H + H$			
24.		$H^* + H$			
25.		H_2^*			
26.		$e + H^+ + e + H^+$	1.79e1 -2.0e4	[21]	b)
27.		$e + H^+ + H$	2.70 - 2.0e4	[21]	b)
28.		$e + H^+ + H^*(n = 2)$	1.4 - 1.0e4	[21]	b)
29.		$e + H_2^+$			

Note:
a) H^- has only one bound state [124].
b) Average ΔE ($\simeq 0.4$) for each H^+ is obtained from the averaged vibrational energy of H_2^+ ($\nu = 0 - 9$) (which approximately coincides with that for the state $\bar{\nu} \simeq \nu = 3$) and then averaged over the Frank-Condon region.

Electron Collisions					
N	Reactants	Products	Range (eV)	Reference	Remarks
30.	$e + H_2$	$e + H_2^*(B^1\Sigma_u^+ 2\text{p } \sigma)$	1.1e1 - 2.0e4	[21]	
31.		$e + H_2^*(C^1\Pi_u 2\text{p } \pi)$	1.5e1 - 2.0e4	[21]	
32.		$e + H_2^*(E, F^1\Sigma_g^+)$	1.6e1 - 2.0e4	[21]	
33.		$e + H_2^+(\nu) + e$	1.8e1 - 2.0e4	[21]	c)
34.		$e + H + H^+ + e$	2.0e1 - 6.0e3	[21]	
35.		$e + H^+ + H^+ + e$			
36.		$e + H_2(\nu)$		[21]	
37.		$(H_2^-)^* \rightarrow H + H^-$	1.0e-1 - 5.0	[21]	
38.		$(H_2^-)^* \rightarrow H^* + H^-$			
39.		$e + H + H$	1.0e1 - 1.2e2	[21]	
40.		$e + H + H^*(2s)$	1.6e1 - 2.0e4	[21]	
41.		$e + H + H^*(n = 3)$	1.9e1 - 3.0e3	[21]	
42.		$e + H^*(2s) + H^*(2p)$	2.9e1 - 4.5e3	[21]	
43.	$e + H_2(\nu)$	$e + H_2(\nu')$			
44.	$e + H_2(\nu = 0)$	$e + H_2(\nu' = 1)$	8.0e-1 - 2.0e2	[21]	
45.	$e + H_2(\nu = 0)$	$e + H_2(\nu' = 2)$	1.5 - 4.0e2	[21]	
46.	$e + H_3^+$	H_3			
47.		$H + H_2$			
48.		$H^* + H_2$			
49.		$e + H_3^+$			
50.		$e + H_2 + H^+$			
51.		$e + H_2^+ + H$			
52.		$e + H^+ + H + H$	1.6e1 -2.0e4	[21]	
53.		$e + H^+ + H + H^*$			
54.		$e + H^+ + H^* + H^*$			
55.		$H + H + H$	1.0e-1 - 1.6e4	[21]	
56.		$H^+ + H^+ + e + e + H$			
57.		$H^+ + H^+ + H^+ + e + e + e$			

Note:
c) The distribution of $H_2^+(\nu)$ over the vibrational quantum number is known [125]

H^+ Collisions					
N	Reactants	Products	Range (eV)	Reference	Remarks
58.	$H^+ + H$	$H + H^+$	1.2e-1 - 6.3e5	[23]	
59.		$H^*(2p) + H^+$	1.9e1 - 2.0e4	[21]	
60.		$H^+ + H^*(2s)$	5.0e3 - 2.5e4	[23]	
			2.0e2 - 2.0e4	[123]	
61.		$H^+ + H^*(2p)$	6.0e2 - 2.4e5	[23]	
			1.9e1 - 2.0e4	[123]	
62.		$H^+ + H^+ + e$	9.4e3 - 1.5e6	[123]	
63.		H_2^+			
64.	$H^+ + H(n)$	$H^+ + H^*(n')$	1.2e-1 - 6.3e5	[23]	n =1-10 n'=1-10
65.	$H^+ + H^-$	$H^+ + H^-$			
66.		$H^- + H^+$	5.9e1 - 1.1e2	[23]	
67.		$H^+ + e + H$	2.8e3 - 7e4	[23]	
68.		$H^+ + e + H^*$			
69.		$H^+ + e + H^+ + e$			
70.		$H + H$	2.0e-1 - 4.8e3	[23]	
71.		$H + H^*$(n=2)	0.1 - 2.0e4	[21]	
72.		$H + H^*$(n=3)	0.1 - 2.0e4	[21]	
73.		$H_2^+ + e$	2e-3 - 7	[23]	
74.		H_2			
75.	$H^+ + H_2^+$	$H^+ + H_2^+$			
76.		$H^+ + H_2^{+*}$			
77.		$H^+ + H + H^+$	1.9e1 - 2.0e4	[21]	
78.		$H^+ + H^* + H^+$			
79.		$H^+ + H^+ + e + H^+$			
80.	$H^+ + H_2^+(\nu)$	$H^+ + H_2^+$ (ν')			
81.	$H^+ + H_2$	$H^+ + H_2$ (ν')			
82.		$H + H_2^+$	2.72 - 2.0e4	[21]	
83.		$H^* + H_2^+$			
84.		$H^+ + H + H$			
85.		$H^+ + H + H^*(2s)$	5.0e3 - 1.0e6	[23]	
86.		$H^+ + H + H^*(2p)$	4.0e3 - 1.0e6	[23]	
87.		$H^+ + H + H^*(3p)$	1.5e4 - 3.0e4	[23]	
88.		$H^+ + H^+ + H + e$			
89.		$H^+ + H^+ + H^+ + e + e$	1.0e5 - 3.0e6	[23]	
90.		$H^- + H^+ + H^+$	2.0e2 - 1.0e6	[23]	
91.		$H^+ + H_2^+ + e$			
92.		H_3^+			

93.	$H^+ + H_2(\nu)$	$H^+ + H_2\ (\nu')$	∼1 - 9 C.M. Energy	[126]	$\nu = 1-14$ $\nu' = 1-18$
			∼1.5e1 - 1.0e2 C.M. Energy	[127]	$\nu = 1-14$ $\nu' = 1-18$
94.	$H^+ + H_2(\nu)$	$H + H_2^+\ (\nu')$	∼1 - 9 C.M. Energy	[126]	$\nu = 1-14$ $\nu' = 1-18$
			∼1.5e1 - 1.0e2 C.M. Energy	[127]	$\nu = 1-14$ $\nu' = 1-18$
95.	$H^+ + H_2(\nu)$	$H^+ + H + H$	∼1 - 9 C.M. Energy	[126]	$\nu = 1-14$
96.	$H^+ + H_3^+$	$H^+ + H_3^+$			
97.		$H^+ + H_2 + H^+$			
98.		$H^+ + H + H + H^+$			
99.		$H^+ + H^* + H + H^+$			
100.		$H^+ + H_2^+ + H$			
101.		$H^+ + H_2^+ + H^*$			

H Collisions					
N	Reactants	Products	Range (eV)	Reference	Remarks
102.	$H + H$	$H + H$	0.1 - 1.0e2	[128]	
103.			C.M. Energy		
104.		$H + H^*(2s)$	2.0e3 - 9.0e4	[23]	
105.		$H + H^*(2p)$	4.0e3 - 3.0e4	[23]	
106.		$H + H^*(3s)$	1.0e3 - 1.0e6	[23]	
107.		$H + H^*(3p)$	1.0e3 - 1.0e6	[23]	
108.		$H + H^*(3d)$	1.0e3 - 1.0e6	[23]	
109.		$H + H^+ + e$	1.2e3 - 3.5e6	[23]	
110.		$H_2\ (\nu)$			
111.		$H^+ + e + H^+ + e$			
112.		$H_2^+(\nu)$+e			
113.		$H^- + H^+$	2.0e3 - 7.3e3		
114.	$H + H_2$	$H + H_2$			
115.		$H^* + H_2$			
116.		$H^*(2s) + H_2$	2.0e3 - 2.5e4	[23]	
117.		$H^*(2p) + H_2$	5.0e3 - 2.5e4	[23]	
118.		$H^*(3s) + H_2$	2.0e2 - 5.0e5	[23]	
119.		$H^*(3p + 3d) + H_2$	2.0e2 - 1.0e5	[23]	
120.		$H^*(4s) + H_2$	2.0e2 - 2.5e3	[23]	
121.		$H^*(4s + 4p) + H_2$	6.0e1 - 2.5e3	[23]	
122.		$H + H + H$			
123.		$H + H + H^*(2s)$	5.0e3 - 2.5e4	[23]	
124.		$H + H + H^*(2p)$	5.0e3 - 2.5e4	[23]	
125.		$H^+ + e + H_2$	6.0e1 - 2.0e7	[23]	
126.		$H^+ + e + H_2\ (\nu')$			
127.		$H^+ + e + H + H$	5.0e3 - 5.0e4	[23]	d)
128.		$H^+ + e + H + H^*$			
129.		$H^+ + e + H^+ + e + H$	5.0e3 - 5.0e4	[23]	d)
130.		$H^+ + e + H^+ + e + H^*$			
131.		$H^+ + H^+ + H^+ + e + e + e$	5.7e3 - 5.2e4	[23]	
132.		$H + H_2^+ + e$	2.0e2 - 4.0e5	[23]	
133.		$H^* + H_2^+ + e$			
134.		$H^- + H_2^+$	4.0e1 - 4.6e5	[23]	
135.		$H^- + H^+ + H$	5.0e3 - 5.0e4	[23]	d)
136.		$H^- + H^+ + H^+ + e$	4.7e3 - 5.0e4	[23]	

Note:
d) Two possible channels : via $H_2(2\text{p}\ \Sigma_u)$ or via $H_2(1\text{s}\ \Sigma_g)$

H^- Collisions					
N	Reactants	Products	Range (eV)	Reference	Remarks
137.	$H^- + H$	$H + H + e$			
138.		$H + H^* + e$			
139.		$H + H^-$			
140.		$H^* + H^-$			
141.		$H^+ + H + e + e$			
142.		$H^+ + H^* + e + e$			
143.		$H^+ + H^+ + e + e + e$			
144.		$H^+ + H^- + e$			
145.		$(H_2^-)^* \rightarrow H_2 + e$			
146.		$(H_2^-)^* \rightarrow H + H^-$			
147.	$H^- + H_2^+$	$H^- + H_2^+(\nu')$			
148.		$H + H_2$			
149.		$H^* + H_2$			
150.		$H^- + H^+ + H$			
151.		$H + H + H$			
152.		$H + H^* + H$			
153.		$H + e + H_2^+$			
154.		$H^+ + H^+ + H + e + e$			
155.	$H^- + H_2$	$H^- + H_2(\nu')$			
156.		$H + e + H_2$	2.3 - 1.7e7	[23]	
157.		$H^* + e + H_2$			
158.		$H^+ + e + e + H_2$	1.0e3 - 1.0e7	[23]	
159.		$H + H_2^- \rightarrow H + H + H^-$			
160.		$H + H_2^- \rightarrow H^* + H + H^-$			
161.		$H + H + H + e$			
162.		$H + H + H^* + e$			
163.		$H^- + H_2^+ + e$			
164.		$H + e + H_2^+ + e$			
165.		$H^+ + e + e + H_2^+ + e$			
166.		$H^+ + H^+ + H + e + e + e$			
167.		$H^+ + H^+ + H^* + e + e + e$			

N	Reactants	Products	Range (eV)	Reference	Remarks
168.	$H^- + H_3^+$	$H^- + H_3^+$			
169.		$H + H_3$			
170.		$H + H + H_2$			
171.		$H + H^* + H_2$			
172.		$H + e + H_2^+ + H$			
173.		$H^+ + e + e + H_3^+$			
174.		$H^+ + e + e + H_2 + H^+$			
175.		$H^- + H^+ + H_2$			
176.		$H + e + H_2 + H^+$			
177.		$H^* + e + H_2 + H^+$			
178.		$H + e + H_3^+$			
179.		$H^* + e + H_3^+$			
180.		$H + e + H + H + H^+$			
181.		$H^* + e + H + H + H^+$			
182.		$H^+ + e + e + H + H + H^+$			
183.		$H^- + H_2^+ + H$			
184.		$H^- + H_2 + H^+$			

H_2^+ Collisions					
N	Reactants	Products	Range (eV)	Reference	Remarks
185.	$H_2^+ + H$	$H_2^+ + H$			
186.		$H_2^+ + H^*$			
187.		$H_2 + H^+$			
188.		$H_2(\nu') + H^+$			
189.		$H_2^* + H^+$			
190.		$H^+ + H + H$			
191.		$H^+ + H + H^*$			
192.		$H^+ + H^+ + H + e$			
193.		$H^+ + H^+ + H^+ + e + e$			
194.		$H^- + H^+ + H^+$			
195.		$H^+ + H_2^+ + e$			
196.		H_3^+			
197.	$H_2^+(\nu) + H$	$H_2^+(\nu')+H$	$\sim$ 1-9 C.M. Energy	[126]	ν =1-14 ν'=1-18
			$\sim$1.5e1 - 1.0e2 C.M. Energy	[127]	ν =1-14 ν' =1-18
198.	$H_2^+ + H_2$	$H_2^+(\nu)+H_2(\nu)$			
199.		$H^+ + H + H_2(\nu)$			
200.		$H_2 + H_2^+$			
201.		$H_2^+ + H + H$			
202.		$H_2^+ + H + H^*$			
203.		$H_3^+ + H$			
204.		$H_3^+ + H^*$			
205.		$H^+ + H + H + H$			
206.		$H^+ + H^* + H + H$			
207.		$H_2^+ + H_2^+ + e$			
208.		$H^+ + H + H^+ + H + e$			
209.		$H^+ + H^* + H^+ + H + e$			
210.		$H^+ + H + H_2$			
211.		$H^+ + H^* + H_2$			
212.		$H^+ + H^+ + e + H_2$			
213.	$H_2^+ + H_3^+$	$H_2^+ + H_3^+$			
214.		$H_2^+ + H_2^+ + H(\nu)$			

H_3^+ Collisions					
N	Reactants	Products	Range (eV)	Reference	Remarks
215.	$H_3^+ + H$	$H_2 + H^+ + H$			
216.		$H_2 + H^+ + H^*$			
217.		$H_2 + H^+ + H^+ + e$			
218.		$H_2^+ + H + H$			
219.		$H_2^+ + H^* + H$			
220.		$H_2^+ + H_2(\nu)$			
221.		$H_3 + H^+$			
222.		$H_2^+ + H^+ + H^+ + e + e$			
223.		$H + H + H^+ + H$			
224.		$H + H + H^+ + H^*$			
225.		$H + H^+ + e + H^+ + H^+ + e$			
226.		$H^* + H^+ + e + H^+ + H^+ + e$			
227.	$H_3^+ + H_2$	$H^+ + H + H + H_2$			
228.		$H^+ + H_2 + H_2$			
229.		$H_3 + H_2^+$			
230.		$H + H_2^+ + H_2$			
231.		$H^+ + H + H + H$			
232.		$H_2^+ + H + H_2^+ + e$			
233.		$H_2 + H + H_2^+$			

3 Body Recombinations					
N	Reactants	Products	Range (eV)	Reference	Remarks
234.	$e + H^+ + e$	$e + H$			
235.		$e + H^*$			
236.		H^-			

Bibliography

[1] World energy outlook. Technical report, International Energy Agency, 2010.

[2] J. Reece Roth. *Introduction to Fusion Energy*. Ibis publishing, 1986.

[3] Roger A. Hinrichs. *Energy: Its Use And The Enviroment*. Sanders College Publishing, 1996.

[4] R.J. Goldston and P.H. Rutherford. *Introduction to Plasma Physics*. Institute of Physics Publishing, 1995.

[5] K.Miyamoto. *Plasma Physics for Nuclear Fusion*. The MIT press, 1989.

[6] W.K.Hogan. *Nucl.Fusion*, 44, 2004.

[7] J.D. Lawson. In *Proc. Phys.Soc.*, volume B70, 1957.

[8] U. Fantz, H. Falter, P. Franzen, D. Wünderlich, M. Berger, A. Lorenz, W. Kraus, P. McNeely, R. Riedl, and E. Speth. Spectroscopy: a powerful diagnostic tool in source development. *Nuclear Fusion*, 46(6):S297, 2006.

[9] R. S. Hemsworth and T. Inoue. Positive and negative ion sources for magnetic fusion. *IEEE Transaction on Plasma Science*, 33(6), December 2005.

[10] P. Franzen et al. Progress of the development of the IPP RF negative ion source for the ITER neutral beam system. *Nuclear Fusion*, 47, 2007.

[11] ITER Organization. *ITER Design Change Request 64*.

[12] Yu. I. Belchenko, G.I. Dimidov, and V. G. Dudnikov. *Nuclear Fusion*, 14, 1974.

[13] M. Bacal, E Nicolopoulou, and H. J. Doucet. In *Proc. Symp. on the Production and Neutralization of Negative Hydrogen Ions and Beams (Brookhaven National Laboratory Upton, NY, USA,)*, pages 26–34, 1977.

[14] M. Bacal and G. W. Hamilton. H^- and D^- production in plasmas. *Phys. Rev. Lett.*, 42(23):1538–1540, Jun 1979.

[15] M. Allan and S.F. Wong. Effect of vibrational and rotational exictation on dissociative attachment in hydrogen. *Phys.Rev.Lett*, 41:1791–974, 1978.

[16] J.N Bardsley and J.M. Wadehra. Dissociative attachment and vibrational excitation in low-energy collisions of electrons with H_2 and D_2. *Phys. Rev. A*, 20:1398–405, 1979.

[17] M. Bacal. Physics aspects of negative ion sources. *Nuclear Fusion*, 46(6):S250, 2006.

[18] J. R. Hiskes. Cross sections for the vibrational excitation of the $H_2(X^1\Sigma_g^+)$ state via electron collisional excitation of the higher singlet states. *Journal of Applied Physics*, 51(9):4592–4594, 1980.

[19] M. Bacal et al. In *Proceeding of the 1999 ICIS conference, Kyoto*, 1999.

[20] O. Fukamasa. identification of cesium effect on enhancement of H^- production in a volume negative ion source. *Review of Scientific Instruments*, 2009.

[21] *Elementary Processes in Hydrogen-Helium Plasmas*. Springer Series on Atoms and Plasmas, Springer-Verlag, 1987.

[22] *Alladin Database, http://www.amdis-iaea.org/ALLADIN*.

[23] C.F. Barnett. Collisions of H, H_2, He and Li atoms and ions with atoms and molecules. Report ornl-6086/vi, Oak Ridge National Laboratory, Oak Ridge, Tennessee 37831, USA (1990), 1990.

[24] B. Peart and R. A. Forrest. Measurement of cross section for double charge transfer in collision between H^+ and H^- ions. *J. Phys. B*, 12, 1979.

[25] H. Brauning et al. Double electron transfer in $H^- + H^+$ collision. In *Journal of Physics: Conference Series 88*, 2007.

[26] F. Brouillard et al. Double charge exchange in $H^+ - H^-$ collisions. *J. Phys. B*, 12, 1979.

[27] *http://www.mathworks.com/products/matlab/.*

[28] I. Langmuir. The effect of space charge and initial velocities on the potential distribution and thermionic current between parallel plane electrodes. *Phys. Rev.*, 21(419-435), 1923.

[29] I. Langmuir. The interaction of electron and positive ion space charge in cathode sheaths. *Phys. Rev.*, 33(6):954 989, 1929.

[30] R.N. Franklin. The plasma–sheath boundary region. *J. Phys. D: Appl. Phys*, 36, 2003.

[31] K. U. Riemann. The Bohm criterion and sheath formation. *J. Phys. D: Appl. Phys.*, 24, 1991.

[32] M. Van Dyke. *Perturbation methods in fluid mechanics.* Academic Press, New York, 1964.

[33] A. H. Nayfeh. *Introduction to perturbation techniques.* J. Wiley, New York, 1981.

[34] Lam S. H. Unified theory for the Langmuir probe in a collisionless plasma. *Phys. Fluids*, 8:73–87, 1965.

[35] R.N. Franklin and J.R. Ockendon. Asymptotic matching of plasma and sheath in an active low pressure discharge. *J. Plasma Phys.*, 4, 1970.

[36] K. U. Riemann. Kinetic theory of the plasma sheath transition in a weakly ionized plasma. *Phys. Fluids*, 24, 1981.

[37] K. U. Riemann. The Bohm criterion and boundary conditions for a multicomponent systems. *IEEE Trans. Plasma Sci.*, 23:709, 1995.

[38] V.A. Godyak and N. Sternberg. Smooth plasma-sheath transition in a hydrodynamic model. *IEEE Trans. Plasma Sci.*, 18:159–168, Feb. 1990.

[39] V.A. Godyak and N. Sternberg. Good news, you can patch active plasma and collisionless sheath. *IEEE Trans. Plasma Sci., 31. (2002).*, 31, 2002.

[40] Kaganovich I. How to patch active plasma and collisionless sheath: Practical guide. *Phys. Plasmas*, 9, 2002.

[41] M.S. Benilov and R.N. Franklin. Asymptotic theory of a collision-dominated space-charge sheath with a velocity-dependent ion mobility. *Journal of Plasma Physics*, 67, 2002.

[42] H. B. Valentini. Bohm criterion for the collisional sheath. *Phys. Plasmas*, 3:1459, 1996.

[43] V.A. Godyak. Modified Bohm criterion for a collisional plasma. *Phys. Lett. A*, 89:80–81, 1982.

[44] T.E. Sheridan and J. Goree. Collisional plasma sheath model. *Phys. Fluids. E*, 3(10), 1991.

[45] P. C. Stangeby. *The plasma boundary of magnetic fusion device*. Taylor and Francis, 2000.

[46] Daybelge and Bein. Electric sheath between a metal surface and a magnetized plasma. *Phys. Fluids*, 24:1190, 1981.

[47] R. Chodura. Plasma wall transition in an oblique magnetic field. *Phys. Fluids*, 25:1628, 1982.

[48] P. G. Stangeby. The Bohm-Chodura plasma sheath criterion. *Phys. Plasmas*, 2:702, 1995.

[49] P.G. Stangeby and A.V. Chankin. The ion velocity (Bohm-Chodura) boundary condition at the entrance to the magnetic presheath in the presence of a diamagnetic and e xb drifts in the scrape-off layer. *Phys.Plasmas*, 2(3), 1995.

[50] K. U. Riemann. Theory of the collisional presheath in an oblique magnetic field,. *Phys. Plasmas*, 1(3), 1994.

[51] Kono A. Formation of an oscillatory potential structure at the plasma boundary in electronegative plasmas. *J. Phys. D 32*, 32:1357, 1999.

[52] Braithwaite and Allen. Boundaris and probes in electronegative plasmas. *J. Phys. D*, 21:1733, 1988.

[53] K. Sato and F. Miyawaki. Formation of presheath and current,Äêfree double layer in a two-electron-temperature plasma. *Phys.Fluids B*, 4:1247, 1992.

[54] H. Amemiya and G. Fuchs. Double sheath formed between two electronegative plasmas. *Plasma Sources Science and Technology*, 13(2), 2004.

[55] Kono A. Intrinsic sheath edge conditions for sheath instability in low-pressure electronegative plasmas. *Journal of physics. D*, 36(5), 2003.

[56] E. R. Harrison and W. B. Thompson. The low pressure plane symmetric discharge. In *Proc Phys. Soc. London*, volume 74, 1959.

[57] F. Taccogna, S. Longo, M. Capitelli, and R. Schneider. Negative ion source modeling: form expansion to extraction region. *IEEE Transaction on Plasma Science*, 36(4):1589–1599, 2008.

[58] F. Taccogna, P. Minelli, S. Longo, and M. Capitelli. Two dimensional particle in cell model of the extraction region of a hybrid negative ion source. In *NIBS conference proceeding*, 2010.

[59] S. Mochalskyy, A.F. Lifschitz, and T. Minea. 3D modeling of negative ion extraction from a negative ion sources. *Nuclear Fusion*, 50, 2010.

[60] *OPERA, http://www.cobham.com/about-cobham/avionics-and-surveillance/about-us/technical-services/kidlington/products/opera-3d/space-charge.aspx*, 2010.

[61] P. Spadtke and C. Muhle. Simulation of ion extraction and beam transport. *Review of Scientific Instruments*, 71:820, 2000.

[62] J. Pamela. A model for negative ion extraction and comparison of negative ion optic calculation to experimenta result. *Review of Scientific Instruments*, 62, 1991.

[63] *Omnitrack Manual, http://www.fieldp.com/manual/omnitrack*, 2010.

[64] M. Cavenago, P. Veltri, F. Sattin, G. Serianni, and V. Antoni. Negative ion extraction with finite element method and ray maps. *IEEE Transaction on Plasma Science*, 36(4), 2008.

[65] M. A. Lieberman and A. J. Lichtenberg. *Principles of Plasma Discharges and Material Processing*. John Wiley, New York, 1994.

[66] L. Tonks and J. Langmuir. A general theory of the plasma of an arc. *Physical Review*, 34:876, 1929.

[67] S.A. Self. Exact solution of the collisionless plasma sheath equation. *Physics of Fluid*, 6:1762–1768, 1963.

[68] M. Abramovitz and I.A. Stegun. *Handbook of mathematical functions*. 10 edition, 1972.

[69] D. Wünderlich, R. Gutzer, and U. Fantz. Influence of magnetic fields and biasing on the plasma of a rf driven negative ion source. In *AIP Conference Proceedings*, volume 925, pages 46–57, 2007.

[70] M. Cavenago. High vacuum gas pumping and boundary coupling. In *Comsol Conference proceedings*, 2008.

[71] P. Clausing. The flow of highly rarefied gases throught tubes of arbitrary length. *Jour. Vac. Sci. Techn. A*, 8, 1971.

[72] E. Surrey. Space charge neutralization in the ITER negative ion beams. *AIP Conference Proceedings*, 925(1):278–289, 2007.

[73] M. Cavenago and P. Veltri. Space charge compensation of negative ion beams. In *Comsol Conference Proceedings, Paris*, 2010.

[74] *Comsol Manual, http://www.comsol.com*, 2010.

[75] J. Rice. *Numerical Methods, Software and Analysis*. Academic Press, 2 edition, 1992.

[76] P. Agostinetti, V. Antoni, M. Cavenago, G. Chitarin, N. Marconato, D. Marcuzzi, N. Pilan, G. Serianni, P. Sonato, P. Veltri, and P. Zaccaria. Physics and engineering design of the accelerator and electron dump for spider. *Submitted to Nuclear Fusion*, 2010.

[77] J. R. Pierce. *Theory and design of electron beams*. Van Nostrand, Princetown, 1954.

[78] G. Fubiani, R.S. Hemsworth, H.P. de Esch, and A. Simonin. Modelling of secondary emission processes in ion based electrostatic accelerator of the International Thermonuclear Experimental Reactor. *Physical review Special Topics, Accelerators and Beams*, 11, 2008.

[79] P. Agostinetti, V. Antoni, M. Cavenago, H.P.L. de Esch, G. Fubiani, D. Marcuzzi, S. Petrenko, N. Pilan, W. Rigato, G. Serianni, M. Singh, P. Sonato, P. Veltri, and P. Zaccaria. Design of a low voltage, high current extraction system for the ITER ion source. *AIP Conference Proceedings*, (1097):325, 2009.

[80] M. Cavenago, P. Veltri, E. Gazza, G. Serianni, and P. Agostinetti. Negative ion beams and secondary beams. In *Comsol Conference Proceedings*, 2009.

[81] A. J.T. Holmes. Theoretical and experimental study of space charge in intense ion beams. *Phys. Rev. A*, 19(1), 1979.

[82] I. A. Soloshenko. Transportation of intense ion beams. *Review of Scientific Instruments*, 69:1359, 1998.

[83] M. D. Gabovitch et al. *Soviet journal of plasma physics*, 1975.

[84] A. J.T. Holmes. Space charge compensation of ion beams. In *The Physics and Technology of Ion Sources*, chapter 3. John Wiley & Sons, I edition, 1989.

[85] N. Chauvin et al. Beam dynamic simulation of the low energy beam transport line for ifmif/eveda. In *Proceeding of LINAC08*, 2008.

[86] J. L. Vay and C. Deutsch. Charge compensated ion beam propagation in a reactor sized chamber. *Physics of Plasma*, 5, 1998.

[87] S. C. L. Srivastava et al. Study of space charge compensation in lebt. In *APAC conference proceeding*, 2007.

[88] A. Benismail, R. Duperrier, and N. Pichoff. Space charge compensation studies of hydrogen ion beams in a drift section. *Phys. Rev. ST Accel. Beams*, 10, 2007.

[89] G. Fubiani, R. S. Hemsworth, H. P. L. de Esch, and L. Svensson. Analysis of the two accelerator concepts foreseen for the neutral beam injector of the international thermonuclear experimental reactor. *Phys. Rev. ST Accel. Beams*, 12(5):050102, May 2009.

[90] P. Agostinetti, V. Antoni, M. Cavenago, G. Chitarin, N. Marconato, D. Marcuzzi, N. Pilan, G. Serianni, P. Sonato, P. Veltri, and P. Zaccaria. RFX-SPIDER-TN-83: Physics and engineering design of the accelerator and electron dump for spider. Technical report, Consorzio RFX, 2010.

[91] P.F. Staub. Bulk target backscattering coefficient and energy distribution of 0.5-100 keV electrons: an empirical and synthetic study. *J. Phys. D*, 27, 1994.

[92] T. Matsukawa, R. Shimizuand, and H. Hashimoto. Measurements of the energy distribution of backscattered kilovolt electrons with a spherical retarding-field energy analyser. *J. Phys. D*, 6, 1974.

[93] E. J. Sternglass. Backscattering of kilovolt electrons from solids. *Phys. Rev.*, 95(345), 1954.

[94] E. W. Thomas. *Data compendium for plasma surface interaction.* Nuclear fusion, 1984.

[95] G. Serianni, P. Agostinetti, V. Antoni, M. Cavenago, G. Chitarin, G. Fubiani, E. Gazza, N. Marconato, N. Pilan, and P. Veltri. Secondary particles in the accelerator stage of high current, high voltage neutral beam injectors: the case of the injector of the thermonuclear fusion experiment iter. In *proceeding of IPAC conference, Kyoto*, 2010.

[96] W.B Hermansfeld. Electron trajectory program. Technical report, Stanford Linear Accelerator Center, 1979.

[97] N. Pilan at al. IRES: a code evaluating the beamlet beamlet interaction for multi-aperture electrostatic accelerators. In *Proceedings of 36th International Conference on Plasma Science, San Diego, California. To be published in IEEE transaction on Plasma Science*, 2009.

[98] *ANSYS Manual, http://www.ansys.com.*

[99] A. Krylov and R. S. Hemsworth. Gas flow and related beam losses in the ITER neutral beam injector. *Fusion Eng. Des.*, 81:2239, 2006.

[100] Y. Takeiri, O. Kaneko, Y. Oka, K. Tsumori, M. Osakabe, R. Akiyama, T. Kawamoto, and E. Asano. Construction of negative-ion-basednbi system in large helical device. *IEEE Trans. Plasma Sci.*, 1998.

[101] L. Grisham. The operational phase of negative ion beam systems on JT-60U and LHD. *IEEE Trans. Plasma Sci.*, 33, 2005.

[102] Y. Takeiri, O. Kaneko, K. Tsumori, Y. Oka nd K. Ikeda, M. Osakabe, K. Nagaoka, E. Asano, T. Kondo, M. Sato, and M. Shibuya. High-power and long-pulse injection with negative-ion-based neutral beam injectors in the Large Helical Device. *Nuclear Fusion*, 46, 2006.

[103] Tsumori K., Osakabe M., Kaneko O., Takeiri Y., Nagaoka K., Oka Y., Ikeda K., Shibuya M., Asano E., Komada S., Kondo T., and Sato M. Neutral beam injection with an improved accelerator for LHD. *Review of Scientific Instruments*, 2008.

[104] K. Tsumori, M. Osakabe, Y. Takeiri, O. Kaneko, K. Nagaoka, K. Ikeda, H. Nakano, Y. Oka, M. Shibuya, E. Asano, S. Komada, T. Kondo,

and M. Sato. Beamlet characteristics in the accelerator with multislot grounded grid. *Review of Scientific Instruments*, 2010.

[105] G. Chitarin et al. Experimental mapping and benchmarking of magnetic field codes on the lhd ion accelerator. In *Proceedings of the 2nd International Symposium on Negative Ions, Beams and Sources,*, 2010.

[106] D. Ciric. *Permag Manual, private communication from D. Ciric.* CCFE, Abingdon, United Kingdom., 2007.

[107] P. Agostinetti et al. Modeling activities on the negative-ion-based neutral beam injectors of the large helical device. In *Proceedings of the 2nd International Symposium on Negative Ions, Beams and Sources*, 2010.

[108] M. Cavenago, V. Antoni, G. Serianni, P.Veltri, T. Kulevoy, and S. Petrenko. Nio1 a versatile negative ion source. In *Proceding of IPAC Conference, Kyoto*, 2010.

[109] M. Cavenago, V. Antoni, T. Kulevoy, S. Petrenko, G. Serianni, and P. Veltri. Development of small multiaperture negative ion beam sources and related simulation tools. in:. In *AIP Conf. Proc. 1097 of 1st Int. Conf. Neg. Ions, Beams and Sources*, 2009.

[110] B. I. Cohen, A. B. Langdon, and A. Friedman. Implicit time integration for plasma simulation. *Journal of computational physics*, 46:15–38, 1982.

[111] G. Fubiani at al. Large time step e grid size implicit particle in cell simulation applied to large plasma devices. In *Proceedings of the 2nd International Symposium on Negative Ions, Beams and Sources, Takayama, Japan*, 2010.

[112] L. Cranberg. *Journal of Applied Physics*, 23:538, 1952.

[113] W. K. Mansfield. *British journal of Applied physics*, 11:454, 1960.

[114] H. R. Mc Hyder. *Review Phys. Appl.*, 12:1493, 1977.

[115] B. P. Singh and P. A. Chatterton. A new model of microdischarge current growt in vacuum. *J. Phys. D*, 9, 1976.

[116] T. Inoue et al. 1 MeV, ampere class accelerator R&D for ITER. *Nuclear Fusion*, 46, 2006.

[117] H.P.L. de Esch. Result of the SINGAP neutral beam accelerator experiment at JAEA. *Fusion Eng. Des.*, 84:669–675, 2009.

[118] M. Cavenago, P. Antonini, P. Veltri, N. Pilan, V. Antoni, and G. Serianni. Cascades of secondary particles in high voltage accelerators. In *Comsol Conference Proceedings, Milan*, 2009.

[119] N. Pilan, P. Veltri, and A. De Lorenzi. Voltage holding prediction in multi electrode-multi voltage systems insulate in vacuum. *IEEE Trans. on Dielectrics and Electrical Insulation*, 2010.

[120] I. N. Slivkov. Mechanism for electrical discharge in vacuum. *Sov. Phys. Techn.*, 2, 1928 (1957).

[121] A. Rizzolo, M. Dalla Palma, M. De Muri, and G. Serianni. Design and analyses of a one dimensional cfc calorimeter for spider beam characterisation. *Fusion Eng. Des.*, 85, 2010.

[122] M. De Muri, M. Dalla Palma, P. Veltri, A. Rizzolo, N. Pomaro, and G. Serianni. thermal and elecrostatic analyses of one dimentional cfc diagnostic calorimeter for SPIDER beam characterisation. In *Comsol Conference Proceedings, Milan*, 2009.

[123] J.J. Smith R.K. Janev. *Cross sections for collision processes of hydrogen atoms with electrons, protons and multiply charged ions, in Atomic and Plasma Material interaction Data for Fusion*, volume 4, pages 1–180. IAEA, Wien, 1993.

[124] R. N. Hill. Proof that the H^- ion has only one bound state. *Phys. Rev. Lett.*, 38(12):643, 1977.

[125] F. V. Von Busch and G. H. Dunn. *Phys. Rev.*, 5:1726, 1972.

[126] P.S. Krstic. Inelastic processes from vibrationally excited states in slow $h^+ + h_2$ and $h + h_2^+$ collisions: Excitations and charge transfer. *Phys. Rev. A*, 66, 2002.

[127] P.S. Krstic. Vibrationally resolved collisions in cold hydrogen plasmas. *Nuclear instruments and methods in Physics Research*, 241(1-4):58–62, 2005.

[128] P.S. Krstic and D.R. Schultz. *Elastic and Related Transport Cross Sections for Collisions among Isotopomers of* $H^+ + H$, $H^+ + H_2$, $H^+ + He$, $H + H$, *and* $H + H_2$. IAEA, Wien, 1998.

Acknowledgements

Molte sono le persone che, in diversi modi, hanno contributo al completamento di questo lavoro di tesi e meritano i miei ringraziamenti. Tra di essi Gianluigi è il primo che, credo non a caso, mi viene in mente; lo ringrazio non solo l'inestimabile supporto tecnico che mi ha dato durante tutto il mio periodo di lavoro a RFX, ma anche per il modo in cui questo aiuto mi è stato offerto. Chi ha avuto la fortuna di lavorare con lui capisce a cosa mi riferisco. Un sentito grazie va anche a Marco Cavenago, con cui ho piacevolmente collaborato per gran parte del lavoro presente in questa tesi. La semplicità e brillantezza con cui si pone rispetto a problemi che spaziano dalla fisica teorica alla quale sia la migliore posizione di una particolare vite sono per me fonte di continua meraviglia. Grazie anche a Vanni Antoni, perché nonostante i suoi impegni siano cresciuti esponenzialmente negli ultimi mesi ha comunque trovato il tempo di darmi consigli preziosi e perché dopo ogni chiacchierata con lui mi sembra di vedere le cose con più chiarezza. La mia gratitudine va anche al professor Gnesotto, che ha anche trovato il tempo di rileggere criticamente alcune parti della tesi, a Susanna Cappello, per la professionalità e simpatia e con svolge il suo ruolo di capogruppo e ed a tutte le altre persone con cui ho collaborato in questi anni, in ordine sparso: Erica, Piero, Nicola, Emanuele, Michela e tutti gli altri, incluso il gruppo NBI dell'esperimento giapponese LHD, dove ho trascorso una piccola ma fruttuosa parte del dottorato. Non posso non ricordare e ringraziare infine anche a tutti i compagni, di stanza o di merenda, che mi hanno circondato negli ultimi anni a RFX: non avrei mai detto che dalla coabitazione forzata di decine di persone in pochi metri quadri potesse venire qualcosa di così buono (e la cosa ha ancora più valore se si pensa che le persone sono per lo più fisici e ingegneri!).

...Anche stavolta mi trovo a dover scrivere la parte dei ringraziamenti rivolta alle persone a me più care negli ultimi minuti prima di stampare il tutto. La cosa in effetti può non sorprendere troppo chi mi conosce bene e sa che le persone che davvero ritengo importanti, sono quelle con cui mi prendo più libertà, inclusa quella di relegarvi negli ultimi secondi e nelle ultime righe dei ringraziamenti.

Il primo grande grazie in questo senso va a papà, mamma, Flora, Federico, i miei nonni, ed il resto della mia famiglia, e spiegare il perché sarebbe tanto lungo quanto superfluo.
Un ultimo grazie è rivolto a tutti voi, " amis que vent emport / et il ventait devant ma port / les emporte..". Bhe, Se doveste mai indagare su questi versi scoprireste che il vento di cui si parla in realtà strappa via gli amici al protagonista! Però, l'idea del vento che ha portato voi, amici, davanti alla mia porta, a me piace, quindi intendetelo anche voi in questo senso. Che dire..non so se abbia un senso ringraziare una persona per come è fatta, questo non siamo noi a sceglierlo credo. Eppure è proprio per come siete che vorrei ringraziare ciascuno di voi. Nel cercare di ricordarvi tutti la mente mi si riempie di decine persone e momenti felici, e questo è bene. Allo stesso tempo il fatto che siate troppi per venir nominati singolarmente e che il tempo giochi a sfavore, mi costringe ad un grazie un pò generalizzato, e questo,lo so, è male. Prometto però che proprio ora dedicherò mentalmente un pensiero di ringraziemento a ciascuno di voi. Fatto!
Grazie.